Chapter 3

Numerical Weather Prediction Models

3.1 Summary

JMA operates NWP models to meet various kinds of requirements on weather forecasting. The suite of the NWP models covers a wide temporal range of forecast periods from a few hours to two seasons providing a seamless sequence of products for the public.

The Global Spectral Model (GSM) produces 84-hour forecast four times a day (00, 06, 12, 18 UTC) to support the official short-range forecasting (day 3) and to provide the lateral boundary conditions for the Meso-Scale Model (MSM). The GSM forecast at 12 UTC is extended to 11 days to support the official one-week forecasting.

Four ensemble prediction systems are in operation. The one-week ensemble forecast is performed with 51 ensemble members every day at 12 UTC supporting the official one-week forecasting. The typhoon ensemble forecast with 11 ensemble members runs four times a day (00, 06, 12 and 18 UTC) when typhoons exist or are expected to form or to come in the western-north Pacific. The model produces 132-hour forecast and supports activities of the RSMC Tokyo-Typhoon Center. The one-month ensemble forecast with 50 members is carried out once a week (every Wednesday and Thursday) to support the official one-month forecasting, which is issued on Friday. The two-week ensemble forecast is also executed to support early warning information on extreme weather on every Sunday and Monday using the one-month ensemble forecast system. The seasonal ensemble forecast using an atmosphere-ocean coupled model with 51 members is carried out once a month to support the official seasonal forecasting.

MSM is executed eight times a day (00, 03, 06, 09, 12, 15, 18 and 21 UTC). It produces 15-hour forecast from 00, 06, 12 and 18 UTC and 33-hour forecast from 03, 09, 15, 21 UTC, to support the very short-range forecasting and the aviation services. It provides the lateral boundary conditions for the Local Forecast Model (LFM).

LFM produces 9-hour forecast eight times a day (00, 03, 06, 09, 12, 15, 18 and 21 UTC) and supports the weather information regarding to severe weather disturbances and aviation services around Tokyo International Airport.

JMA also operates a global atmospheric transport model to support the RSMC for Emergency Response activities. The model stands ready to run anytime when an environmental emergency situation occurs.

JMA operates three kinds of Chemical Transport Models (CTMs). The Aerosol CTM produces 96-hour forecast to provide Kosa (Aeolian Dust) information, the stratospheric ozone CTM produces 48-hour forecast to support UV index information, and tropospheric-stratospheric ozone CTM produces 72-hour forecast to support the photochemical oxidant information. These CTMs are operated once a day at 12UTC. The radiative transfer model is also used for UV index information.

Table 3.1.1 (global) and Table 3.1.2 (regional) shows specifications of the major NWP models respectively. Details on the NWP models, the ensemble prediction systems, the atmospheric transport model and the chemical transport models are described particularly in the following Section 3.2 - Section 3.8. The operational verification procedure is explained in Section 3.9.

Table 3.1.1: Specifications of the global NWP models at JMA

	Global Spectral Model (GSM)	One-week Ensemble Prediction System (WEPS)	Typhoon Ensemble Prediction System (TEPS)	One-month Ensemble Prediction System
Forecast Range (Initial Time)	84 hours (00, 06, 18UTC) 264 hours (12UTC)	264 hours (12UTC)	132 hours (00,06,12,18UTC)	17 days (12UTC; Sun & Mon) 34 days (12UTC; Wed & Thu)
Horizontal Grids #	$(1920-60)\times 960$	$(640-48)\times 320$		
Truncation Wave #	TL959	TL319		TL159
Grid Spacing	20km	55km		110km
Vertical Layers	60			
Top Layer Pressure	0.1hPa			
Ensemble Size	-	51	11	50
Perturbation Generator	-	Singular Vector method		Combination of BGM method and LAF method (25 BGM and 2 initial dates with 1 day LAF)
Perturbed Area	-	Globe	North-Western Pacific and Vicinities of up to three TCs	Northern Hemisphere and the tropics
Radiation Process	Solar (every hour) Infrared (3 hourly)			
Convective Parametarization	Prognostic Arakawa-Schubert			
Cloud Process	Prognostic cloud water content			
PBL and Surface Fluxes	Mellor-Yamada level 2 Monin-Obukhov similarity			
Gravity Wave Drag	Long wave drag Short wave drag			
Land Surface Model	Simple Biosphere (SiB)			

Table 3.1.2: Specifications of the regional NWP models at JMA

	Meso-Scale Model (MSM)	Local Forecast Model (LFM)
Forecast Range (Initial Time)	15 hours (00,06,12,18UTC) 33 hours (03,09,15,21UTC)	9 hours (00,03,06,09,12,15,18,21UTC)
Forecast Domain	East Asia	Eastern part of Japan
Map Projection	Lambert Conformal	
Horizontal Grids #	721×577	551×801
Grid Spacing	5km	2km
Vertical Layers	50	60
Top Layer Height	21.8km	20.2km
Radiation Process	Solar (every 15 minutes) Infrared (every 15 minutes)	
Convective Parameterization	Kain-Fritsch	(not used)
Cloud Process	3-ice bulk microphysics	
PBL and Surface Fluxes	Mellor-Yamada-Nakanishi-Niino level 3 Monin-Obukhov similarity	
Gravity Wave Drag	(not used)	

3.2 Global Spectral Model (JMA-GSM1212)

3.2.1 Introduction

The Global Spectral Model (GSM) employs primitive equations to express resolvable motions and states of the atmosphere. It also incorporates sophisticated parameterization schemes for physical processes. In the horizontal, prognostic variables are spectrally discretized using triangular truncation at wave number 959 (TL959). The corresponding transform grids cover about 0.1875° in both longitude and latitude. In the vertical, the model has 60 layers up to 0.1 hPa.

JMA has operated GSM since March 1988. The model originally had a horizontal resolution of T63 and 16 vertical layers up to 10 hPa with a sigma coordinate system.

In a model upgrade implemented in November 1989, the truncation wave number and the number of vertical layers were increased to T106 and 21, respectively, and a hybrid η vertical coordinate system was adopted.

In March 1996, the horizontal resolution was doubled to T213 and the number of vertical layers was increased to 30. The cumulus parameterization was changed from a Kuo scheme to a prognostic Arakawa-Schubert scheme.

In December 1999, the physical package underwent extensive refinement. Treatment of cloud water content as a prognostic variable was introduced, and the moist convection process was improved.

In March 2001, the number of vertical layers was increased to 40 and the vertical domain was extended up to 0.4 hPa. The model was highly parallelized to suit massively distributed-memory parallel computer operation.

In February 2005, the Eulerian advection scheme was replaced with a semi-Lagrangian one, and the spectral resolution was increased from T213 (quadratic grid) to TL319 (linear grid). Incremental non-linear normal mode initialization and vertical mode initialization were also introduced.

On 1 March, 2006, operations at 06 and 18 UTC were begun with a forecast time of 36 hours in addition to those conducted at 00 UTC with a forecast time of 90 hours and 12 UTC with a forecast time of 216 hours.

On 21 November, 2007, the horizontal resolution of GSM was enhanced to TL959, while the number of vertical layers was increased to 60 and the vertical domain was extended up to 0.1 hPa (Iwamura and Kitagawa 2008; Nakagawa 2009). The numerical integration scheme was upgraded from the three-time-level leap-frog scheme to a two-time-level scheme. The forecasts run at 00, 06 and 18 UTC were altered to each cover a uniform period of 84 hours. At the same time, the 20-km-resolution Regional Spectral Model (RSM) and the 24-km-resolution Typhoon Model (TYM) were retired from operational use.

On 5 August, 2008, a reduced Gaussian grid was incorporated into GSM as a new dynamical core. This removed redundant grid points at higher latitudes, thereby saving on computational resources (Miyamoto 2006). Incremental non-linear normal mode initialization and vertical mode initialization were eliminated.

On 18 December, 2012, a relative humidity threshold was introduced to the diagnostic stratocumulus scheme.

In March 2013, the coverage period of the forecast run at 12 UTC was extended from 216 hours to 264 hours.

3.2.2 Dynamics

The GSM is based on the framework of a semi-implicit semi-Lagrangian global model. In order to overcome the general shortcomings of semi-Lagrangian models (such as the lack of conservation properties and the high computational cost of three-dimensional interpolations), a vertically conservative semi-Lagrangian scheme is adopted for the GSM.

3.2.2.1 Governing Equations

The GSM is run on an η vertical coordinate system, which is a hybrid between pressure p and σ ($\sigma = p/p_S$, where p_S is surface pressure), implicitly defined as $p = A(\eta) + B(\eta)p_S$. The prognostic variables (wind vector $\boldsymbol{u} = (u, v)$, temperature T, pressure p, specific humidity q and cloud water content q_c) follow the system of primitive equations in the η-coordinate system as follows:

$$\frac{d\mathbf{u}}{dt} = \left(\frac{\partial}{\partial t} + \mathbf{u}\cdot\nabla + \dot{\eta}\frac{\partial}{\partial \eta}\right)\mathbf{u} = -f\mathbf{z}\times\mathbf{u} - (\nabla\Phi + R_d T_V \nabla \ln p) + \mathbf{F}_{\boldsymbol{u}} \tag{3.2.1}$$

$$\frac{dT}{dt} = \frac{\kappa T_V \omega}{\left[1 + \left(C_{pv}/C_{pd} - 1\right) q\right] p} + F_T \tag{3.2.2}$$

$$\frac{dq}{dt} = F_q \tag{3.2.3}$$

$$\frac{dq_c}{dt} = F_c \tag{3.2.4}$$

$$\frac{\partial}{\partial t}\left(\frac{\partial p}{\partial \eta}\right) + \nabla\cdot\left(\mathbf{u}\frac{\partial p}{\partial \eta}\right) + \frac{\partial}{\partial \eta}\left(\dot{\eta}\frac{\partial p}{\partial \eta}\right) = 0 \tag{3.2.5}$$

Here, d/dt is a total derivative and ∇ is a horizontal gradient operator. The other notations used above are conventional: $\mathbf{z}$ is the unit vertical vector, T_V is the virtual temperature, f is the Coriolis parameter, R_d is the gas constant for dry air, and $\kappa = R_d/C_{pd}$. C_{pd} is the the specific heat capacity at the constant pressure of dry air and C_{pv} is the specific heat capacity at the constant pressure of water vapor. $\mathbf{F}_{\boldsymbol{u}}$, F_T, F_q and F_c are tendencies relating to parameterized processes. In addition, $\mathbf{F}_{\boldsymbol{u}}$ and F_T include the effects of horizontal diffusion (to be described later). Integrating Eq. (3.2.5) with respect to η using the boundary conditions of $\dot{\eta} = 0$ at $\eta = 0$ and $\eta = 1$, η-velocity and ω are found:

$$\dot{\eta}\frac{\partial p}{\partial \eta} = -\frac{\partial p}{\partial t} - \int_0^\eta \nabla\cdot\left(\mathbf{u}\frac{\partial p}{\partial \eta'}\right) d\eta' \tag{3.2.6}$$

$$\omega \equiv \frac{dp}{dt} = -\int_0^\eta \nabla\cdot\left(\mathbf{u}\frac{\partial p}{\partial \eta'}\right) d\eta' + \mathbf{u}\cdot\nabla p \tag{3.2.7}$$

The geopotential Φ is given by the following hydrostatic relation:

$$\frac{\partial \Phi}{\partial \eta} = -R_d T_V \frac{\partial \ln p}{\partial \eta} \tag{3.2.8}$$

3.2.2.2 Vertical Finite Difference Scheme

The vertical finite difference scheme is coded according to Simmons and Burridge (1981). The prognostic variables $\mathbf{u}$, T, q and q_c are defined on the full levels, while η (including vertical fluxes) is defined on half-integer levels. Pressure on half-integer levels are expressed as

$$p_{k-1/2} = A_{k-1/2} + B_{k-1/2} p_S \qquad (k = 1, 2, \ldots, \mathrm{kmax}) \tag{3.2.9}$$

Here, the level index k increases with height, $kmax$ is the index of the highest model level, $A_{k-1/2} = A(\eta_{k-1/2})$ and $B_{k-1/2} = B(\eta_{k-1/2})$. $A_{1/2}$ is set to zero so that the lowest level coincides with the ground surface, and values of $B_{k-1/2}$ above 50hPa are set to zero so that these levels coincide with constant pressure surfaces. For intermediate levels, $A_{k-1/2}$ and $B_{k-1/2}$ vary smoothly with k.

From the hydrostatic relation given by Eq. (3.2.8) the finite difference form of geopotential on the full level is chosen as

$$\Phi_k = \Phi_S + \sum_{k'=1}^{k-1} R_d T_{Vk'} \ln\left(\frac{p_{k'-1/2}}{p_{k'+1/2}}\right) + \alpha_k R_d T_{Vk} \tag{3.2.10}$$

$$\alpha_k = \begin{cases} 1 - \dfrac{p_{k+1/2}}{\Delta p_k} \ln\left(\dfrac{p_{k-1/2}}{p_{k+1/2}}\right) & (1 \le k < \mathrm{kmax}) \\ \ln 2 & (k = \mathrm{kmax}) \end{cases} \tag{3.2.11}$$

Here, Φ_S is the geopotential at the surface. The pressure gradient force term in Eq. (3.2.1) and the adiabatic heating rate term in Eq. (3.2.2) can then be written in discretized form as

$$(\nabla\Phi + R_d T_V \nabla \ln p)_k = \nabla\Phi_S + \left[\sum_{k'=1}^{k-1} R_d \nabla T_{Vk'} \ln\left(\frac{p_{k'-1/2}}{p_{k'+1/2}}\right) + \alpha_k R_d T_{Vk}\right] + h_k \nabla p_S$$
$$h_k = \sum_{k'=1}^{k-1} R_d T_{Vk'} \left(\frac{B_{k'-1/2}}{p_{k'-1/2}} - \frac{B_{k'+1/2}}{p_{k'+1/2}}\right) + \frac{R_d T_{Vk}}{p_{k-1/2}} B_{k-1/2} \tag{3.2.12}$$

and

$$\left[\frac{\kappa T_V}{C_p/C_{pd}}\frac{\omega}{p}\right]_k = \frac{\kappa T_{Vk}}{C_{pk}/C_{pd}}\frac{1}{\Delta p_k}\left[\left(\ln\frac{p_{k^-1/2}}{p_{k+1/2}}\right)\left(B_{k+1/2}\mathbf{u}_k\cdot\nabla p_S - \sum_{l=k+1}^{\text{kmax}}\nabla\cdot(\mathbf{u}_l\Delta p_l)\right) - \alpha_k\left(\nabla\cdot\mathbf{u}_k\right)\Delta p_k\right] \tag{3.2.13}$$

respectively. C_p is the specific heat capacity at the constant pressure of moist air. The vertical mass flux in Eq. (3.2.6) is discretized as

$$\left(\dot{\eta}\frac{\partial p}{\partial \eta}\right)_{k-1/2} = -B_{k-1/2}\frac{\partial p_S}{\partial t} - \sum_{l=k}^{\text{kmax}}\nabla\cdot(\mathbf{u}_l\Delta p_l) = B_{k-1/2}\sum_{l=1}^{\text{kmax}}\nabla\cdot(\mathbf{u}_l\Delta p_l) - \sum_{l=k}^{\text{kmax}}\nabla\cdot(\mathbf{u}_l\Delta p_l) \tag{3.2.14}$$

3.2.2.3 Horizontal Grid

To mitigate the overconcentration of grid points at high latitudes and lower the computational cost, a reduced Gaussian grid is adopted for the GSM. The number of east-west grid points at each latitude is determined based on the magnitude of associated Legendre functions, which is negligibly small at high latitudes and in high orders. With this method, the computational cost of Legendre transformation can also be reduced (Juang 2004). The number of east-west grid points is in fact restricted by FFT package specifications, the number of east-west decompositions in parallelization and the interval of coarser radiation grids.

3.2.2.4 Semi-implicit Semi-Lagrangian Formulation

Prior to integration, the forecast equations (Eq. (3.2.1) - Eq. (3.2.5)) are rewritten in the form of $d_H X/dt = \partial X/\partial t + \mathbf{u}\cdot\nabla X = R$ with vertical advection terms incorporated into R on the right-hand side. These equations are integrated with respect to time along the trajectory of the parcel from the departure point D at time t to the arrival point A at time $t + \Delta t$. The linear term L separated from the forcing term R is treated semi-implicitly (i.e. using a trapezoidal rule), and the remaining R, including vertical advection terms, are treated with spatial averaging (Tanguay *et al.* 1992).

The resulting linear terms are slightly amplified by the factor $\beta = 1.2$ for computational stability, and the following is obtained:

$$X^{A+} - X^{D0} = \Delta t\frac{R^{A0} + R^{D(+)}}{2} + \Delta t\beta\left[\frac{L^{A+} + L^{D-}}{2} - \frac{L^{A0} + L^{D0}}{2}\right] \tag{3.2.15}$$

Superscript A represents the arrival point $\mathbf{x}_{ij}$ assumed to be on the Gaussian grid, and D is the departure point $\mathbf{x}_{ij} - \boldsymbol{\alpha}$ (the displacement vector $\boldsymbol{\alpha}$, whose calculation will be described later). The abbreviations used above are the same as those for $X^{A+} = X(\mathbf{x}, t + \Delta t)$, $X^{D0} = X(\mathbf{x} - \boldsymbol{\alpha}, t)$, $R^{A0} = R(\mathbf{x}, t)$, $R^{D(+)} = R(\mathbf{x} - \boldsymbol{\alpha}, t + \Delta t)$ and others. $R^{D(+)}$ is calculated based on extrapolation with respect to time. Rearranging the terms of the above equations gives a system of linear equations for the unknown values X^{A+}:

$$X^{A+} - \frac{\beta\Delta t}{2}L^{A+} = \left[X^0 + \frac{\Delta t}{2}\left\{R^{(+)} - \beta\left(L^0 - L^-\right)\right\}\right]^D + \frac{\Delta t}{2}\left[R^0 - \beta L^0\right]^A \tag{3.2.16}$$

3.2.2.5 Vertically Conservative Semi-Lagrangian Scheme

Yoshimura and Matsumura (2003, 2004) developed a vertically conservative semi-Lagrangian scheme in which vertical advection is treated separately from horizontal advection so that the model preserves conservative vertically integrated quantities such as water vapor under non-dissipative conditions. This separate treatment also reduces the model's cost of interpolation.

Eq. (3.2.16) can be reformulated with flux forms appropriate for a scheme in which vertical advection can retain conservative properties. Beginning with Eq. (3.2.5) and Eq. (3.2.1) - Eq. (3.2.4), rewriting is performed as follows:

$$\frac{d_H}{dt}\frac{\partial p}{\partial \eta} = -D\frac{\partial p}{\partial \eta} - \frac{\partial}{\partial \eta}\left(\dot{\eta}\frac{\partial p}{\partial \eta}\right) \tag{3.2.17}$$

$$\frac{d_H}{dt}\left(X\frac{\partial p}{\partial \eta}\right) = -DX\frac{\partial p}{\partial \eta} - \frac{\partial}{\partial \eta}\left(\dot{\eta}X\frac{\partial p}{\partial \eta}\right) + R_X\frac{\partial p}{\partial \eta} \tag{3.2.18}$$

Here, X represents $\mathbf{u}$, T_V, q and q_c, and $R_X = dX/dt$. The parallel nature of these equations is easily recognizable. The first term on the right hand side of these equations represents the increase caused by horizontal convergence, and the second term is the increase caused by vertical flux convergence. With respect to the latter, where q and q_c being conservative when $R_X = 0$, devising a vertically integrated quantity that remains unchanged in vertical advection appears to be a promising approach. A simple outline of the procedure is given here for specific humidity q without R_q.

Vertical discretization and time integration during the period Δt described earlier give the following equations with the omission of terms related to the semi-implicit method for reasons of simplicity:

$$\begin{aligned}(\Delta p_k)^{A+} = &\left[(\Delta p_k)^0 - \frac{1}{2}(D_k\Delta p_k)^{(+)}\Delta t + \frac{1}{2}\left\{\left(\dot{\eta}\frac{\partial p}{\partial \eta}\right)_{k+1/2} - \left(\dot{\eta}\frac{\partial p}{\partial \eta}\right)_{k-1/2}\right\}^{(+)}\Delta t\right]^D \\ &+\left[-\frac{1}{2}(D_k\Delta p_k)^0\Delta t + \frac{1}{2}\left\{\left(\dot{\eta}\frac{\partial p}{\partial \eta}\right)_{k+1/2} - \left(\dot{\eta}\frac{\partial p}{\partial \eta}\right)_{k-1/2}\right\}^{0}\Delta t\right]^A\end{aligned} \tag{3.2.19}$$

$$\begin{aligned}(q_k\Delta p_k)^{A+} = &\left[(q_k\Delta p_k)^0 - \frac{1}{2}q_k^0(D_k\Delta p_k)^{(+)}\Delta t + \frac{1}{2}\left\{\left(q\dot{\eta}\frac{\partial p}{\partial \eta}\right)_{k+1/2} - \left(q\dot{\eta}\frac{\partial p}{\partial \eta}\right)_{k-1/2}\right\}^{(+)}\Delta t\right]^D \\ &+\left[-\frac{1}{2}q_k^+(D_k\Delta p_k)^0\Delta t + \frac{1}{2}\left\{\left(q\dot{\eta}\frac{\partial p}{\partial \eta}\right)_{k+1/2} - \left(q\dot{\eta}\frac{\partial p}{\partial \eta}\right)_{k-1/2}\right\}^{0}\Delta t\right]^A\end{aligned} \tag{3.2.20}$$

$$p_{k-1/2} = \sum_{k'=k}^{\mathrm{kmax}}\Delta p_{k'}, \quad (k = 1, 2, \ldots, \mathrm{kmax}) \tag{3.2.21}$$

Here, the vertically cumulative quantity Q is defined as follows:

$$Q_{k-1/2} = \sum_{k'=k}^{\mathrm{kmax}}\Delta Q_{k'}, \quad Q_k = q_k\Delta p_k, \quad (k = 1, 2, \ldots, \mathrm{kmax} + 1) \tag{3.2.22}$$

Eq. (3.2.20) rewritten for ΔQ_k is found to be similar to Eq. (3.2.19) for Δp_k, and there is a clear correspondence between Q and p. Computation of Q can therefore be carried out in the five steps outlined below in a fashion parallel to that of p. The first two steps concern the operations inside the square brackets $[\ldots]^D$ in the above equations. The third step involves the calculation of variables at departure points based on interpolation. The fourth and the fifth steps are similar to the first two, but for the operations in the square brackets $[\ldots]^A$.

1. First step: Horizontal divergence is calculated. As the mass of each layer Δp_k varies to $\Delta p'_k$, the half-level pressure values $p_{k-1/2}$ by which layers are bound also shift to $p'_{k-1/2}$, which can be computed using Eq. (3.2.21). The values of q_k remain constant under the horizontal convergence $q'_k = q_k$.

2. Second step: Vertical flux convergence is calculated using Eq. (3.2.14) as in the Eulerian scheme. In the same way as in the first step, $\Delta p'_k$ varies to $\Delta p''_k$, and the values of $p'_{k-1/2}$ shift to $p''_{k-1/2}$ except $k = 1$ ($p'_{1/2} = p''_{1/2}$). In this step, the shift in $Q'_{k-1/2}$ caused by the vertical flux convergence is computed based on interpolation from $Q'_{k-1/2}(p'_{k-1/2})$ using $Q''_{k-1/2} = Q'_{k-1/2}(p''_{k-1/2})$. This procedure ensures the conservation of the total mass-weighted integral $Q'_{1/2} = Q''_{1/2}$, because $p'_{1/2} = p''_{1/2}$ holds and the other values of $p''_{k-1/2}$ ($k = 2, 3, \ldots, kmax$) merely have their intervals changed in the vertical column. New values of q''_k are computed using $\Delta Q''_k$ and $\Delta p''_k$ with Eq. (3.2.22).

3. Third step: Horizontal advection is incorporated by computing $(\Delta p_k)^D$ and q_k^D via quasi-cubic interpolation.

4. Forth step: Vertical flux convergence is calculated at the arrival point via the second step.

5. Fifth step: Horizontal divergence is calculated at the arrival point via the first step.

The time-integration of q and q_c is completed based on these five steps, and that of $\mathbf{u}$, T_V and p_S is followed by the semi-implicit calculation shown in Eq. (3.2.16).

3.2.2.6 Departure Point Determination

The displacement vector $\boldsymbol{\alpha}$ (as yet undetermined) obeys the implicit equation

$$\boldsymbol{\alpha} = \Delta t \left\{ \frac{\mathbf{u}_k(\mathbf{x}_{ij} - \boldsymbol{\alpha},\ t + \Delta t) + \mathbf{u}_k(\mathbf{x}_{ij},\ t)}{2} \right\} \tag{3.2.23}$$

which expresses that the horizontal advection during the time interval Δt is related to the average of future time-step wind value at the departure point and current time-step wind value at the arrival point (SETTLS; Hortal 2002). To improve stability, a method based on wind integrated in a semi-Lagrangian scheme rather than the time extrapolated wind is adopted (Yoshimura 2002). This implicit equation is solved by successive insertions of $\boldsymbol{\alpha}$. For the computation of these vector components, it is considered that the axes of the local coordinates (λ, φ) rotate due to the spherical metric as a parcel advances along a trajectory, as is the case whenever horizontal vector components are interpolated on a sphere. The wind at the departure point is computed from linear interpolation except for the last third of the iteration, for which a quasi-cubic approach is used.

3.2.2.7 Spectral Method and Horizontal Diffusion

Spectral variables (i.e. vorticity $\zeta(= \mathbf{z} \cdot \nabla \times \mathbf{u})$, divergence $D(= \nabla \cdot \mathbf{u})$, T_V and $\ln(p_S)$) are expanded in terms of spherical harmonics with triangular truncation. In accordance with the framework of the semi-Lagrangian scheme, a linear Gaussian transformation grid is used. By solving the semi-implicit equations, horizontal diffusion and variables such as the differentials on the sphere are calculated using the spectral method (Bourke 1974; Hoskins and Simmons 1975). The remaining variables q and q_c are defined only on grid points.

To prevent the accumulation of small scale noise (spectral blocking), fourth-order linear horizontal diffusion is applied to ζ, D and T_V backward and implicitly for the spectral forms in the independent step after semi-implicit time integration:

$$\left(\frac{\partial \zeta}{\partial t}\right)_{\text{hdiff}} = -K\left(\nabla^4 - \frac{4}{a^4}\right)\zeta \tag{3.2.24a}$$

$$\left(\frac{\partial D}{\partial t}\right)_{\text{hdiff}} = -K\nabla^4 D \tag{3.2.24b}$$

$$\left(\frac{\partial T_V}{\partial t}\right)_{\text{hdiff}} = -K\nabla^4\left[T_V - \frac{\partial \bar{T}_V}{\partial \bar{p}}p\right] = -K\nabla^4\left[T_V - \frac{\partial \bar{T}_V}{\partial \bar{p}}B(\eta)p_S\right] \tag{3.2.24c}$$

Here, K is the horizontal diffusion coefficient and a is the radius of the earth. Bars over variables indicate the global average on the η-surface. Angular momentum conservation does not allow the horizontal diffusion

process to work on vorticity with total wave number 1 as shown by Eq. (3.2.24a). Diffusion for virtual temperature is modified to work on the constant pressure surface; otherwise, diffusion on a declining η-surface may produce spurious mixing along steep mountain slopes. The diffusion coefficient is chosen so that the power spectrum of enstrophy coincides with that expected based on two-dimensional turbulence theory. In layers above 100hPa, the coefficient is gradually enhanced with height to simulate a sponge layer that absorbs waves incident upon the upper boundary. Rayleigh friction is also implemented for layers above 50hPa.

3.2.3 Radiation

The radiative heating rate is computed as the divergence of net radiation fluxes F:

$$\left(\frac{\partial T}{\partial t}\right)_{\text{rad}} = \frac{g}{C_p}\frac{\partial F}{\partial p} \tag{3.2.25}$$

where g is the acceleration of gravity and C_p the specific heat at the constant pressure of moist air.

Solving radiative transfer equation is computationally very expensive. In order to reduce computational costs, full radiation computation is performed only every three hours for longwave and hourly for shortwave on a coarser (reduced radiation) grid.

3.2.3.1 Longwave Radiation

The basic framework for longwave flux and cooling rate computation follows the method of Chou *et al.* (2001). Longwave radiation is treated using the broad-band flux emissivity method for nine spectral bands shown in Figure 3.2.1.

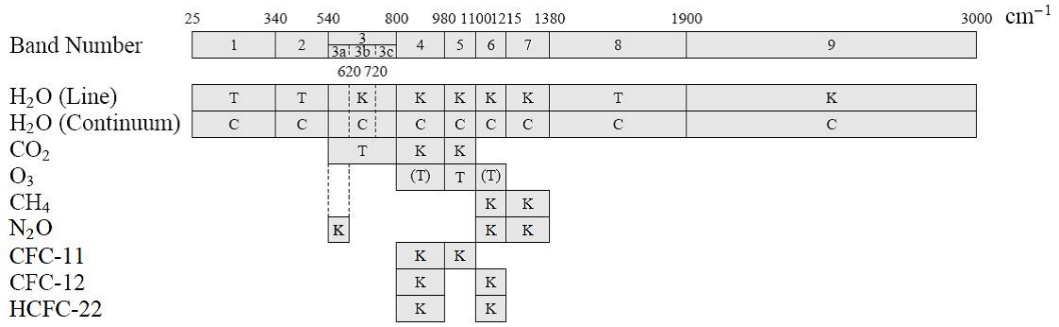

Figure 3.2.1: Spectral regions for evaluation of broad-band transmissivity. Letters represent transmittance calculation methods: K: k-distribution method; T: table look-up method; C: parameterization for water vapor continuum absorption.

Assuming a non-scattering atmosphere, the net longwave radiation flux F can be given by

$$F(p) = C\,(p,\ p_{\text{s}})\,\pi B\,(T_{\text{s}})\,\tau\,(p,\ p_{\text{s}}) + \int_{p_{\text{s}}}^{0} C\,(p,\ p')\,\pi B(T')\frac{\partial \tau\,(p,\ p')}{\partial p'}\,dp' \tag{3.2.26}$$

where p_s is the surface pressure, T_s the surface temperature, and T the air temperature. $\tau\,(p,\ p')$ denotes the band transmissivity between pressures p and p', and $B(T)$ the total Planck function. $C\,(p,\ p')$ is the clear sky fraction between pressures p and p' derived from fractional cloud cover assuming the maximum-random cloud overlap proposed by Geleyn and Hollingsworth (1979). Since clouds are treated as blackbodies, the effective cloudiness of semi-transparent cloud is given by the product of horizontal coverage and emissivity.

Band transmissivity is normalized using the Planck function $B_\nu(T)$ for each absorber in a given spectral region $\Delta\nu$:

$$\tau(p,\, p') = \int_{\Delta\nu} B_\nu(T_0)\tau_\nu(p,\, p')\, d\nu \Big/ \int_{\Delta\nu} B_\nu(T_0)\, d\nu \tag{3.2.27}$$

where T_0 is 250K. Depending on the absorber and the spectral band, band transmissivity is evaluated with three different approaches: the pre-computed table look-up method (Chou and Kouvaris 1991), the *k*-distribution method (Arking and Grossman 1972) for line absorption, and parameterization for water vapor continuum absorption. Gas absorption data are derived from HITRAN2000 (Rothman *et al.* 2003) for water vapor, carbon dioxide, ozone, methane, nitrous oxide and three CFCs. The e-type and P-type continuum absorption by water vapor is treated after the method of Zhong and Haigh (1995) with some refinement. In order to consider the broadening of absorption lines in the *k*-distribution method, the absorption coefficient is adjusted using a pressure scaling technique based on the Line-By-Line calculation. A diffusivity factor of 1.66 is used to approximate integration over the direction of radiance transmission.

3.2.3.2 Shortwave Radiation

Shortwave scattering and absorption are modeled in a two-stream formulation using the delta-Eddington approximation (Joseph *et al.* 1976; Coakley *et al.* 1983). The spectrum is divided into 22 bands based on Freidenreich and Ramaswamy (1999), while absorption by water vapor in the near-infrared region is based on Briegleb (1992). Assuming a plane parallel atmosphere, the diffuse radiance I is governed by the following radiative transfer equation:

$$\mu\frac{dI}{d\delta} + I = \frac{\omega_0}{2}\int_{-1}^{+1} p(\mu,\, \mu')I(\delta,\, \mu')\, d\mu' + \frac{\omega_0}{2}S_0 p(\mu,\, \mu_0)\exp\left(-\frac{\delta}{\mu_0}\right) \tag{3.2.28}$$

where δ is the optical thickness, ω_0 the single scattering albedo, and S_0 the incident solar irradiance in the direction μ_0 (the cosine of the solar zenith angle). The scattering phase function $p(\mu,\, \mu')$ defines the probability that radiation coming from direction μ' is scattered in direction μ. In the delta-Eddington method, the phase function is formed as a linear expression of μ with the fraction of forward-scattering peak f:

$$p(\mu,\, \mu') = 2f\delta(\mu - \mu') + (1 - f)\left(1 + 3\frac{g - f}{1 - f}\mu\mu'\right) \tag{3.2.29}$$

where $\delta(\mu - \mu')$ is the Dirac delta function and g the asymmetry factor.

Considering an atmosphere where the fraction C_{total} (which depends on cloud overlap assumption) is covered by clouds, the total shortwave radiation flux is given as a weighted average of the fluxes in the cloudy and clear sky fractions of the column as follows:

$$F = C_{\text{total}}F_{\text{cloudy}} + (1 - C_{\text{total}})F_{\text{clear-sky}} \tag{3.2.30}$$

The reflectance and transmittance of the cloudy and clear sky fraction of the layer are calculated as functions of the total optical thickness δ_{total}, the total single scattering albedo $\omega_{0\ \text{total}}$ and the total asymmetry factor g_{total} of the layer:

$$\delta_{\text{total}} = \delta_R + \delta_g + \delta_a + \delta_c \tag{3.2.31a}$$

$$\omega_{0\ \text{total}} = \frac{\delta_R + \omega_{0a}\delta_a + \omega_{0c}\delta_c}{\delta_R + \delta_g + \delta_a + \delta_c} \tag{3.2.31b}$$

$$g_{\text{total}} = \frac{g_a\omega_{0a}\delta_a + g_c\omega_{0c}\delta_c}{\delta_R + \omega_{0a}\delta_a + \omega_{0c}\delta_c} \tag{3.2.31c}$$

where the subscripts R, g, a and c denote molecular Rayleigh scattering, gaseous absorption, and Mie scattering/absorption caused by aerosols and cloud droplets, respectively.

The cloud optical properties are parametrized as functions of the cloud water path CWP and the effective radius of liquid droplets or ice particles r_e as follows:

$$\delta_c = \mathrm{CWP}(a + b/r_e) \tag{3.2.32a}$$

$$1 - \omega_{0c} = c + dr_e \tag{3.2.32b}$$

$$g_c = e + fr_e \tag{3.2.32c}$$

where the coefficients $a, \ldots, f$ are specified differently for liquid droplets (Slingo 1989) and for ice particles (Ebert and Curry 1992).

3.2.3.3 Radiatively Active Constituents

Radiatively active gases considered in the scheme are prognostic water vapor, climatological ozone, globally uniform carbon dioxide (at 375ppmv), oxygen (at 209490ppmv), methane (at 1.75ppmv), nitrous oxide (at 0.28ppmv) and CFC-11, CFC-12 and HCFC-22 (at 0.3, 0.5, 0.2ppbv, respectively). Monthly mean concentrations of ozone are specified by three-dimensional Chemical Transport Model calculation(see Subsection 3.8.4). Aerosol optical depth climatology is based on total-column value from Moderate Resolution Imaging Spectroradiometer (MODIS) and Total Ozone Mapping Spectrometer (TOMS) observations with seasonal variation. Other optical properties of aerosols are specified as continental and maritime background values without seasonal variation. The effective radius of cloud liquid droplets is fixed at 13 and 10 micrometers over the ocean and land, respectively. The effective radius of ice particles depends on temperature T and cloud ice content IWC (Wyser 1998) as follows:

$$B = -2 + 10^{-3}(273 - T)^{1.5} \log_{10} \frac{\mathrm{IWC}}{\mathrm{IWC}_0} \tag{3.2.33}$$

$$r_e = 377.4 + 203.3B + 37.91B^2 + 2.3696B^3 \tag{3.2.34}$$

where IWC_0 is $50\mathrm{gm}^{-3}$.

3.2.4 Cumulus Convection

3.2.4.1 Cumulus Model

An economical version of the Arakawa-Schubert scheme (Arakawa and Schubert 1974) developed by JMA is implemented. For economical computation, two simplifications are introduced. First, the vertical profile of the upward mass flux η is assumed to be a linear function of height z, as proposed by Moorthi and Suarez (1992), in the form of $\eta = 1 + \lambda(z - z_b)$, where λ denotes the entrainment rate and z_b is the cloud base height. Secondly, the mass flux at the cloud base is determined by solving a prognostic equation (Randall and Pan 1993) rather than by applying quasi-equilibrium assumption. The cloud base level is fixed near 900 hPa in the model. The moist static energy and other thermodynamic properties of the upward mass flux at the cloud base are given by the grid-scale values at the maximum moist static energy level below the base.

Following the concept of Arakawa and Schubert (1974), the ensemble effect of multiple types of cumuli is considered. Each type is defined by the level of the cloud top, where the updraft cloud mass loses buoyancy and detrainment occurs. The entrainment of the environmental air mass is considered during the upward movement of the cloud air mass. The entrainment rate λ of each cumulus is determined based on a no-buoyancy condition at the cloud top. The upper limit of λ is set to $1 \times 10^{-3}\ \mathrm{m}^{-1}$.

Here it is assumed that all condensed water in the updraft is carried up to the cloud top. Part of this water falls into the environment as rain, and the rest is detrained as cloud water. The ratio of rainwater and cloud water changes linearly with cloud depth. Detrained cloud water is redistributed to layers where the temperature is below freezing point.

3.2.4.2 Upward Mass Flux

The following prognostic equation is used for upward mass flux at the cloud base M_B:

$$\frac{dM_B(\lambda)}{dt} = \max\left(\frac{A(\lambda) - fA_0(\lambda)}{2\alpha},\ 0\right)\min\left(\frac{\lambda}{\lambda_{\min}},\ 1\right)\max\left(\lambda_{\max},\ 0\right)\left(\frac{\Delta p}{\Delta p_{\text{eff}}}\right) - \frac{M_B(\lambda)}{2\tau_d} \tag{3.2.35}$$

where A denotes the cloud work function, A_0 is the average of observed cloud work functions as given by Lord and Arakawa (1980), Δp is the depth of model cloud top layer, Δp_{eff} is the effective depth of the cloud top, and τ_d is the time constant of cumulus kinetic energy decay. The parameter f is introduced to incorporate the effects of grid-scale vertical wind and convective inhibition. This is given by

$$f = \frac{\omega}{\omega_0} + \frac{A_i}{A_{i0}} + c \tag{3.2.36}$$

where ω denotes the vertical pressure velocity at the lowest level, A_i represents the work involved in lifting the parcel to the level of free convection, and ω_0, A_{i0} and c are empirically determined constants. In order to suppress tall cumuli in dry conditions and incorporate the effects of turbulence in the planetary boundary layer, the parameter $\lambda_{\min}$ is defined as follows:

$$\lambda_{\min} = \max\left(\frac{0.9 - \text{RH}}{0.2},\ 10^{-3}\right) \times \frac{0.3}{5l_0} \tag{3.2.37}$$

where RH denotes the vertical mean of relative humidity between the cloud base and the cloud top, and l_0 represents the mixing length of the planetary boundary layer. The parameter $\lambda_{\max}$ is introduced to suppress tall cumuli with unnaturally large entrainment rates, and is defined as

$$\lambda_{\max} = \min\left(\frac{\lambda - \lambda_2}{\lambda_1 - \lambda_2},\ 1\right) \tag{3.2.38}$$

where $\lambda_1 = a_1/(z_t - z_b)$, $\lambda_2 = a_2/(z_t - z_b)$, z_t is the cloud top height, and a_1 and a_2 are empirically determined constants.

3.2.4.3 Convective Downdraft

The convective downdraft associated with cumulus convection affects the environment by reducing the net upward mass flux and detrainment from the downdraft. For reasons of economy, only one type of downdraft is assumed, while many types are considered in the updraft scheme.

The downdraft is initiated at the level where the net upward mass flux is reduced to half of that at the cloud base. The downdraft mass flux M_d at the cloud base is given by

$$M_d = 0.4M_B \tag{3.2.39}$$

Entrainment from the environment is assumed to occur above the cloud base, while detrainment is assumed to occur both above and below it. The entrainment and detrainment rates are set to the same constant value above the cloud base.

3.2.4.4 Triggering Mechanism

The convective triggering mechanism proposed by Xie and Zhang (2000) known as the dynamic CAPE generation rate (DCAPE) is used in the cumulus parameterization. DCAPE is defined as follows:

$$\text{DCAPE} = \left(\text{CAPE}\left(T^*, q^*\right) - \text{CAPE}\left(T, q\right)\right)/\Delta t \tag{3.2.40}$$

where T is the temperature, q is the specific humidity, and (T^*, q^*) are (T, q) plus the change caused by overall large-scale advection over a certain time period Δt (the integration time step used in the model). These values are equivalent to (T, q) just after dynamics calculation. CAPE is defined as

$$\text{CAPE} = \int_{z_{\text{LFC}}}^{z_{\text{LNB}}} g\frac{T_v^u - T_v}{T_v}dz \tag{3.2.41}$$

where z_{LFC} and z_{LNB} are the height of the level of free convection and that of neutral buoyancy, respectively, g is the acceleration of gravity, and T_v is the virtual temperature. The superscript u denotes air parcel lifting. Deep convection is assumed to occur only when DCAPE exceeds an empirically determined critical value.

3.2.4.5 Mid-level Convection

In the extratropics, moist convection does not always arise from the top of the planetary boundary layer. Accordingly, a mid-level convection scheme is incorporated to represent cumulus convection with its roots in the free atmosphere. The cloud base of mid-level convection is given by the maximum moist static energy level in the vertical column. The cloud top is defined as the level where an air mass rising from the cloud base with a constant entrainment rate loses buoyancy. The upward mass flux at the cloud base is given by

$$\frac{dM_B}{dt} = \frac{A}{2\alpha} - \frac{M_B}{2\tau_d} \tag{3.2.42}$$

where A is a cloud work function.

3.2.4.6 Convective Momentum Transport

The parameterization of convective momentum transport follows the scheme proposed by Kershaw and Gregory (1997) and Gregory *et al.* (1997). The horizontal momentum tendency caused by convection is parameterized as

$$\frac{\partial(\rho\overline{\boldsymbol{v}})}{\partial t} = -\frac{\partial M_u}{\partial z}\boldsymbol{v}^u + \frac{\partial}{\partial z}\left(M_u\overline{\boldsymbol{v}}\right) + \frac{\partial M_d}{\partial z}\boldsymbol{v}^d - \frac{\partial}{\partial z}\left(M_d\overline{\boldsymbol{v}}\right) \tag{3.2.43}$$

where $\boldsymbol{v}$ is the horizontal component of the wind vector, ρ is the air density, and M_u and M_d are upward and downward mass fluxes. The overbars denote the average over the horizontal grid, and the superscript $u(d)$ denotes a contribution from the convective upward (downward) domain. Entrainment and detrainment are assumed to occur between the cloud base and the cloud top.

3.2.4.7 Effects on Large-scale Tendencies

The effects of cumulus convection on large-scale tendencies are calculated using large-scale budget equations. The major contributions of such convection are made through 1) compensating downward motion, 2) detrainment of moisture from updraft at the cloud top, 3) detrainment from convective downdraft, and 4) convective momentum transport.

3.2.5 Clouds and Large-scale Precipitation

Clouds are prognostically determined in a fashion similar to that proposed by Smith (1990). The simple statistical approach proposed by Sommeria and Deardorff (1977) is adopted for the calculation of cloud amounts and their water content. In each grid box, the total water content (water vapor and cloud water) and the liquid water temperature are assumed to vary due to unresolved atmospheric fluctuations with uniform probability distribution. The cloud fraction C is given by the part of the grid box where the total water content q_w exceeds the saturation specific humidity q_s:

$$C = \frac{a_L\left(\overline{q}_w - q_s\left(T_L\right)\right) + \Delta q_w}{2\Delta q_w} \tag{3.2.44a}$$

$$a_L = \frac{1}{1 + \frac{L}{C_p}\left(\frac{\partial q_s}{\partial T}\right)_{T=T_L}} \tag{3.2.44b}$$

where L is the latent heat of condensation, C_p is the specific heat at constant pressure, Δq_w is the maximum local deviation from the grid-box mean total water content $\overline{q}_w$, and T_L is the liquid water temperature, defined as

$$T_L = T - \frac{L}{C_p} q_c \tag{3.2.45}$$

where T is the temperature and q_c is the cloud water content. In addition to this, for the representation of marine stratocumulus clouds, the cloud fraction C is diagnosed using the following scheme proposed by Kawai and Inoue (2006) when specific conditions are met:

$$C = 12.0\left(-\frac{\partial\theta}{\partial p} - 0.07\right) \tag{3.2.46}$$

where θ is the potential temperature and p is the pressure. Liquid (ice) cloud is assumed when the temperature is above 0°C (below −15°C). Between −15°C and 0°C, mixed-phase cloud is present and the mixing ratio changes linearly with temperature.

Parameterization for the rate of conversion P from cloud water to precipitation follows the scheme proposed by Sundqvist (1978):

$$P = c_0 q_c \left[1 - \exp\left\{-\left(\frac{q_c}{C q_c^{\mathrm{crit}}}\right)^2\right\}\right] \tag{3.2.47}$$

where $1/c_0$ represents a characteristic time scale for the conversion of cloud droplets into raindrops, and q_c^{crit} is the critical cloud water content at which the release of precipitation becomes efficient. The coalescence process (collection of cloud droplets by raindrops falling through a cloud) and the Bergeron-Findeisen effect (enhancement of precipitation release in clouds containing a mixture of droplets and ice crystals) are modeled following Sundqvist *et al.* (1989).

Based on Kessler (1969) and Tiedtke (1993), the evaporation rate E for large-scale precipitation is parameterized as

$$E = b \times \frac{1}{\tau_e} \times (q_s - q) \times \left\{\left(\frac{p}{p_s}\right)^{1/2} \frac{1}{b} \frac{P_l}{P_{l0}}\right\}^{0.577} \tag{3.2.48}$$

where b is the clear-sky precipitation fraction (set at 0.5), q_s is the saturation specific humidity, p is the pressure, p_s is the surface pressure, and P_l is the local precipitation rate. The values of constants are $1/\tau_e = 5.44 \times 10^{-4}\ \mathrm{s}^{-1}$ and $P_{l0} = 5.9 \times 10^{-3}\ \mathrm{kg\,m^{-2}\,s^{-1}}$. The melting process and snow sedimentation are also considered.

3.2.6 Surface Turbulent Fluxes

Surface turbulent fluxes are formulated with bulk formulae following the Monin-Obukhov similarity theory:

$$\overline{(w'\mathbf{v}')}_s = -C_m|\mathbf{v}_1|\mathbf{v}_1 \tag{3.2.49}$$

$$\overline{(w'\theta')}_s = -C_h|\mathbf{v}_1|(\theta_1 - \theta_s) \tag{3.2.50}$$

$$\overline{(w'q')}_s = -C_h|\mathbf{v}_1|(q_1 - q_s). \tag{3.2.51}$$

Here $\mathbf{v} = (u, v)$ represents horizontal wind, θ is potential temperature and q is specific humidity, and subscripts "1" and "s" indicate variables at the lowest level of the model grid and at the ground surface, respectively.

The bulk Richardson number R_{iB} is defined as

$$R_{iB} = \frac{g z_1(\theta_{v1} - \theta_{vs})}{T_1|\mathbf{v}_1|^2} \tag{3.2.52}$$

where z_1 is the height of the lowest level of the model grid above the ground, and θ_v is the virtual potential temperature.

Using the stability functions proposed by Louis *et al.* (1982), the exchange coefficients can be written as follows:

$$C_m = \begin{cases} \dfrac{\gamma_m}{1 + 10R_{iB}/\sqrt{1 + 5R_{iB}}} & R_{iB} > 0 \\ \gamma_m \left[1 - \dfrac{10R_{iB}}{1 + 75\gamma_m \sqrt{z_1 |R_{iB}|/z_{0m}}} \right] & R_{iB} \leq 0 \end{cases} \tag{3.2.53}$$

$$C_h = \begin{cases} \dfrac{\gamma_h}{1 + 15R_{iB}/\sqrt{1 + 5R_{iB}}} & R_{iB} > 0 \\ \gamma_h \left[1 - \dfrac{15R_{iB}}{1 + 75\gamma_h \sqrt{z_1 |R_{iB}|/z_{0h}}} \right] & R_{iB} \leq 0 \end{cases} \tag{3.2.54}$$

$$\begin{aligned} \gamma_m &= \frac{k^2}{\ln(z_1/z_{0m}) \ln(z_1/z_{0m})} \\ \gamma_h &= \frac{k^2}{\ln(z_1/z_{0m}) \ln(z_1/z_{0h})} \end{aligned} \tag{3.2.55}$$

where k is von Kármán's constant (= 0.4), while z_{0m} and z_{0h} are the surface momentum and heat roughness lengths, respectively.

Over land, surface roughness lengths ($z_{0m} = z_{0h}$) are determined based on vegetation types, and are affected by snow cover. Over ocean, surface wind stress depends on oceanic waves excited by surface winds. Roughness length and wind-induced stress are iteratively calculated in the model. Following the method of Beljaars (1995), surface roughness lengths over ice-free ocean are determined from Charnock's relation (Charnock 1955):

$$\begin{aligned} z_{0m} &= \frac{0.11\nu}{u_*} + \frac{\alpha}{g} u_*^2 \\ z_{0h} &= \frac{0.62\nu}{u_*} \end{aligned} \tag{3.2.56}$$

where $u_* \left(\equiv \left| \overline{(w'\mathbf{v}')_s} \right| \right)$ is the friction velocity, ν is the kinematic viscosity of air (= $1.5 \times 10^{-5} \mathrm{m}^2/\mathrm{s}$) and α the Charnock coefficient (= 0.020). The surface roughness length over sea ice is fixed at 0.001m.

3.2.7 Vertical Turbulent Diffusion

The level 2 turbulence closure scheme of Mellor and Yamada (1974) is used to represent the vertical diffusion of momentum, heat and moisture. The turbulent transports are expressed as

$$\overline{w'\mathbf{v}'} = -K_m \frac{\partial \mathbf{v}}{\partial z} \tag{3.2.57}$$

$$\overline{w's'_L} = -K_h \frac{\partial s_L}{\partial z} \tag{3.2.58}$$

$$\overline{w'q'_w} = -K_h \frac{\partial q_w}{\partial z} \tag{3.2.59}$$

where $s_L (\equiv C_p T + gz - Lq_c)$ is the liquid water static energy and $q_w (\equiv q + q_c)$ is the total water content.

Following the mixing-length theory, the diffusion coefficients can be written as

$$K_m = l^2 \left| \frac{\partial \mathbf{v}}{\partial z} \right| f_m(R_i) \tag{3.2.60}$$

$$K_h = l^2 \left| \frac{\partial \mathbf{v}}{\partial z} \right| f_h(R_i) \tag{3.2.61}$$

where the mixing length l is given according to Blackadar (1962) as;

$$l = \frac{kz}{1 + kz/l_0}. \tag{3.2.62}$$

The asymptotic mixing length l_0 is determined from sub-grid scale orographic variances and the planetary boundary layer depth.

The stability functions f_m and f_h are given following Mellor and Yamada (1982). The gradient Richardson number R_i is defined after the method of Smith (1990),

$$R_i = g \left\{ \tilde{\beta}_s \frac{\partial s_L}{\partial z} + \tilde{\beta}_Q \frac{\partial q_w}{\partial z} \right\} \Big/ \left| \frac{\partial \mathbf{v}}{\partial z} \right|^2 \tag{3.2.63}$$

where $\tilde{\beta}_s$ and $\tilde{\beta}_Q$ are buoyancy parameters in terms of the cloud-conserved quantities s_L and q_w, respectively.

3.2.8 Gravity Wave Drag

The parameterization for the orographic gravity wave drag consists of two components; one for long waves (wavelength > 100km) and the other for short waves (wavelength ≈ 10km). The long waves are assumed to propagate upward until reaching wave-breaking levels mainly in the stratosphere and exert drag there (type A scheme), while short waves are always regarded as trapped and dissipated within the lower troposphere (type B scheme). Therefore the fundamental difference between the two schemes appears in the vertical distribution of the momentum deposit. The type A scheme is based on Palmer *et al.* (1986) with some modifications. Details of type A and B schemes are explained in Iwasaki *et al.* (1989).

In both schemes, the momentum flux $\boldsymbol{\tau}_r$ excited by subgrid-scale variances of topography σ^2 is determined by

$$\boldsymbol{\tau}_r = \min\left(C_{gw}\, \rho_r\, N_r\, v_r\, \sigma^2,\ |\boldsymbol{\tau}_{r,\,sat}| \right) \boldsymbol{v}_r / v_r \tag{3.2.64}$$

where

$$\boldsymbol{\tau}_{r,\,sat} = C_{gw}\, \rho_r\, N_r\, v_r \left(\frac{\nu_r}{2F_c N_r} \right)^2 \boldsymbol{v}_r / v_r \tag{3.2.65}$$

C_{gw} is constant, ρ air density, N Brunt-Väisälä frequency, F_c critical Froude number, $\boldsymbol{v}$ the intrinsic velocity and $v = |\boldsymbol{v}|$. The subscript r denotes the reference level where the gravity wave stresses (momentum fluxes) are generated. There is a maximum of the momentum flux due to the valley blocking phenomenon, which is caused by stagnant flow near bottoms of valleys. This phenomenon occurs when the Froude number is below a critical value. The blocking effectively reduces the amplitudes of gravity waves. The topographic variances σ^2 are derived from the GTOPO30, which is $30'' \times 30''$ geographical data. First, the mean elevation (h_m) and its standard deviation (σ_m) over a $5' \times 5'$ grid box are evaluated from GTOPO30. The standard deviation of $(h_m - h)$ in a Gaussian grid box is regarded as σ in the type A scheme where h denotes the model topography, while the average of σ_m in the Gaussian grid box is regarded as σ in the type B scheme.

In the type A scheme, the momentum deposit is determined by the amplitude saturation hypothesis. The gravity wave stress at the $(k + 1/2)$-th level is given by

$$\boldsymbol{\tau}_{k+1/2} = \min\left(\left| \boldsymbol{\tau}_{k-1/2} \right|,\ |\boldsymbol{\tau}_{sat}| \right) \boldsymbol{\tau}_r / |\boldsymbol{\tau}_r| \tag{3.2.66}$$

where

$$\boldsymbol{\tau}_{sat} = C_{gw}\, \rho\, N \left(\boldsymbol{v} \cdot \frac{\boldsymbol{\tau}_r}{|\boldsymbol{\tau}_r|} \right) \left[\frac{\epsilon}{2F_c N} \left(\boldsymbol{v} \cdot \frac{\boldsymbol{\tau}_r}{|\boldsymbol{\tau}_r|} \right) \right]^2 \frac{\boldsymbol{\tau}_r}{|\boldsymbol{\tau}_r|} \tag{3.2.67}$$

ϵ is a function of the Richardson number

$$R_i = N^2 \Big/ \left[\frac{\partial}{\partial z} \left(\boldsymbol{v} \cdot \frac{\boldsymbol{\tau}_r}{|\boldsymbol{\tau}_r|} \right) \right]^2 \tag{3.2.68}$$

The wave stress of short gravity waves decreases with altitude due to nonhydrostatic effects (*e.g.*, Wurtele *et al.* 1987). In the type B scheme, the wave stress is simply assumed to be a quadratic function of pressure and to vanish around 700hPa as follows:

$$\tau(p) = \begin{cases} \tau(p_s) \cdot \dfrac{(p/p_s - 0.7)^2}{0.3^2} & p/p_s \geq 0.7 \\ 0 & p/p_s < 0.7 \end{cases} \tag{3.2.69}$$

Gravity wave drag is calculated by taking a vertical convergence of gravity wave fluxes as follows:

$$\frac{\partial v}{\partial t} = \frac{1}{\rho}\frac{\partial \tau}{\partial z} \tag{3.2.70}$$

3.2.9 Land Surface Processes

The Simple Biosphere scheme (SiB) developed by Sellers *et al.* (1986), Sato *et al.* (1989a) and Sato *et al.* (1989b) is implemented in the model. Evapotranspiration from dry leaves considerably reduces the Bowen ratio during daylight hours. Figure 3.2.2 shows heat and water flows in the analogy of an electric circuit.

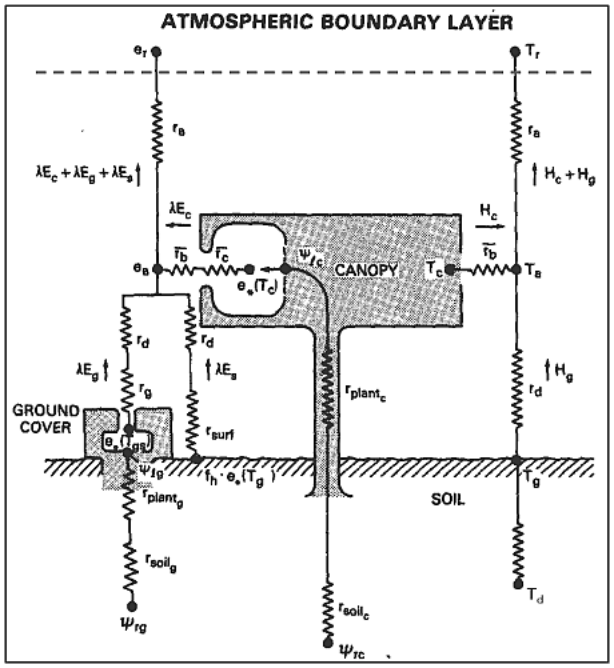

Figure 3.2.2: Schematic illustration of SiB. The temperature T_a and the specific humidity q_a of the canopy space are related to variables at the lowest level of the model grid by the surface boundary layer scheme (Modified from Sellers *et al.* (1986)).

The governing equations for the canopy temperature T_c, the ground surface temperature T_g and the deep soil temperature T_d are

$$C_c \frac{\partial T_c}{\partial t} = R_c^n - H_c - \lambda E_c \tag{3.2.71}$$

$$C_g \frac{\partial T_g}{\partial t} = R_g^n - H_g - \lambda E_g - \frac{2\pi C_g}{\tau_D}\left(T_g - T_d\right) \tag{3.2.72}$$

$$\frac{\partial T_d}{\partial t} = -\frac{2\pi}{\sqrt{365}\,\tau_D}\left(T_d - T_g\right) \tag{3.2.73}$$

where C is heat capacity, R^n is net radiation, H is sensible heat, E is the evapotranspiration rate, λ is the latent heat of evaporation of water, and τ_D is the length of the day. The suffixes c, g and d denote the canopy, the ground/ground grass and the deep soil, respectively. T_g and T_d are predicted using the force-restore method (Deardorff 1978). The initial conditions of T_c, T_g and T_d are those of the first guess, the 6-hour forecast initiated 6 hours before.

Water storage on leaves of the canopy M_c and the ground grass M_g are predicted using

$$\frac{\partial M_c}{\partial t} = P_c - D_c - \frac{E_{wc}}{\rho_w} \tag{3.2.74}$$

$$\frac{\partial M_g}{\partial t} = P_g - D_g - \frac{E_{wg}}{\rho_w} - \delta M_{\mathrm{sn}} \tag{3.2.75}$$

where P represents precipitation over leaves, D is water drainage from leaves, E_w is the evaporation of liquid water on leaves, ρ_w is water density and δM_{sn} is the amount of snow melt. When T_c (T_g) is below the freezing point of water, M_c (M_g) represents ice on canopy leaves (snow water equivalent on the ground).

Soil moisture is predicted in three layers. Vegetation draws water from the soil and transfers it directly to the air. In this relation, stomatal resistance (which depends on soil moisture, humidity and solar radiation intensity) considerably controls transpiration. The prognostic equations used for soil moisture in each layer are as follows:

$$\frac{\partial W_1}{\partial t} = \frac{1}{\delta_s D_1}\left\{P_1 - Q_{1,2} - \frac{1}{\rho_w}E_s\right\} \tag{3.2.76}$$

$$\frac{\partial W_2}{\partial t} = \frac{1}{\delta_s D_2}\left\{Q_{1,2} - Q_{2,3} - \frac{1}{\rho_w}\left(E_{dc,2} + E_{dg,2}\right)\right\} \tag{3.2.77}$$

$$\frac{\partial W_3}{\partial t} = \frac{1}{\delta_s D_3}\left\{Q_{2,3} - Q_3 - \frac{1}{\rho_w}\left(E_{dc,3} + E_{dg,3}\right)\right\} \tag{3.2.78}$$

where W_i is the soil moisture wetness of the i-th soil layer, δ_s is soil porosity, D_i is the thickness of the i-th soil layer, P_1 is infiltration of precipitation, $Q_{i,j}$ is the water flux caused by the difference in matric potential between the i-th and j-th soil layers, Q_3 is gravitational drainage, E_s is evaporation from bare soil, $E_{dc,i}$ is water drawn from the i-th soil layer by canopy transpiration, and $E_{dg,i}$ is that drawn by ground grass transpiration. The first soil layer is the top one. The surface overflow and the gravitational drainage of water are counted as the run-off Q_r as follows:

$$Q_r = P_0 - P_1 + Q_3 \tag{3.2.79}$$

where

$$P_0 = P_{\mathrm{total}} - \left(P_c + P_g\right) + \left(D_c + D_g\right) \tag{3.2.80}$$

P_{total} is total precipitation and P_0 is precipitation reaching the ground. P_1 is limited due to the hydraulic conductivity of saturated soil. The initial condition for soil moisture is based on climatological data published by Willmott *et al.* (1985). Snow depth data from Snow Depth Analysis (see Section 2.8) are used to set the initial value of snow water equivalent M_g, assuming a constant snow density of 200kg/m^3.

SiB is connected to the surface boundary layer scheme through the temperature T_a and the specific humidity q_a of the canopy space. Roughness lengths are based on the vegetation types in the SiB scheme.

3.2.10 Parallelization

In the GSM, Open Multiprocessing (OpenMP) is employed for shared memory parallelization, and a Message Passing Interface (MPI) is used for distributed memory parallelization. A two-dimensional decomposition method is adopted for parallelization among processes.

Figure 3.2.3 shows the schematic design of parallelization. There are five computational stages in the performance of spherical harmonic transformation and the semi-Lagrangian advection scheme, and appropriate decompositions are selected in each stage.

At the grid stage, since all vertical levels exist in a same rank for the computation of physical processes and non-linear terms of dynamical processes, variable arrays are decomposed into east-west and north-south direction. North-south decomposition follows a cyclic order, and is applied in such a way that the order of ranking is reversed alternately. This helps to mitigate load imbalances associated with physical parameterization and the number of grid points, since their computational loads depend mainly on latitudinal zones. At the Fourier stage, since all east-west grid points exist in a same rank for the performance of Fourier transformation, variable arrays are decomposed into north-south and vertical direction. At the Legendre stage, since all north-south grid points exist in a same rank for the performance of Legendre transformation, variable arrays are decomposed into vertical and longitudinal wavenumber direction. At the wavenumber stage, since all vertical levels exist in a same rank for the solution of Helmholtz equations in the semi-implicit scheme, variable arrays are decomposed into longitudinal and total wavenumber direction. Communication among these four stages can be performed independently within each subset based on the provision of two restrictions for the number of decompositions: 1) the number of decompositions for the east-west direction, the vertical direction and the total wavenumber direction must be the same, and 2) the number of decompositions for the north-south direction and the longitudinal wavenumber direction must be the same.

At the horizontal advection stage, variable arrays are decomposed into vertical and north-south direction. To reduce the amount of communication relating to halo regions, the number of decompositions for the north-south direction is made as small as possible. Unlike communication in the stages described above, global communication is required for interaction between the grid stage and the horizontal advection stage.

3.2.11 Surface Boundary Conditions

Model topography is derived from GTOPO30 data, while land-sea distribution is determined in reference to the Global Land Cover Characteristics (GLCC) database compiled by the U.S. Geological Survey (USGS) and others. Vegetation types are based on Dorman and Sellers (1989).

Analyzed daily sea surface temperature (SST) (see Section 5.2) data and sea ice concentration (SIC) are used as initial conditions for the sea surface in the GSM. The amount of change in these variables during the temporal integration of the model is equivalent to the time interpolated variation in monthly climatological data given by the NOAA OI SST (Reynolds and Smith 1994) and the climatological SIC derived using the method of Nomura (1998). A sea area where SIC exceeds 55% is regarded as a sea ice area in the GSM.

3.2.12 Initial Conditions

The initial conditions for zonal wind, meridional wind, temperature, specific humidity and surface pressure are provided from 4D-Var global objective analysis (see Section 2.5). The initial conditions for cloud water content, cloud cover (for radiation), convective mass flux at cloud base, canopy temperature, ground surface temperature and deep soil temperature are those of the first guess. Soil moisture data in the first step are climatological values. The value obtained from snow depth analysis (see Section 2.8) is used to determine the initial snow water equivalent and to adjust the initial ground surface temperature.

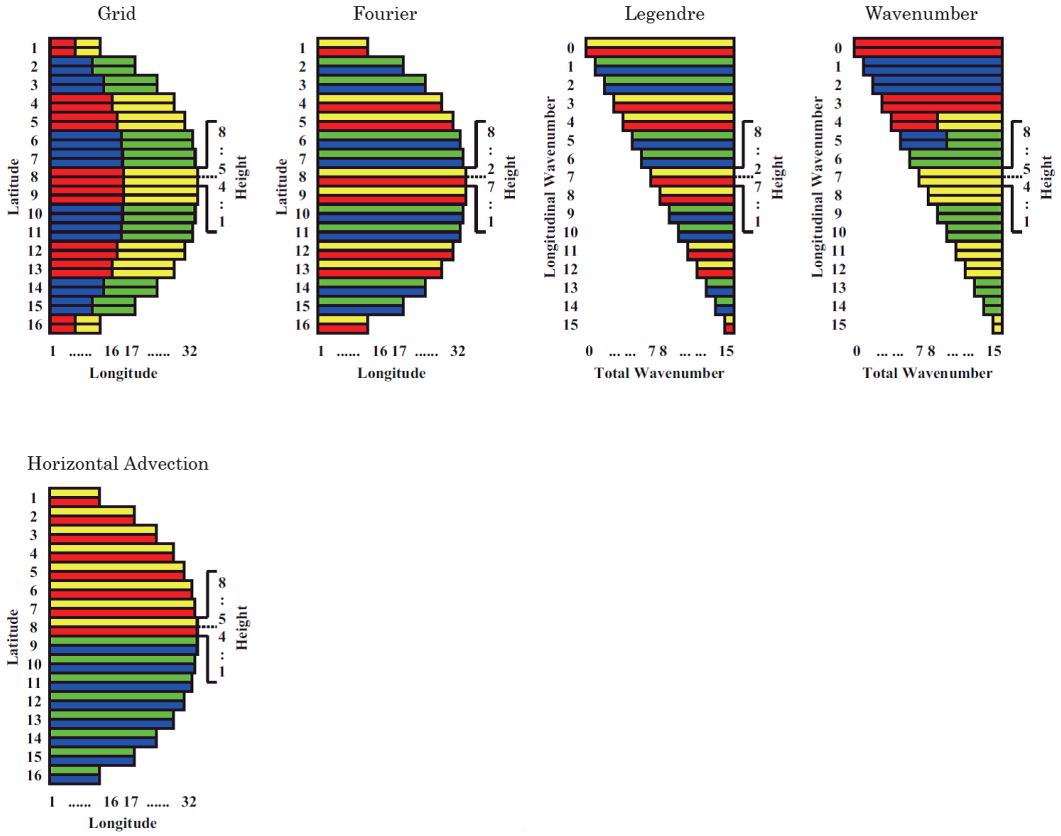

Figure 3.2.3: Schematic design of the parallelization. The number of processes used is assumed to be 4 in this example. Colors in the figure represent the rank for the computation in that area; red is rank 0, yellow is rank 1, blue is rank 2 and green is rank 3.

3.2.13 Forecast Performance

Figure 3.2.4 shows Root Mean Square Error (RMSE) for 24, 72 and 120 hours forecast of 500hPa geopotential height against analysis in the northern hemisphere extra-tropics. Dashed lines indicate the monthly means and solid lines represent 13-month running means. Substantial improvements of the forecast performance are seen at the timing of the upgrades of GSM (see Subsection 3.2.1).

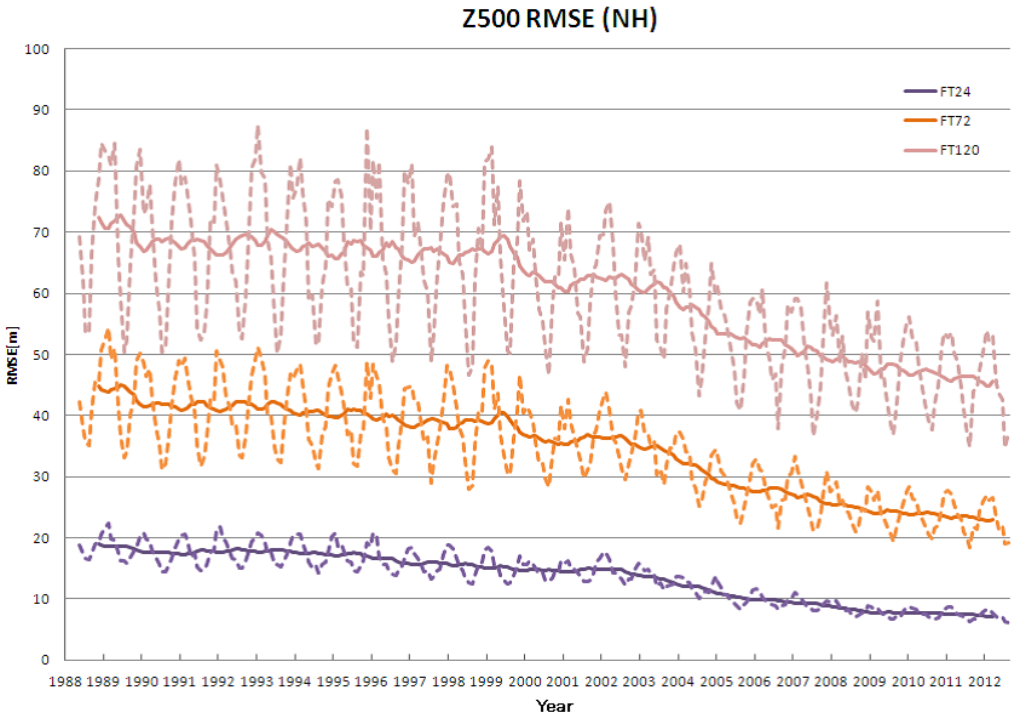

Figure 3.2.4: Root Mean Square Error of GSM 500hPa geopotential height predictions (Z500) against analysis in the northern hemisphere extra-tropics (20°N – 90°N). Dashed lines indicate the monthly means, and solid lines represent 13-month running means.

The predictions of tropical cyclone (TC) track and central pressure are verified against the best track analyzed by the RSMC Tokyo - Typhoon Center in JMA. The mean position error of TC track predictions of GSM in the western North Pacific is shown in Figure 3.2.5. It is found that the mean position error is gradually reduced during the period from 1996 through 2011 corresponding to the improvements of GSM, but with the inter-annual variations of TC occurrences and so on. Figure 3.2.6 shows the bias and Root Mean Square Error (RMSE) of central pressure predictions for 2010 and 2011. The differences of the performance of TC central pressure predictions between 2010 and 2011 appear to be the inter-annual variations.

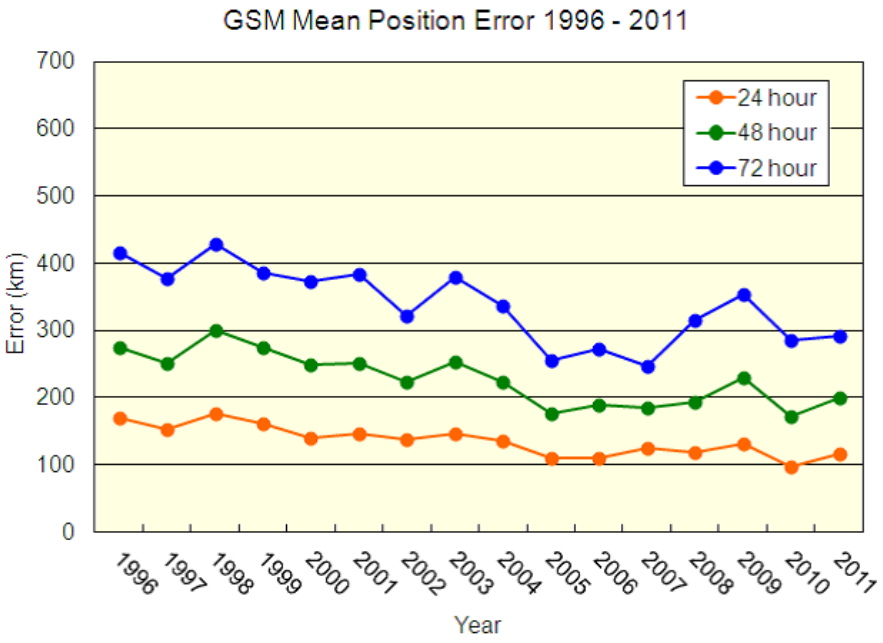

Figure 3.2.5: Mean position error of TC track predictions of GSM in the western North Pacific from 1996 to 2011. The lines represent 24 hours forecast (red), 48 hours forecast (green), and 72 hours forecast (blue), respectively.

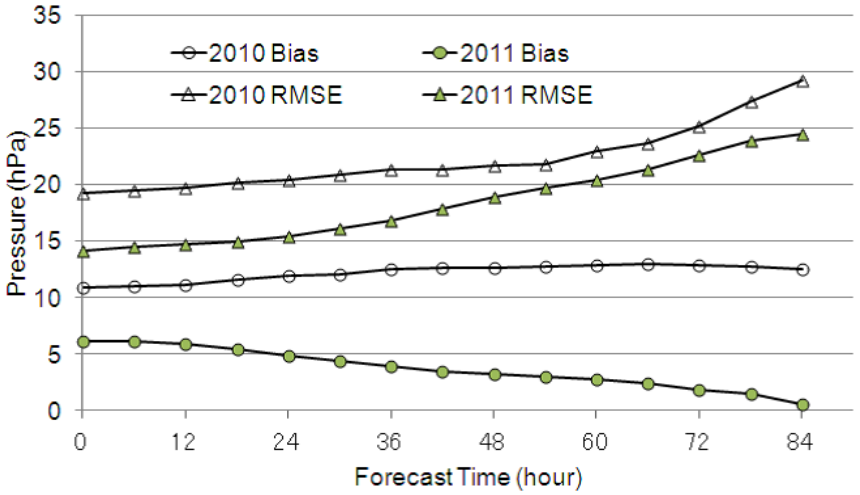

Figure 3.2.6: Bias and RMSE of TC central pressure predictions of GSM in the western North Pacific for 2010 and 2011. The horizontal axis is forecast time, and the vertical axis is TC central pressure. The circles and the triangles indicate bias and RMSE, respectively.

3.3 Ensemble Prediction Systems

3.3.1 Introduction

JMA routinely operates ensemble prediction systems (EPSs) to support forecasting work. As well as covering a wide range of prediction periods from early medium-range to seasonal forecasting, JMA's suite of EPSs supports the issuance of five-day tropical cyclone (TC) track forecasts. Totals of 11, 51 and 50 initial conditions are integrated using a low-resolution version of JMA's Global Spectral Model (GSM) to produce an ensemble of 132-hour forecasts in the Typhoon EPS, 11-day forecasts in the One-week EPS, and 34-day forecasts in the One-month EPS, respectively. In addition, 51 initial conditions are integrated using JMA's coupled Atmosphere-ocean General Circulation Model (CGCM) to produce an ensemble of 120-day forecasts (covering 210 days five times a year) in the Seasonal EPS.

3.3.2 In Operation

3.3.2.1 System Configuration

The specifications of all JMA's operational EPSs are shown in Table 3.3.1.

Table 3.3.1: Specifications of JMA EPSs

		Typhoon EPS	One-week EPS	One-month EPS	Seasonal EPS
Integration	Start of operation	February 2008	March 2001	March 1996	March 2003
	Ensemble size	11	51	50	51
	Initial time	00, 06, 12 and 18 UTC	12 UTC	12 UTC	00 UTC
	Forecast range	132 hours	11 days	17 days on Sundays and Mondays/34 days on Wednesdays and Thursdays	7 months
EPS model	Model type	GSM (an atmospheric general circulation model)			GSM coupled with the Meteorological Research Institute Community Ocean Model (MRI.COM) (a coupled atmosphere-ocean general circulation model)
	Horizontal resolution	TL319[†] reduced Gaussian grid system[‡] roughly equivalent to 0.5625° × 0.5625° (55 km) in latitude and longitude		TL159 reduced Gaussian grid system roughly equivalent to 1.125° × 1.125° (110 km) in latitude and longitude	GSM: TL95 Gaussian grid system roughly equivalent to 1.875° × 1.875° (180 km) MRI.COM: 1.0° × 1.0° in latitude and longitude
	Vertical resolution (model top)	60 levels (0.1 hPa)			GSM: 40 levels (0.4 hPa) MRI.COM: 50 levels
Atmospheric ensemble setting	Initial perturbation generator	Singular vector method		Combination of the breeding of growing modes (BGM) method and the lagged average forecasting (LAF) method (25 BGMs and 2 initial dates with 1-day LAF)	Combination of the BGM method and the LAF method (9 BGMs and 6 initial dates with 5-day LAF)
	Initial perturbed area	Northwestern Pacific (20°N–60°N, 100°E–180°) and the vicinities of up to 3 TCs	Globe	The Northern Hemisphere (20°N–90°N) and the tropics (20°S–20°N)	
	Model ensemble method	Stochastic physics scheme		*Not introduced*	

[†]TL319 is an abbreviation of spectral triangular truncation 319 with a linear grid. The spectral method is described in Subsection 3.2.2.
[‡]The reduced Gaussian grid is described in Subsection 3.2.2.

A low-resolution version of the GSM is used in the Typhoon EPS, the One-week EPS and the One-month EPS. Accordingly, the dynamical framework and physical processes involved are identical to those of the GSM (see Section 3.2) except for the horizontal resolution. Each unperturbed analysis is prepared by interpolating the analyzed field in global analysis (see Section 2.5). The sea surface temperature analysis value (see Section 5.2) is used as a lower boundary condition and prescribed using the persisted anomaly, which means that the anomalies shown by analysis for the initial time are fixed during the time integration. The sea ice concentration analysis value is also prescribed using the persisted anomaly except with the One-month EPS, in which sea ice climatology is adopted as a lower boundary condition.

The CGCM (see Section 3.4) is used in the Seasonal EPS. Unperturbed analysis for this EPS is obtained from the JMA Climate Data Assimilation System (JCDAS) (see Section 2.10) and the ocean data assimilation system (MOVE/MRI.COM-G) (see Section 5.3).

The model's systematic bias is removed from the model results both for One-Month Forecasts and Seasonal Forecasts. The bias is estimated in advance from the mean forecast error obtained from hindcast experiments.

3.3.2.2 Frequency

The frequency of operation differs with each EPS as detailed below.

1. Typhoon EPS

   The Typhoon EPS consists of 11 forecasts run up to four times a day from base times at 00, 06, 12 and 18 UTC with a forecast range of 132 hours. The system is operated when any of the following conditions is satisfied:

   - A TC of tropical storm (TS[1]) intensity or higher is present in the RSMC Tokyo - Typhoon Center's area of responsibility (0°–60°N, 100°E–180°).
   - A TC is expected to reach TS intensity or higher in the area within the next 24 hours.
   - A TC of TS intensity or higher is expected to move into the area within the next 24 hours.

2. One-week EPS

   The One-week EPS consists of 51 forecasts run once a day from a base time at 12 UTC with a forecast range of 11 days.

3. One-month EPS

   The One-month EPS consists of 25 forecasts run four times a week on Sundays, Mondays, Wednesdays and Thursdays from a base time at 12 UTC. The range of the forecasts run on Sundays/Mondays is 17 days, and that of the Wednesday/Thursday forecasts is 34 days. A 50-member lagged ensemble with a forecast range of one month is used for the One-month Forecast issued on Fridays. A 50-member lagged ensemble with a forecast range of two weeks is used for the Early Warning Information on Extreme Weather, which is issued on Tuesdays and Fridays when a high probability of very high or very low seven-day averaged temperatures is predicted in the week starting from five to eight days ahead of the date of announcement.

4. Seasonal EPS

   The Seasonal EPS consists of nine forecasts run every five days from a base time at 00 UTC with a forecast range of seven months. A 51-member lagged ensemble is used for the Three-month Forecast issued every month and for the Warm/Cold Season Forecast issued five times a year (in February, March, April, September and October). The EPS is also used for the El Niño Outlook issued every month.

[1] A TS is defined as a TC with maximum sustained wind speeds of 34 knots or more and less than 48 knots.

Table 3.3.2: SV calculation specifications

	One-week EPS			Typhoon EPS	
Resolution	Spectral triangular truncation 63 (T63), 40 levels				
Norm	Moist total energy				
Target area	Northern Hemisphere (30°N–90°N)	Southern Hemisphere (90°S–30°S)	Tropics (30°S–30°N)	Northwestern Pacific (20°N–60°N, 100°E–180°)	Vicinities of up to 3 TCs in the Typhoon Center's area of responsibility
Physical process	Simplified physics		Full physics	Simplified physics	Full physics
Optimization time	48 hours		24 hours	24 hours	24 hours
Evolved SV	Used			Not used	Not used
Number of perturbations	25			10	10 for each TC

3.3.3 Approach to Ensemble Initial Conditions

Two methods are employed to perturb the initial conditions for the atmosphere. One is the singular vector (SV) method (Buizza and Palmer 1995), which is used for both the One-week EPS and the Typhoon EPS as initial perturbation generators. The other is the breeding of growing modes (BGM) method (Toth and Kalnay 1993, 1997), which is used for both the One-month EPS and the Seasonal EPS. The following subsections describe the specifications of these methods and outline how atmospheric ensemble initial conditions are generated for each EPS.

For the Seasonal EPS, initial perturbations for the ocean are introduced in addition to those for the atmosphere. These values are estimated using the ocean data assimilation system (MOVE/MRI.COM-G) forced with surface heat and momentum fluxes in the atmospheric initial perturbation fields.

3.3.3.1 SV Method

Table 3.3.2 summarizes the specifications of SV calculation for the One-week EPS and the Typhoon EPS. The tangent-linear and adjoint models used for SV computation are lower-resolution versions of those used in 4D-Var (see Section 2.5) until October 2011. The models involve full dynamical core and physical processes including surface fluxes, vertical diffusion, gravity wave drag, large-scale condensation, long-wave radiation and deep cumulus convection. SVs based on tangent-linear and adjoint models incorporating full physical processes are called moist SVs, while those based on models incorporating simplified physical processes involving surface fluxes and vertical diffusion are called dry SVs.

1. SV definition for the One-week EPS

   In the One-week EPS, three targeted areas are used for SV calculation: the Northern Hemisphere (30°N–90°N), the tropics (30°S–30°N) and the Southern Hemisphere (90°S–30°S). Dry SVs with a 48-hour optimization time are computed for the Northern Hemisphere and the Southern Hemisphere, and moist SVs with a 24-hour optimization time are computed for the tropics.

2. Norm of SV calculation for the One-week EPS

   In the One-week EPS, the norm for evaluating the growth rate of dry and moist SVs is based on a total energy norm that includes a specific humidity term (Barkmeijer *et al.* 2001):

$$
\begin{aligned}
(x, Ey) \quad = \quad & \frac{1}{2}\int_0^1 \int_S \left[\nabla\triangle^{-1}\zeta_x \cdot \nabla\triangle^{-1}\zeta_y + \nabla\triangle^{-1}D_x \cdot \nabla\triangle^{-1}D_y + \frac{c_p}{T_r}T_x T_y \right. \\
& \left. + w_q \frac{L_c^2}{c_p T_r} q_x q_y \right] dS \left(\frac{\partial p}{\partial \eta}\right) d\eta + \frac{1}{2}\int_S \left[\frac{R_d T_r}{P_r} P_x P_y \right] dS . \qquad (3.3.1)
\end{aligned}
$$

   Here, ζ_x, D_x, T_x, q_x and P_x are the vorticity, divergence, temperature, specific humidity and surface pressure components of state vector x respectively, and (x, Ey) is an inner product of state vectors x and

y with a norm operator E. c_p is the specific heat of dry air at a constant pressure, L_c is the latent heat of condensation, and R_d is the gas constant for dry air. T_r = 300 K is a reference temperature, P_r = 800 hPa is a reference pressure, and w_q is a constant (here 0.04). $\int dS$ is the horizontal integration for the whole globe, and $\int \left(\frac{\partial p}{\partial \eta}\right) d\eta$ gives the vertical integration from the surface to the model top. In addition, the norm at the initial time is vertically integrated with a weight that depends on the model level; the kinetic energy term and the available potential energy term are multiplied by a factor of 10^3 above the 35th model level, and the specific humidity term is multiplied by a factor of 10^3 above the 9th model level. When the surface pressure is 1,000 hPa, the 35th and 9th model levels correspond to about 10 and 750 hPa, respectively. This suppresses initial perturbation around the model top and confines initial specific humidity perturbation in the lower troposphere.

3. Generation of initial perturbations for the One-week EPS

   The initial conditions of 50 perturbed members are given by adding and subtracting 25 initial perturbations to unperturbed analysis. The initial perturbations are linear combinations of SVs (initial SVs) and evolved SVs. These evolved SVs are calculated by linearly growing previous initial SVs (with an initial time earlier than the current one by an amount equivalent to the optimization time) to the current initial time. A total of 25 initial SVs are created for each targeted area. In this creation procedure, SVs with extremely high growth rates (which will not grow sufficiently in a nonlinear model) and SVs with a high level of similarity to others can be eliminated. Here too, 25 evolved SVs are created for each targeted area. Before the initial and evolved SVs are combined, the evolved ones are approximately orthogonalized with initial SVs and other evolved SVs, and are normalized to a size twice that of the initial SVs. The 25 combined SVs are transformed in a variance minimum rotation (Yamaguchi *et al.* 2009) to generate 25 initial perturbations for each targeted area. The perturbations for the Northern Hemisphere and the Southern Hemisphere are scaled so that their amplitudes of temperature at the 15th model level (or the 6th model level for the tropics) inside the targeted area become 0.3 K. When the surface pressure is 1,000 hPa, the 15th and 6th model levels correspond to about 500 and 850 hPa, respectively. Global perturbations representing linear combinations of the perturbations for the three targeted areas are used as initial perturbations for perturbed members.

4. SV definition for the Typhoon EPS

   Two SV calculations are introduced into the system to efficiently capture the uncertainty of TC track forecasts. One produces dry SVs with a spatial target area fixed on the Northwestern Pacific (20°N–60°N, 100°E–180°), and the other produces moist SVs whose spatial target area can be moved within a 750-km radius of a predicted TC's position in one-day forecasting. Up to three movable areas can be configured for different TCs at one initial time. If more than three TCs are present in the area of responsibility, three are selected in the order of concern as prioritized by the RSMC Tokyo - Typhoon Center.

5. Norm of SV calculation for the Typhoon EPS

   For the Typhoon EPS, the total energy norm is defined by:

$$
\begin{aligned}
(x, Ey) \quad = \quad & \frac{1}{2} \int_0^1 \int_S \left[\nabla\triangle^{-1}\zeta_x \cdot \nabla\triangle^{-1}\zeta_y + \nabla\triangle^{-1}D_x \cdot \nabla\triangle^{-1}D_y + \frac{g\,(\Gamma - \Gamma_d)^{-1}}{T_r} T_x T_y \right. \\
& \left. + w_q \frac{L_c^2}{c_p T_r} q_x q_y \right] dS \left(\frac{\partial p}{\partial \eta}\right) d\eta + \frac{1}{2} \int_S \left[\frac{R_d T_r}{P_r} P_x P_y \right] dS. \qquad (3.3.2)
\end{aligned}
$$

   Here, g is gravity acceleration, Γ_d is the dry adiabatic temperature lapse rate and $\Gamma = \frac{2}{3}\Gamma_d$ is a constant referential temperature lapse rate. Here, w_q = 1. In Eq. (3.3.2), the vertical integration of the kinetic energy term and the available potential energy term is limited to the 26th model level, and the specific humidity term can be limited to the 15th model level. When the surface pressure is 1,000 hPa, the 26th and 15th model levels correspond to about 100 and 500 hPa, respectively. Otherwise, as reported

by Barkmeijer *et al.* (2001), SVs would have a shallow vertical structure in the upper troposphere or a large specific humidity contribution in the upper troposphere where the amount of specific humidity is relatively small. As such SVs have little influence on TC track forecasts, the limit on vertical integration is set as detailed in Eq. (3.3.2).

6. Generation of initial perturbations for the Typhoon EPS

   Initial perturbations are determined by combining dry and moist SVs linearly. Each SV calculation can produce up to 10 SVs depending on how accurate SV estimates are, which makes the maximum number of SVs 40 (i.e., 10 dry SVs for the fixed area and 30 moist SVs for 3 movable areas) for each forecast event. Before the binding coefficients are determined, SVs with structures similar to those of others are eliminated. When the value of the inner product of any two SVs is 0.5 or more, one of them is eliminated from the group of SV candidates to be used for initial perturbations. After this process, the coefficients are determined based on variance minimum rotation, which creates a wide spread in the spatial distributions of the perturbations. If no SVs are eliminated, the number of independent initial perturbations is the same as the number of SVs computed. Five perturbations are randomly selected from the initial perturbations and added to/subtracted from the analysis field to produce 10 perturbed initial conditions. The amplitude of the perturbations is normalized using the moist total energy value.

3.3.3.2 BGM Method

The processes of the BGM method with separate estimation for the Northern Hemisphere (20°N–90°N) and the tropics (20°S–20°N), are described here. First, perturbed and unperturbed initial conditions are integrated up to 12 hours for the Northern Hemisphere and 24 hours for the tropics. Then, the difference between the two fields is normalized so that the area-averaged root mean square of the difference for 500-hPa height over the Northern Hemisphere and 200-hPa velocity potential for the tropics are equal to 14.5 and 20.0 % of the climatological variance, respectively. Third, the normalized perturbations are orthogonalized to each other and added to the analysis to create the next set of initial perturbations. In both the One-month EPS and the Seasonal EPS, the Northern Hemisphere and tropical initial perturbations are combined and added to/subtracted from the analysis.

3.3.4 Model Ensemble Approach

The stochastic physics scheme (Buizza *et al.* 1999) is used in the One-week EPS and the Typhoon EPS in consideration of model uncertainties associated with physical parameterizations. This scheme represents random errors associated with parameterized physical processes as follows:

$$\frac{\partial \mathbf{x}}{\partial t} = F(\mathbf{x}) + \alpha(\lambda, \phi, t)P(\mathbf{x}). \tag{3.3.3}$$

Here t, $\mathbf{x}$, $F(\mathbf{x})$ and $P(\mathbf{x})$ are the time, the set of forecast variables, the total tendency of the forecast model and the tendency of the parameterized physical processes, respectively. λ and ϕ show latitude and longitude; $\alpha(\lambda, \phi, t)$ is a random variable described in a spectral space (Berner *et al.* 2009) featuring spatial correlation with a total wave number of 20 and a time correlation of six hours. The average of α is set to zero. Its value is limited to the range from -0.7 to 0.7 to avoid excess perturbation, and its value in the stratosphere is also set to zero.

3.3.5 Performance

The performance of each EPS product is described below.

3.3.5.1 One-week EPS

The results of verification regarding One-week EPS output are published in the annual WMO Technical Progress Report on the Global Data-processing and Forecasting System (GDPFS). Monthly verification data

are also published on the website of the WMO/CBS Lead Centre for EPS Verification[2].

Figure 3.3.1 shows root mean square errors (RMSEs) for the 500-hPa geopotential height ensemble mean forecast against analysis for the Northern Hemisphere (NH; 20°N–90°N) averaged for the periods of DJF (December/January/February) of 2011/2012 and JJA (June/July/August) of 2012. Figure 3.3.2 compares the monthly-averaged RMSEs of the ensemble means, unperturbed members and the spread of the ensemble. A higher level of skill is observed for ensemble means than for deterministic forecasts, especially for longer lead times. Figure 3.3.3 shows the Brier skill score (BSS) for 500-hPa geopotential height probabilistic forecasts in the NH. The reference forecast for the skill score is the climatological probability given by the frequency derived from the analysis fields for each month. Since the start of its operation, the performance of the One-week EPS has been improved year after year in ensemble mean forecasts and probabilistic forecasts.

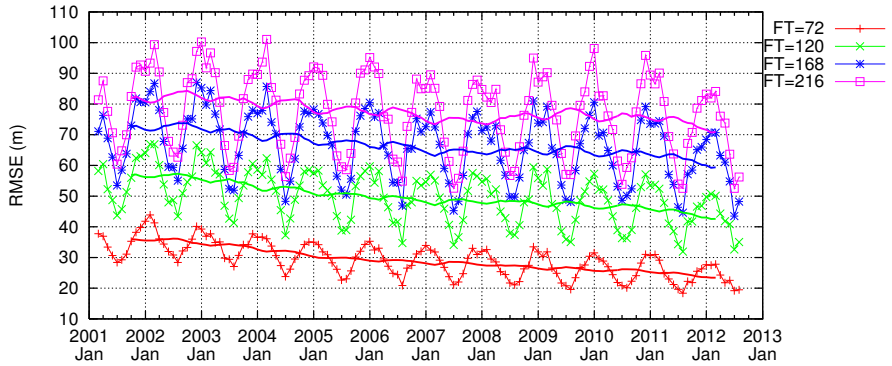

Figure 3.3.1: Time-series representation of ensemble mean scores for JMA's One-week EPS (where the score is the monthly-averaged RMSE of the ensemble mean) for Northern Hemisphere (20°N–90°N) 500-hPa geopotential height forecasts with lead times of 72, 120, 168 and 216 hours from March 2001 to August 2012. The thick lines show 13-month running means.

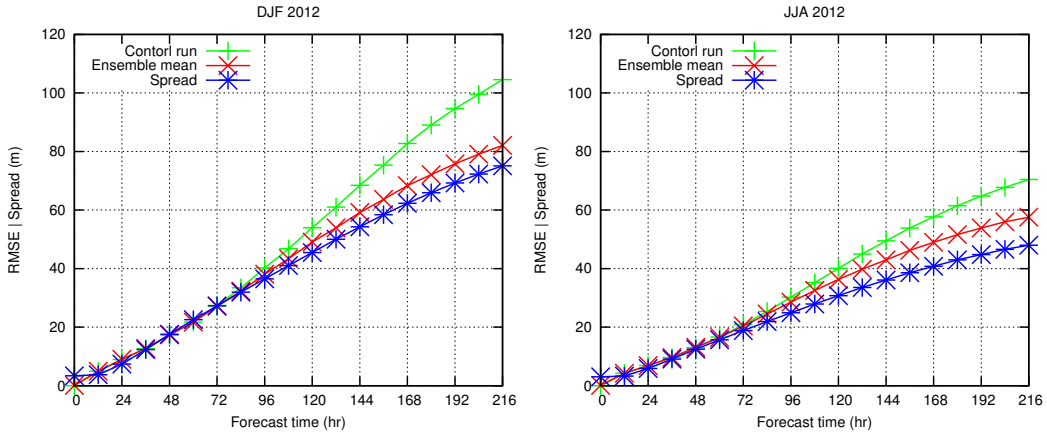

Figure 3.3.2: RMSEs for Northern Hemisphere (20°N–90°N) 500-hPa geopotential height forecasts of the ensemble mean (red) and unperturbed members (green) for DJF and JJA 2012 from JMA's One-week EPS. The spread of the ensemble (blue) is also shown.

[2] http://epsv.kishou.go.jp/EPSv/

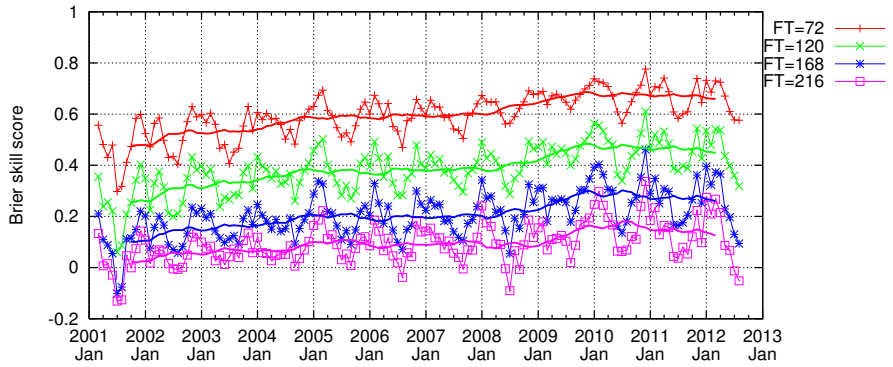

Figure 3.3.3: Time-series representation of Brier skill score for probabilistic forecasts of 500-hPa geopotential height negative anomalies with magnitudes less than one climatological standard deviation over the Northern Hemisphere (20°N–90°N) for lead times of 72 (red), 120 (green), 168 (blue) and 216 (violet) hours from March 2001 to August 2012 from JMA's One-week EPS. The thick lines show 13-month running means.

3.3.5.2 Typhoon EPS

The results of verification regarding Typhoon EPS output are published in the Annual Report on Activities of the RSMC Tokyo - Typhoon Center [3].

Ensemble TC tracks derived from the Typhoon EPS enable JMA forecasters to integrate TC track forecast uncertainty into their operational processes. Strike probability data, which indicate the chances of a TC center passing within 120 km of a grid point, are routinely produced as a form of probabilistic guidance. Figure 3.3.4 shows the reliability of typhoon strike probability data during next five days. The curves for the previous three-year period indicate similar levels of performance. However, the 2008 curve shows relatively high departure from the diagonal, especially in low-probability areas where the forecast frequency is quite large.

3.3.5.3 One-month EPS

The results of prediction skill evaluation based on hindcast experiments and real-time forecasts are available on the Tokyo Climate Center website [4]. To verify performance, hindcast experiments covering a period of 31 years (1979–2009) were conducted under conditions identical to those of the operational system, except with an ensemble size of 5 instead of 50. The skill of ensemble mean forecasts was evaluated using the Anomaly Correlation Coefficient (ACC) and the RMSE for selected areas with respect to several physical variables. Probabilistic forecast skill was also evaluated based on the BSS, the Reliability Skill Score (Brel), the Resolution Skill Score (Bres) and the Relative Operating Characteristics (ROC).

Figure 3.3.5 shows the time-series representation of the NH 500-hPa geopotential height ACC for ensemble mean forecasts averaged over 28 days (the running mean of 52 forecasts) based on operational forecasting conducted from 1996 to 2011. It can be seen that skill in the NH shows a rising trend from 1999 onward. Although ensemble mean skill is sensitive to initial conditions, it is almost consistently higher than that of persistence forecasts. Table 3.3.3 shows ROC areas of 2-m temperature (T2m) and precipitation anomalies based on the outcomes of hindcast experiments covering a 31-year period (1979–2009), and indicates that skill for the tropics is higher than that for the extratropics.

3.3.5.4 Seasonal EPS

The results of prediction skill evaluation based on the WMO Standard Verification System for long-range forecasts (SVS-LRF; WMO 2010b) are available on the Tokyo Climate Center website. To verify performance,

[3] http://www.jma.go.jp/jma/jma-eng/jma-center/rsmc-hp-pub-eg/annualreport.html
[4] http://ds.data.jma.go.jp/tcc/tcc/index.html

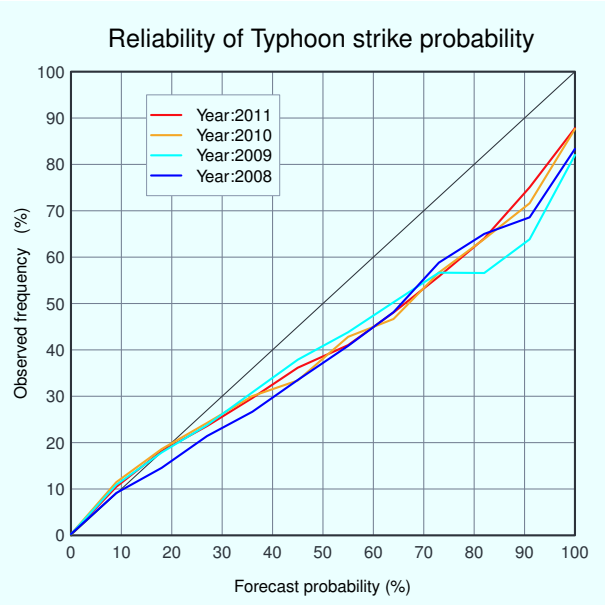

Figure 3.3.4: Reliability diagram for probabilistic verification of typhoon position forecasts as derived from the Typhoon EPS over a four-year period. The target years for verification are 2008 (blue), 2009 (sky blue), 2010 (orange) and 2011 (red). RSMC Tropical Cyclone Best Track information is used as observation data.

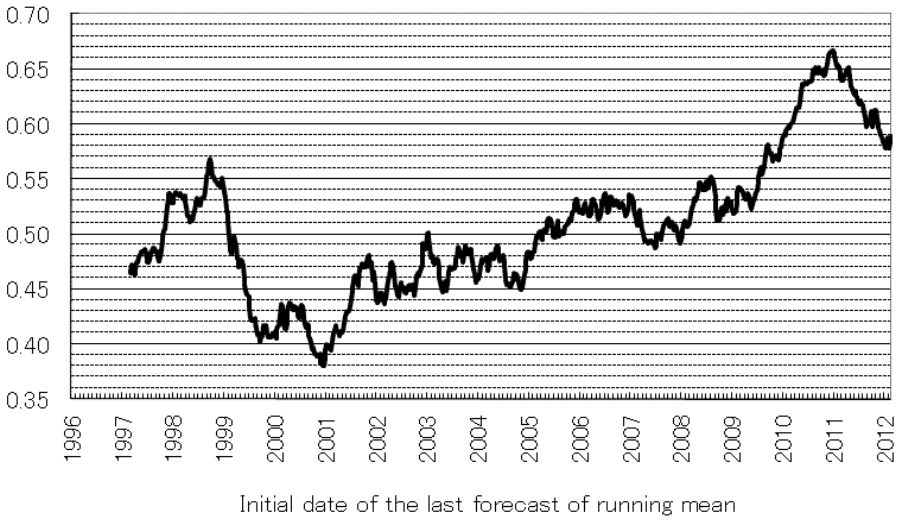

Figure 3.3.5: Time-series representation of the Northern Hemisphere (NH; 20°N–90°N) 500-hPa geopotential height anomaly correlation coefficient in ensemble mean forecasts averaged over 28 days (the running mean of 52 forecasts) based on operational forecasting conducted from 1996 to 2011

Table 3.3.3: ROC areas of 28-day mean 2-m temperature (T2m) and precipitation anomaly prediction for positive anomaly events (upper tercile) in the Northern Hemisphere (NH; 20°N–90°N), the tropics (20°S–20°N), and the Southern Hemisphere (SH; 90°S–20°S) based on hindcast experiments covering a period of 31 years (1979–2009). The figures in the table are multiplied by 100. The initial dates are 31 December for January and 30 June for July.

T2m	NH	Tropics	SH
January(Initial:12/31)	75.9	76.4	69.8
July(Initial:6/30)	71.6	74.3	68.8

Precipitation	NH	Tropics	SH
January(Initial:12/31)	63.0	64.4	56.1
July(Initial:6/30)	58.8	64.0	57.3

hindcast experiments covering a period of 30 years (1979–2008) were conducted under conditions identical to those of the operational system, except with an ensemble size of 10 instead of 51. Figure 3.3.6 shows the ACC between ensemble mean forecasts and observations for SSTs in the NINO3 (5°S–5°N, 150°W–90°W), NINO.WEST (0°–15°N, 130°E–150°E) and IOBW (20°S–20°N, 40°E–100°E) regions. SSTs in these areas are predicted well with the CGCM. Although not shown in Figure 3.3.6, the skill for NINO3.4 SSTs is comparable to those of major state-of-the-art seasonal forecast models (Jin *et al.* 2008). ROC areas of T2m anomalies and precipitation anomalies are shown in Table 3.3.4. The level of skill for T2m is better than that of precipitation in all regions, and skill in the tropics is better than that in the NH and the Southern Hemisphere (SH; 90°S–20°S). These results are consistent with those obtained from studies on the predictability of seasonal mean fields (e.g., Sugi et al. 1997).

Table 3.3.4: ROC areas of three-month means (JJA and DJF) 2-m temperature (T2m) and precipitation anomaly prediction for positive anomaly events (upper tercile) in the Northern Hemisphere (NH; 20°N–90°N), the tropics (20°S–20°N), and the Southern Hemisphere (SH; 90°S–20°S) based on hindcast experiments covering a period of 30 years (1979–2008). The figures in the table are multiplied by 100. The initial dates are 1 May for JJA and 28 October for DJF.

T2m	NH	Tropics	SH
JJA(Initial:5/1)	63.8	73.9	61.3
DJF(Initial:10/28)	63.5	77.1	61.2

Precipitation	NH	Tropics	SH
JJA(Initial:5/1)	52.3	64.9	55.6
DJF(Initial:10/28)	56.0	62.7	53.8

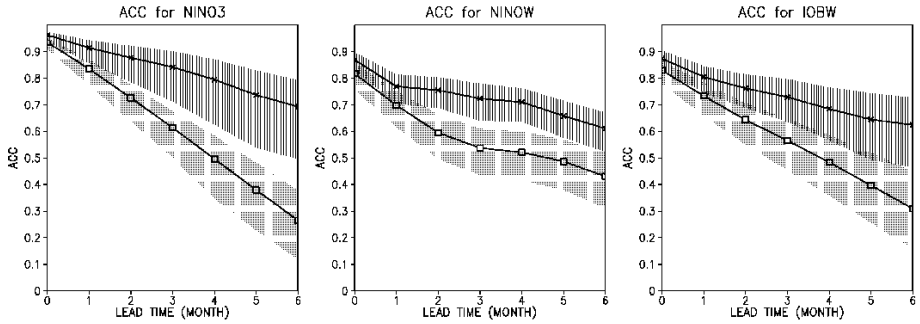

Figure 3.3.6: Anomaly correlations for SSTs over (a) NINO3 (5°S–5°N, 150°W–90°W), (b) NINO.WEST (0°–15°N, 130°E–150°E) and (c) IOBW (20°S–20°N, 40°E–100°E). Crosses indicate scores for CGCM predictions, and squares indicate those for anomaly persistent predictions. Shading indicates a 90% confidence interval as estimated using the bootstrap method.

3.4 Coupled Atmosphere-Ocean General Circulation Model

3.4.1 Model Description

Since July 1998, JMA has used atmosphere-ocean coupled general circulation models (CGCMs) to predict the phenomenon of El Niño-Southern Oscillation (ENSO). The current CGCM (JMA/MRI-CGCM) introduced in February 2008 was developed in collaboration with the Meteorological Research Institute (MRI). In February 2010, the ENSO Prediction System and the Seasonal Prediction System were integrated, and CGCM products have since been commonly used for operational seasonal forecasting and ENSO prediction.

The model consists of atmospheric and oceanic components and a coupler. The atmospheric component is based on a low-resolution version of JMA's Global Spectral Model (GSM0603; JMA 2007), which has a horizontal resolution of TL95 (triangular truncation at total wavenumber 95 with a linear grid) corresponding to 180-km grid spacing and 40 levels in the vertical direction with its top at 0.4 hPa (corresponding to approximately 55 km).

Most physical parameterization schemes relating to atmospheric components remain unchanged unless schemes have resolution dependency or shortcomings in coupled simulations. Several modifications have been made so that the CGCM can better represent atmospheric and oceanic states. Cumulus convection and cloud schemes can be tuned to improve the climatology of precipitation and radiative budgets, and gravity wave drag parameterization can be adjusted to the resolution of the CGCM, whose specifications are summarized in Table 3.4.1.

The effects of greenhouse gas forcing are incorporated via the setting of an increasing atmospheric carbon dioxide (CO_2) trend in the model. In the hindcast covering the period from 1979 to 2007 (Section 3.3), global average CO_2 concentrations during integration are specified as observed values on initial dates based on NASA/Goddard Institute for Space Studies (GISS) data (Hansen and Sato 2004). In hindcasts and real-time forecasts covering the period from 2007 onward, the observed CO_2 trend based on WMO/World Data Centre for Greenhouse Gases (WDCGC) data is added to the 2007 CO_2 value, and the CO_2 concentration specified is fixed throughout each integration. This treatment and the warming trend in ocean analysis contribute to better replication of the global warming trend in seasonal forecasts (e.g., Doblas-Reyes *et al.* 2006).

The oceanic component is the Meteorological Research Institute Community Ocean Model (MRI.COM-G; Tsujino *et al.* 2010), which is a primitive equation ocean general circulation type. The model has a horizontal resolution of $1^\circ \times 1^\circ$ in the extratropics with meridional refinement near the equator to 0.3°, and 50 vertical layers. Sophisticated model parameterizations are adopted, including a vertical diffusion scheme incorporating sea surface wave breaking effects (Noh and Kim 1999) and an isopycnal mixing scheme (Gent and McWilliams 1990). More details are given in Chapter 5.

The atmospheric and oceanic components are coupled every hour with the coupler. These components communicate ocean surface properties such as SSTs, sensible and latent heat fluxes, momentum flux, radiation flux and fresh water flux. Adjustment is applied to heat and momentum fluxes to reduce mean biases.

Atmospheric initial conditions are provided from JRA-25 reanalysis data (Onogi *et al.* 2007) and related real-time analysis from JCDAS (Section 2.10). Oceanic initial conditions are given by an ocean data assimilation system (MOVE/MRI.COM-G, Section 5.3), while land initial conditions are climatologies derived from offline land model simulations forced by ERA-15 reanalysis (Gibson *et al.* 1997). Ensemble perturbations are produced using a combination of the BGM method and the LAF technique. Further details are provided in Section 3.3.

3.5 Meso-Scale Model (JMA-MSM1206)

3.5.1 Introduction

The meso-scale numerical prediction system has been operational since March 2001 to provide information for disaster prevention and aviation safety. In the beginning of its operation, the Meso-Scale Model (MSM) was a hydrostatic spectral model which was also used as a coarser operational model in different configuration. The horizontal resolution of the MSM was 10km and the 40 vertical layers were placed at that time. The MSM produced 18-hour forecasts every 6 hours at 00, 06, 12, 18UTC.

Table 3.4.1: Specifications of the Coupled General Circulation Model

Atmospheric component	Basic equation	Primitive
	Domain	Global
	Resolution	TL95, 40 vertical levels
	Cumulus convection	Prognostic Arakawa-Schubert scheme
	Land surface process	Simple Biosphere (SiB)
	Planetary boundary layer	Mellor & Yamada Level 2
Oceanic component	Basic equation	Primitive, free surface
	Domain	Global (75°S – 75°N)
	Resolution	1°(lon) × 1°(lat), (1°(lon) × 0.3°(lat) near the equator), 50 vertical levels
	Vertical diffusion	Noh and Kim (1999)
Coupling	Frequency	Every hour
	Flux correction	For momentum and heat flux

In September 2004, the hydrostatic spectral model was replaced with a nonhydrostatic grid model. The new MSM employed full-compressible elastic equations including a map factor. The general configurations of the system such as resolution, forecast time, forecast frequency and so on, were kept almost the same to those of the previous system with the hydrostatic model.

In March 2006, simultaneously with installing a new supercomputer system, the resolutions and operation frequency of the MSM were enhanced. The new model with the 5-km horizontal grid spacing and 50 vertical layers produced 15-hour forecasts every 3 hours at 00, 03, 06, 09, 12, 15, 18, 21UTC.

Furthermore, the forecast period was extended to 33 hours four times per day out of the eight-time operations in May 2007. The extension of the forecast period made it possible for the MSM to provide 1-day ahead useful information associated to disaster prevention and aviation operations.

Accompanied with the upgrades of the system configurations such as horizontal and vertical resolution, forecast period, and update frequency, various physical processes were also refined. The improvements contributed to considerable part of the steady progress in accuracy of the forecasts, as shown in Subsection 3.5.11.

3.5.2 General Configurations

The current MSM has been operated 8 times a day and providing 15-hour forecasts at 00, 06, 12, 18 UTC, and 33-hour forecasts at 03, 09, 15, 21UTC. Its forecast domain is a rectangular flat area of 3600km by 2880km covering the Japan and its surroundings with the grid spacing of 5km, which is identical to the domain of the the 4D-Var Meso-scale Analysis (MA; see Section 2.6) as shown in Figure 2.6.2. The rectangular plane is obtained by the Lambert conformal conic map projection of the Earth sphere with the scale factor (map factor) introduced to correct the expanded or shrank distance on the plane through the projection from the sphere.

A hybrid terrain following coordinate is adopted as the vertical coordinate to reduce influences of topography as the height increases (Subsection 3.5.3). The lowest atmospheric layer is placed at the height of 20m above the surface, and the model top is set to 21,801m with 50 layers whose intervals vary linearly from 40m at the bottom to 904m at the top.

A forecast model of the MSM is the JMA nonhydrostatic model (JMA-NHM; Saito *et al.* 2006, 2007). The prognostic variables are horizontal and vertical momentum, potential temperature, pressure, mixing ratios of water vapor and hydrometeors (cloud water, cloud ice, rain, snow and graupel), number concentration of cloud ice, ground temperatures, soil water and four of the second order moments of the turbulent fluctuations (including the turbulent kinetic energy). The model is operated with 20-second time step.

Initial conditions for the model are generated by the MA, and lateral boundary conditions of the model come from forecasts produced by the GSM (Section 3.2). When the operations of the GSM finish and newer forecasts are available, the boundary conditions are updated. The MSM operations initialized with analysis at 03, 09, 15, 21UTC switch the boundary conditions to newer ones (GSM forecasts initialized at 00, 06, 12, 18UTC, respectively) and produce longer period (33 hours) forecasts taking advantage of the new boundary

conditions, while the ones initialized at 00, 06, 12, 18UTC use the same boundary conditions as the previous operation (at 21, 03, 09, 15UTC, respectively) and provide only shorter period (15 hours) forecasts.

The model terrain is set relying on the GTOPO30 data set, which is a global digital elevation model with a horizontal grid spacing of 30 arc seconds and developed by U.S. Geological Survey's EROS Data Center (EDC). In order to avoid computational instability related to steep slopes in the terrain, the terrain is smoothed so that the valid resolution of the terrain adopted in the model is 1.5 times as coarse as the resolution of the model itself.

The Global Land Cover Characteristics (GLCC) data set, again provided by EDC, helps to determine the land-sea attribute of each grid in the model. A grid with the sea fraction over 0.5 is supposed to be located on the sea. The sea fraction on each grid in the model is calculated based on the GLCC data set.

Parameters characterizing surface such as heat capacity, thermal conductivity, albedo, initial values of soil moisture and roughness are decided based on land use described by the GLCC data set as well. The National Land Numerical Information developed by the National-Land Information Office of Japan is also referred to set the parameters over the Japan.

Grids on land are further classified in terms of existence of snow. Similarly, grids on the sea can be covered by ice. It means that there are totally four categories of the surface types: land, land with snow covered, sea, sea with ice covered. Snow covered areas are analyzed with a 5-km horizontal grid spacing using the snow depth data of the Global snow depth analysis (see Section 2.8) and observations obtained through the domestic SYNOP and Automated Meteorological Data Acquisition System (AMeDAS). The snow depth given by the Global snow depth analysis is modified with the denser and frequent domestic observations assuming 60-km correlation radius in the analysis. If the snow depth is greater than 5cm, a corresponding grid is classified to be the land with snow covered. Ice covered areas are identified from the sea ice analysis conducted by the JMA. Over grids with snow or ice covered, surface parameters previously determined based on the GLCC data are modified with the predetermined values.

3.5.3 Dynamics

3.5.3.1 Basic Equations

The governing equations used in the MSM consist of non-hydrostatic, fully compressible equations on a spherical curvilinear orthogonal and a hybrid terrain-following coordinate with the shallow assumption. Details of the derivations of these equations are given in Saito *et al.* (2006).

1. Flux form momentum equations

   The equations of motion are described in the flux form:

$$\frac{\partial U}{\partial t} + \frac{m_1}{m_2}\left(\frac{\partial P}{\partial \hat{x}} + \frac{\partial G^{13} P}{\partial \hat{z}}\right) = -\mathrm{ADV}U + \mathrm{R}U, \tag{3.5.1}$$

$$\mathrm{ADV}U = m_1\left(\frac{\partial Uu}{\partial \hat{x}} + \frac{\partial Vu}{\partial \hat{y}}\right) + \frac{m_3}{m_2}\frac{\partial \hat{W}u}{\partial \hat{z}} - \frac{U}{\rho G^{1/2}}\mathrm{PRC}, \tag{3.5.2}$$

$$\mathrm{R}U = \frac{m_1}{m_2} f_3 V - V\left(v\frac{m_1^2}{m_2^2}\frac{\partial m_2}{\partial \hat{x}} - u\frac{\partial m_1}{\partial \hat{y}}\right) + \mathrm{DIF}.U, \tag{3.5.3}$$

$$\frac{\partial V}{\partial t} + \frac{m_1}{m_2}\left(\frac{\partial P}{\partial \hat{y}} + \frac{\partial G^{23} P}{\partial \hat{z}}\right) = -\mathrm{ADV}V + \mathrm{R}V, \tag{3.5.4}$$

$$\mathrm{ADV}V = m_2\left(\frac{\partial Uv}{\partial \hat{x}} + \frac{\partial Vv}{\partial \hat{y}}\right) + \frac{m_3}{m_v}\frac{\partial \hat{W}v}{\partial \hat{z}} - \frac{V}{\rho G^{1/2}}\mathrm{PRC}, \tag{3.5.5}$$

$$\mathrm{R}V = -\frac{m_2}{m_1} f_3 U - U\left(u\frac{m_2^2}{m_1^2}\frac{\partial m_1}{\partial \hat{y}} - v\frac{\partial m_2}{\partial \hat{x}}\right) + \mathrm{DIF}.V, \tag{3.5.6}$$

$$\frac{\partial W}{\partial t} + \frac{1}{m_3}\frac{\partial}{\partial \hat{z}}\left(\frac{P}{G^{1/2}}\right) + \sigma\frac{gP}{m_3 C_m^2} = \frac{1}{m_3}\mathrm{BUOY} - \mathrm{ADV}W + \mathrm{R}W, \tag{3.5.7}$$

$$\mathrm{BUOY} = \sigma\frac{\rho G^{1/2}\theta'_m}{\theta_m}g - (1-\sigma)\rho' G^{1/2} g, \tag{3.5.8}$$

$$\mathrm{ADV}W = \frac{m_1 m_2}{m_3}\left(\frac{\partial Uw}{\partial \hat{x}} + \frac{\partial Vw}{\partial \hat{y}}\right) + \frac{\partial \hat{W}w}{\partial \hat{z}} - \frac{W}{\rho G^{1/2}}\mathrm{PRC}, \tag{3.5.9}$$

$$\mathrm{R}W = \mathrm{DIF}.W, \tag{3.5.10}$$

where

$$U = \frac{\rho G^{1/2}}{m_2}u, \quad V = \frac{\rho G^{1/2}}{m_1}v, \quad W = \frac{\rho G^{1/2}}{m_3}w, \tag{3.5.11}$$

$$\hat{w} = \frac{1}{G^{1/2}}\left(m_1 G^{1/2} G^{13} u + m_2 G^{1/2} G^{23} v + w\right), \tag{3.5.12}$$

$$\hat{W} = \frac{\rho G^{1/2}}{m_3}\hat{w} = \frac{1}{G^{1/2}}\left\{\frac{m_1 m_2}{m_3}\left(G^{1/2} G^{13} U + G^{1/2} G^{23} V\right) + W\right\}, \tag{3.5.13}$$

$$P = p' G^{1/2}. \tag{3.5.14}$$

Here, u, v and w are the velocity components, m_1 and m_2 are the map factors, m_3 is not a map factor in the z direction but a variable introduced for definition of momentum. ADVs denote the advection terms and DIF.s denote the diffusion terms. Symbols p', ρ and g are the pressure perturbation from the hydrostatic state, density and gravity acceleration, respectively. $G^{1/2}$, G^{13} and G^{23} are the metric tensors, f is the Coriolis parameter. A symbol σ is the switching parameter to choose the way to calculate the buoyancy term. In the MSM, σ is set to zero and buoyancy term is calculated directly from the perturbation of density. A symbol θ_m is the mass-virtual potential temperature (Saito 1997) defined as

$$\theta_m \equiv \theta(1 + 0.608 q_v)(1 - q_c - q_i - q_r - q_s - q_g), \tag{3.5.15}$$

where q is the mixing ratios of water substances and subscripts v, c, i, r, s and g represent water vapor, cloud water, cloud ice, rain, snow and graupel, respectively. A symbol θ'_m is the perturbation of θ_m from 300K. $\hat{W}$ and $\hat{w}$ are vertical momentum and vertical velocity along with $\hat{z}$ coordinate defined below Eq. (3.5.21).

In this model, density is defined by the sum of the masses of moist air and water substances per unit volume as

$$\begin{aligned}\rho &\equiv \rho_d + \rho_v + \rho_c + \rho_i + \rho_r + \rho_s + \rho_g \\ &= \rho_a + \rho_c + \rho_i + \rho_r + \rho_s + \rho_g,\end{aligned} \tag{3.5.16}$$

where ρ_a is the density of air.

PRC is the sum of fallout of precipitable water substances defined by

$$\mathrm{PRC} = \frac{\partial}{\partial \hat{z}}\left(\rho_a V_r q_r + \rho_a V_i q_i + \rho_a V_s q_s + \rho_a V_g q_g\right), \tag{3.5.17}$$

where V_r, V_i, V_s, V_g are the terminal fall velocities of rain, cloud ice, snow and graupel, respectively.

The Lambert conformal projection is employed and the map factors m_1 and m_2, and a variable m_3 are given by

$$m_1 = m_2 = m = \left(\frac{\cos\varphi}{\cos\varphi_1}\right)^{c-1}\left(\frac{1+\sin\varphi_1}{1+\sin\varphi}\right)^{c}, \tag{3.5.18}$$

$$m_3 = 1, \tag{3.5.19}$$

where φ is the latitude of a concerned point, $\varphi_1 = 30°$, $\varphi_2 = 60°$ and c is given by

$$c = \ln\left(\frac{\cos\varphi_1}{\cos\varphi_2}\right)\Bigg/\ln\left\{\frac{\tan\left(45° - \frac{\varphi_1}{2}\right)}{\tan\left(45° - \frac{\varphi_2}{2}\right)}\right\}. \tag{3.5.20}$$

The hybrid terrain-following vertical coordinate which is based on the same approach as the η coordinate (Simmons and Burridge 1981) is adopted to reduce influences of topography as the height increases (Ishida 2007). The vertical coordinate $\hat{z}$ is transformed using the following equation:

$$z = \hat{z} + z_s f(\hat{z}), \tag{3.5.21}$$

where z is the actual height and z_s is the surface height. The function $f(\hat{z})$ is given by,

$$f(\hat{z}) = \frac{c\left\{1 - \left(\frac{\hat{z}}{z_T}\right)^n\right\}}{c + \left(\frac{\hat{z}}{z_T}\right)^n}, \quad c = \frac{\left(\frac{z_l + z_h}{2z_T}\right)^n}{1 - 2\left(\frac{z_l + z_h}{2z_T}\right)^n}, \tag{3.5.22}$$

where z_T is the model top height, $z_l = 1000$, $z_h = 11000$ and $n = 3$ in the MSM. The metric tensors $G^{1/2}$, $G^{1/2}G^{13}$, $G^{1/2}G^{23}$ are written as

$$G^{1/2} = \frac{\partial z}{\partial \hat{z}} = 1 + z_s \frac{-nc(1+c)\left(\frac{\hat{z}}{z_T}\right)^{n-1}}{z_T\left\{c + \left(\frac{\hat{z}}{z_T}\right)^n\right\}^2}, \tag{3.5.23}$$

$$G^{1/2}G^{13} = \frac{\partial z}{\partial \hat{z}}\frac{\partial \hat{z}}{\partial x} = -\frac{\partial z}{\partial \hat{x}} = -\frac{c\left\{1 - \left(\frac{\hat{z}}{z_T}\right)^n\right\}}{c + \left(\frac{\hat{z}}{z_T}\right)^n}\frac{\partial z_s}{\partial \hat{x}}, \tag{3.5.24}$$

$$G^{1/2}G^{23} = \frac{\partial z}{\partial \hat{z}}\frac{\partial \hat{z}}{\partial y} = -\frac{\partial z}{\partial \hat{y}} = -\frac{c\left\{1 - \left(\frac{\hat{z}}{z_T}\right)^n\right\}}{c + \left(\frac{\hat{z}}{z_T}\right)^n}\frac{\partial z_s}{\partial \hat{y}}. \tag{3.5.25}$$

2. Prognostic equation of pressure

The pressure equation is described as follows:

$$\frac{\partial P}{\partial t} + C_m^2(\mathrm{DIVT} - \mathrm{PRC} - \mathrm{PFT}) = 0, \tag{3.5.26}$$

$$\mathrm{DIVT} = m_1 m_2\left(\frac{\partial U}{\partial \hat{x}} + \frac{\partial V}{\partial \hat{y}}\right) + m_3\frac{\partial \hat{W}}{\partial \hat{z}}, \tag{3.5.27}$$

$$\mathrm{PFT} = \frac{\rho G^{1/2}}{\theta_m}\frac{\partial \theta_m}{\partial t}. \tag{3.5.28}$$

Here, C_m is the velocity of sound waves defined by

$$C_m^2 = \frac{C_p}{C_v} R\theta_m \left(\frac{p}{p_0}\right)^{\frac{R}{C_p}}. \tag{3.5.29}$$

C_p and C_v are the specific heat of dry air at constant pressure and constant volume, respectively. R is the gas constant for dry air and $p_0 = 1000$ hPa is a reference pressure. DIVT and PFT are the divergence in $\hat{z}$ coordinate and the thermal expansion of air, respectively.

3. Prognostic equation of potential temperature

   The thermodynamic equation is given by,

$$\frac{\partial \theta}{\partial t} = -\mathrm{ADV}\theta + \frac{Q}{C_p \pi} + \mathrm{DIF}.\theta, \tag{3.5.30}$$

$$\mathrm{ADV}\theta = \frac{1}{\rho G^{1/2}}\left\{ m_1 m_2 \left(\frac{\partial U\theta}{\partial \hat{x}} + \frac{\partial V\theta}{\partial \hat{y}}\right) + m_3 \frac{\partial \hat{W}\theta}{\partial \hat{z}} - \theta \mathrm{DIVT}\right\}, \tag{3.5.31}$$

   where Q is the diabatic heating. π is the Exner function defined by

$$\pi = \left(\frac{p}{p_0}\right)^{\frac{R}{C_p}}. \tag{3.5.32}$$

4. Prognostic equation of water substances

   The prognostic equations of mixing ratios of water substances are given by,

$$\frac{\partial q_n}{\partial t} = -\mathrm{ADV}q_n + Q_n + \mathrm{DIF}.q_n, \tag{3.5.33}$$

$$\mathrm{ADV}q_n = \frac{1}{\rho G^{1/2}}\left\{ m_1 m_2 \left(\frac{\partial U q_n}{\partial \hat{x}} + \frac{\partial V q_n}{\partial \hat{y}}\right) + m_3 \frac{\partial \hat{W} q_n}{\partial \hat{z}} - q_n \mathrm{DIVT}\right\}. \tag{3.5.34}$$

5. State equation

   The state equation is

$$\rho = \frac{p_0}{R\theta_m}\left(\frac{p}{p_0}\right)^{\frac{C_v}{C_p}}. \tag{3.5.35}$$

3.5.3.2 Finite Discretization

The grid structures of the model are the Arakawa C type in the horizontal direction and the Lorenz type in the vertical direction. The fourth-order finite difference scheme is employed to calculate horizontal advection terms, while vertical advection is calculated with the second-order scheme. Considering the staggered grid structure, the fourth-order finite difference is described by

$$\left.\frac{\partial \phi}{\partial x}\right|_i = \frac{9}{8}\frac{\phi_{i+1/2} - \phi_{i-1/2}}{\Delta x} - \frac{1}{8}\frac{\phi_{i+1+1/2} - \phi_{i-1-1/2}}{3\Delta x} + \frac{3}{640}(\Delta x)^4 \frac{\partial^5 \phi}{\partial x^5} + O\left[(\Delta x)^6\right]. \tag{3.5.36}$$

For advection of scalar prognostic variables, the fourth-order finite difference in the flux form is given by

$$\left.\frac{\partial U\theta}{\partial x}\right|_i = \frac{9}{8}\frac{(U\bar{\theta})_{i+1/2} - (U\bar{\theta})_{i-1/2}}{\Delta x} - \frac{1}{8}\frac{(U\bar{\theta})_{i+1+1/2} - (U\bar{\theta})_{i-1-1/2}}{3\Delta x}, \tag{3.5.37}$$

where the second-order interpolation process is used to calculate scalar prognostic variables at the vector points currently. For advection of vector variables,

$$\left.\frac{\partial Uu}{\partial x}\right|_{i+1/2} = \frac{9}{8}\frac{(U\bar{u})_{i+1} - (U\bar{u})_i}{\Delta x} - \frac{1}{8}\frac{(U\bar{u})_{i+2} - (U\bar{u})_{i-1}}{3\Delta x}. \tag{3.5.38}$$

The above higher-order schemes are employed with the modified centered difference advection scheme (Kato 1998), which is a kind of flux limiter and acts as a flux correction scheme.

3.5.3.3 Split Explicit (HE-VI) Scheme

For the temporal discritization, the horizontally explicit, and vertically implicit (HE-VI) scheme is employed. Forward time integrations

$$\frac{U^{\tau+\Delta\tau} - U^\tau}{\Delta\tau} + \frac{m_1}{m_2}\left(\frac{\partial P^\tau}{\partial\hat{x}} + \frac{\partial G^{13}P^\tau}{\partial\hat{z}}\right) = -\mathrm{ADV}U + \mathrm{R}U, \tag{3.5.39}$$

$$\frac{V^{\tau+\Delta\tau} - V^\tau}{\Delta\tau} + \frac{m_2}{m_1}\left(\frac{\partial P^\tau}{\partial\hat{y}} + \frac{\partial G^{23}P^\tau}{\partial\hat{z}}\right) = -\mathrm{ADV}V + \mathrm{R}V, \tag{3.5.40}$$

are used for horizontal momentum equations, where $\Delta\tau$ is the short time step. Backward time integration is employed for vertical momentum equation as

$$\frac{\hat{W}^{\tau+\Delta\tau} - \hat{W}^\tau}{\Delta\tau} + \frac{1}{m_3}\frac{\partial}{\partial\hat{z}}\left(\frac{P^\beta}{G^{1/2}}\right) + \frac{gP^\beta}{m_3C_m^2} = \frac{1}{m_3}\mathrm{BUOY} - \mathrm{ADV}W + \mathrm{R}W + (1-\sigma)\frac{gP^\tau}{m_3C_m^2}, \tag{3.5.41}$$

where

$$P^\beta = \frac{1+\beta}{2}P^{\tau+\Delta\tau} + \frac{1-\beta}{2}P^\tau. \tag{3.5.42}$$

The pressure equation is integrated backward as

$$\frac{P^{\tau+\Delta\tau} - P^\tau}{\Delta\tau} + C_m^2\left\{m_1m_2\left(\frac{\partial U^\gamma}{\partial\hat{x}} + \frac{\partial V^\gamma}{\partial\hat{y}}\right) + m_3\frac{\partial\hat{W}^\beta}{\partial\hat{z}} - \mathrm{PRC} - \mathrm{PFT}\right\} = \mathrm{DIF}.P, \tag{3.5.43}$$

where

$$U^\gamma = \frac{1+\gamma}{2}U^{\tau+\Delta\tau} + \frac{1-\gamma}{2}U^\tau, \quad V^\gamma = \frac{1+\gamma}{2}V^{\tau+\Delta\tau} + \frac{1-\gamma}{2}V^\tau, \quad \hat{W}^\beta = \frac{1+\beta}{2}\hat{W}^{\tau+\Delta\tau} + \frac{1-\beta}{2}\hat{W}^\tau. \tag{3.5.44}$$

Here, β and γ are the implicit factor. $\beta = 1$ and $\gamma = 1$ are employed in the MSM.

Eliminating $\hat{W}^\beta$ from the pressure Eq. (3.5.43) using the vertical momentum Eq. (3.5.41), we obtain the one dimensional Helmholtz type equation

$$-\left(\frac{C_m\Delta\tau(1+\beta)}{2}\right)^2\frac{\partial}{\partial\hat{z}}\left(\frac{1}{G^{1/2}}\frac{\partial}{\partial\hat{z}}\left(\frac{P^\beta}{G^{1/2}}\right)\right) - \left(\frac{C_m\Delta\tau(1+\beta)}{2}\right)^2\frac{\partial}{\partial\hat{z}}\left(\frac{gP^\beta}{C_m^2G^{1/2}}\right) + P^\beta$$
$$= \mathrm{FP.HE.INV} + \mathrm{HP.HE.VAR}, \tag{3.5.45}$$

where

$$\mathrm{FP.HE.INV} = C_m^2 \frac{\Delta\tau(1+\beta)}{2}\left(\mathrm{PRC}^t + \mathrm{PFT}^t + \frac{\mathrm{DIF}.P^t}{C_m^2}\right)$$
$$- C_m^2\left(\frac{\Delta\tau(1+\beta)}{2}\right)^2 m_3 \frac{\partial}{\partial\hat{z}}\left\{\frac{1}{G^{1/2}}\left(\frac{1}{m_3}\mathrm{BUOY}^t - (\mathrm{ADV}W^t - \mathrm{R}W^t) + (1-\sigma)\frac{gP^t}{m_3 C_m^2}\right)\right\}, \quad (3.5.46)$$

$$\mathrm{FP.HE.VAR} = P^\tau - C_m^2 \frac{\Delta\tau(1+\beta)}{2}\left\{m_1 m_2\left(\frac{\partial U^\gamma}{\partial\hat{x}} + \frac{\partial V^\gamma}{\partial\hat{y}} + \frac{\partial}{\partial\hat{z}}(G^{13}U^\beta + G^{23}V^\beta)\right) + m_3\frac{\partial}{\partial\hat{z}}\frac{W^\tau}{G^{1/2}}\right\}. \quad (3.5.47)$$

Considering $(\hat{W}^{\tau+\Delta\tau} - \hat{W}^\tau)/\Delta\tau = 0$ at the upper and lower boundary, upper and lower boundary conditions are given by

$$\frac{1}{G^{1/2}}\frac{\partial}{\partial\hat{z}}\left(\frac{P^\beta}{G^{1/2}}\right) + \frac{gP^\beta}{C_m^2 G^{1/2}} = \frac{m_3}{G^{1/2}}\left\{\frac{1}{m_3}\mathrm{BUOY}^t - \mathrm{ADV}W^t + \mathrm{R}W^t + (1-\sigma)\frac{gP^t}{m_3 C_m^2}\right\}. \quad (3.5.48)$$

3.5.3.4 Divergence Damping

An acoustic filter which is based on the idea of Skamarock and Klemp (1992) is implemented to avoid the computational instability by the sound waves. The gradient of the divergence is added to the momentum equations as

$$\mathrm{R}U \rightarrow \mathrm{R}U + \alpha_H \frac{m_1}{m_2}\left(\frac{\partial G^{1/2}\mathrm{DIVT}}{\partial\hat{x}} + \frac{\partial G^{1/2}G^{13}\mathrm{DIVT}}{\partial\hat{z}}\right), \quad (3.5.49)$$

$$\mathrm{R}V \rightarrow \mathrm{R}V + \alpha_H \frac{m_2}{m_1}\left(\frac{\partial G^{1/2}\mathrm{DIVT}}{\partial\hat{y}} + \frac{\partial G^{1/2}G^{23}\mathrm{DIVT}}{\partial\hat{z}}\right), \quad (3.5.50)$$

$$\mathrm{R}W \rightarrow \mathrm{R}W + \alpha_V \frac{1}{m_3}\frac{\partial}{\partial\hat{z}}\frac{\mathrm{DIVT}}{G^{1/2}}, \quad (3.5.51)$$

where

$$\alpha_H = 0.06\,\frac{1}{\Delta t}\min\left[\left(\frac{\Delta x}{m_1}\right)^2, \left(\frac{\Delta y}{m_2}\right)^2\right], \quad (3.5.52)$$

$$\alpha_V = 0.05\frac{1}{\Delta t}\left(G^{1/2}\Delta\hat{z}\right)^2. \quad (3.5.53)$$

3.5.3.5 Time Splitting of Advection and Gravity Waves

To stabilize the integration in cases where environmental wind is considerably strong and strong inversion layer exists, a new time splitting scheme is implemented (Saito *et al.* 2006). In the scheme, the higher-order advection terms with the modified advection scheme are evaluated at the center of the leapfrog time step, and then the lower-order (second-order) components at each short time step are adjusted only in the latter half of the leapfrog time integration scheme,

$$\mathrm{ADV}^* = \mathrm{ADV} - \mathrm{ADVL} + \mathrm{ADVL}^\tau. \quad (3.5.54)$$

Here, ADV and ADVL are the higher-order advection and the lower-order advection component at a leapfrog time step, respectively, while ADVL^τ is the lower-order advection components at each short time step. This adjustment is performed from $(ns-1)/2+1$ to $ns-1$, where ns is the ratio of $2\Delta t$ and $\Delta\tau$ as shown Figure 3.5.1.

Using this adjustment, the equation of $\hat{W}$ is rewritten as

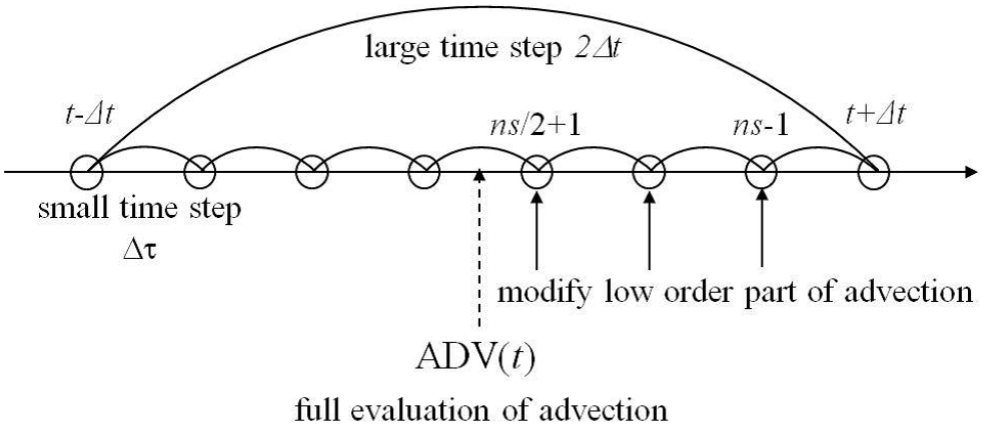

Figure 3.5.1: Time split of advection for case of $ns = 2\Delta t/\Delta\tau = 7$ after Saito *et al.* (2006) Fig. 3.

$$\frac{\hat{W}^{\tau+\Delta\tau} - \hat{W}^{\tau}}{\Delta\tau} + \frac{1}{m_3}\frac{\partial}{\partial\hat{z}}\left(\frac{P^{\beta}}{G^{1/2}}\right) + \frac{gP^{\beta}}{m_3 C_m^2}$$
$$= \frac{1}{m_3}\mathrm{BUOY} - (\mathrm{ADV}W - \mathrm{ADVL}W + \mathrm{ADVL}W^{\tau}) + \mathrm{R}W + (1-\sigma)\frac{gP^{\tau}}{m_3 C_m^2}. \tag{3.5.55}$$

The time splitting of advection of potential temperature using this adjustment is an alternative way to split gravity waves

$$\frac{\theta^{\tau+\Delta\tau} - \theta^{\tau}}{\Delta\tau} = -(\mathrm{ADV}\theta - \mathrm{ADVL}\theta + \mathrm{ADVL}\theta^{\tau}) + \frac{Q}{C_p\pi} + \mathrm{DIF}.\theta, \tag{3.5.56}$$

where ADVLθ is computed by a flux form second-order central difference.

3.5.3.6 Computational Diffusion

A nonlinear damper, a fourth-order linear damper and the Asselin time filter (Robert 1966) are employed to suppress the computational noise. The targeted moisture diffusion is implemented (Saito and Ishida 2005) to control the gridpoint storms and the associated intense grid scale precipitation.

1. Nonlinear damper

   Nonlinear damping (Nakamura 1978),

   $$\mathrm{D}_{NL} = \frac{1}{8m_{NL}\Delta t}\left\{(\Delta x)^3\frac{\partial}{\partial x}\left(\left|\frac{\partial\phi}{\partial x}\right|\frac{\partial\phi}{\partial x}\right) + (\Delta y)^3\frac{\partial}{\partial y}\left(\left|\frac{\partial\phi}{\partial y}\right|\frac{\partial\phi}{\partial y}\right)\right\} \tag{3.5.57}$$

   is added to the diffusion term of ϕ where $m_{NL} = 600$ is used. For two-grid noise of amplitude α, 1/e-folding time is given by $m_{NL}\Delta t/\alpha$. This nonlinear damping sometimes causes the computational instability because of the excessive diffusion. A limit is applied to D_{NL} using the estimated amplitude of the maximum wave number.

2. Fourth-order linear damper

   Fourth-order linear damping,

$$\mathrm{D}_{2D} = \frac{1}{16 m_{2D} \Delta t} \left\{ (\Delta x)^4 \frac{\partial^4 \phi}{\partial x^4} + (\Delta y)^4 \frac{\partial^4 \phi}{\partial y^4} \right\} \tag{3.5.58}$$

is added to the diffusion term of ϕ where $m_{2D} = 600$ is used. 1/e-folding time is given by $m_{2D}\Delta t$.

3. Asselin time filter

   After the time integration, all quantities of prognostic variables are modified following the Asselin time filter,

$$\phi(t) = \phi(t) + 0.5\nu \{\phi(t - \Delta t) - 2\phi(t) + \phi(t + \Delta t)\}, \tag{3.5.59}$$

   where ν is set to 0.2 in the MSM.

4. Targeted moisture diffusion

   A second-order horizontal diffusion is applied to water vapor when strong upward motions exist to selectively damp the gridpoint storms caused by the positive feedback of the latent heat release by condensation and updraft acceleration. In the MSM, water vapor at grid points where the upward velocity exceeds 3.0 ms^{-1} is horizontal diffused with 1/e-folding time of 300 seconds.

3.5.3.7 Boundary Conditions

Rayleigh damping,

$$\mathrm{D}_R = -\frac{\mathrm{D}}{m_R} \{\phi - \phi_{EXT}\} \tag{3.5.60}$$

is added near the lateral and upper boundary to the time tendencies of horizontal and vertical momentum, potential temperature and mixing ratio of water vapor, where ϕ is the prognostic variable and ϕ_{EXT} is the value of the external model. m_R is the coefficient which determines the 1/e-folding time and $m_R = 2400$ is used. D is a function given by of location, where D is unity at boundary and decreases as the grid points are away from boundary.

3.5.4 Cloud Microphysics

An explicit three-ice bulk microphysics scheme (Ikawa and Saito 1991) based on Lin *et al.* (1983) is incorporated. The scheme predicts the mixing ratios of water vapor and five hydrometeors, which are designated by q_x where x denotes categories, defined as v for water vapor, c for cloud water, r for rain, i for cloud ice, s for snow, and g for graupel. Number concentrations of solid hydrometeors (cloud ice N_i, snow N_s, and graupel N_g) are optionally treated as prognostic values in addition to their mixing ratios. Spherical particles are assumed in all categories of hydrometeors. Density is constant in each category (ρ_x). Therefore, the mass-size relation ($m_x(D_x)$) is given by

$$m_x(D_x) = \frac{\pi}{6} \rho_x {D_x}^3, \tag{3.5.61}$$

where D_x is the diameter of the particles. Simple power law is also taken for the fall velocity-size relation ($U_x(D_x)$); therefore, it is given by

$$U_x(D_x) = \alpha_{ux} {D_x}^{\beta_{ux}} \left(\frac{\rho_0}{\rho_a} \right)^{\gamma_{ux}}, \tag{3.5.62}$$

where ρ_a is the density of the air, ρ_0 is the density of the reference air, and α_{ux}, β_{ux} and γ_{ux} are constants in each category of the hydrometeors.

The cloud microphysical processes simulated in this scheme are illustrated in Figure 3.5.2 (see Table 3.5.1 for the list of the symbols used in Figure 3.5.2). In this scheme, some basic cloud microphysical processes (e.g., nucleation of cloud particles, conversion from cloud particles to precipitation particles) are parameterized, because their processes occur in a shorter temporal compared to the integration time-step. However, most

of the cloud microphysical processes can be applied directly to the calculation related to the size distribution assumed in each category of hydrometeors. The number-weighted mean of temporal tendency of one cloud microphysical variable ϕ due to one cloud microphysical process in each particle gives the grid-mean temporal tendency of ϕ as follows:

$$\frac{d\phi}{dt} = \int_0^\infty \frac{d\phi_0}{dt} n(D)\, dD, \tag{3.5.63}$$

where $\frac{d\phi_0(D)}{dt}$ is temporal tendency of ϕ due to one cloud microphysical process in a particle of diameter D, and $n(D)\, dD$ is the number of particles per unit volume of air with diameter D to $D + dD$. Therefore, size distributions of hydrometeors deeply affect time tendency of cloud microphysical variables due to cloud microphysical processes.

The size distributions of rain, snow and graupel are assumed to follow an exponential function:

$$n_x(D_x) = N_{0x} \exp(-\lambda_x D_x), \tag{3.5.64}$$

where N_{0x} is the intercept, and λ_x is the slope parameter of the size distribution. Therefore, the moment formula for rain, snow, and graupel is calculated as the following equation:

$$M_x(p) = \int_0^\infty {D_x}^p n_x(D_x)\, dD_x = N_{0x} \frac{\Gamma(1+p)}{{\lambda_x}^{1+p}}, \tag{3.5.65}$$

where $M_x(p)$ is the p-th moment of $n_x(D_x)$. The number concentration is the zeroth moment of $n_x(D_x)$; therefore, it is calculated as

$$N_x = \int_0^\infty n_x(D_x)\, dD_x = M_x(0) = \frac{N_{0x}}{\lambda_x}. \tag{3.5.66}$$

The mixing ratio ($q_x \equiv \rho_x/\rho_a$) is the third moment of $n_x(D_x)$; therefore, it is also calculated as

$$q_x = \frac{1}{\rho_a} \int_0^\infty m_x(D_x) n_x(D_x)\, dD_x = \frac{\rho_x}{\rho_a} \frac{\pi}{6} M_x(3) = \frac{\rho_x}{\rho_a} \frac{\pi}{6} N_{0x} \frac{\Gamma(4)}{{\lambda_x}^4}. \tag{3.5.67}$$

When the number concentrations for rain, snow, and graupel are not predicted, their intercepts are assumed to be constant; therefore, the following formula is used:

$$N_{0x} = \text{const.}, \quad \lambda_x = \left(\frac{\pi \rho_x N_{0x}}{\rho_a q_x} \right)^{\frac{1}{4}}. \tag{3.5.68}$$

This option is adopted in the MSM.

Cloud water and cloud ice are assumed to be monodisperse; therefore, their size distributions follow the δ-function:

$$n_x(D_x) = N_x \delta(D_x - \overline{D_x}), \tag{3.5.69}$$

where $\delta(x)$ satisfies the following equation: $\int_{-\infty}^{\infty} \delta(x-a) f(x)\, dx = f(a)$, and $\overline{D_x}$ is the diameter of the monodisperse particle. The moment formula for cloud water and cloud ice is given by

$$M_x(p) = N_x \overline{D_x}^p. \tag{3.5.70}$$

The mixing ratio is calculated as

$$q_x = \frac{\rho_x}{\rho_a} \frac{\pi}{6} M_x(3) = \frac{\rho_x}{\rho_a} \frac{\pi}{6} N_x \overline{D_x}^3. \tag{3.5.71}$$

Therefore, their diameter is determined as

$$\overline{D_x} = \left(\frac{6 \rho_a q_x}{\pi \rho_x N_x} \right)^{\frac{1}{3}}. \tag{3.5.72}$$

The number concentration of cloud water (N_c) is always assumed to be constant in this scheme. The number concentration of cloud ice (N_i) can be optionally treated as prognostic value, and this option is adopted in the MSM.

Table 3.5.2 provides the characteristics of each hydrometeor class. More detailed information on the treatment of each cloud microphysical process in this scheme can be found in Ikawa and Saito (1991).

Table 3.5.1: List of symbols in Figure 3.5.2

Notation	Description
	Production terms
p_a_ppp_b	Production of category "a" converted from category "b" through a process "ppp"
p_a_ppp_a_b	Growth of category "a" by capturing category "b" through a process "ppp"
p_a_ppp_b_c	Generation of category "a" by category "b" capturing category "c" through a process "ppp"
	Categories by hydrometeors
v	Water vapor
w	Cloud water
r	Rain
i	Cloud ice
s	Snow
g	Graupel
	Cloud microphysical processes
evp	Evaporation
cnd	Condensation
aut, cn	Conversion
ac	Accretion
mlt	Melting
nud	Nucleation
dep	Deposition/Sublimation
frz	Freezing
spl	Ice splinter multiplication
sed	Sedimentation

Table 3.5.2: Assumed hydrometeor parameters and characteristics.

Variable	Rain q_r(kg kg^{-1})	Snow q_s(kg kg^{-1}) N_s (m^{-3})	Graupel q_g(kg kg^{-1}) N_g (m^{-3})	Cloud water q_c(kg kg^{-1})	Cloud ice q_i(kg kg^{-1}) N_i (m^{-3})
Size distribution (m^{-4})	$n_r(D_r) = N_{r0}\exp(-\lambda_r D_r)$ $N_{r0} = 8.0\times10^6$	$n_s(D_s) = N_{s0}\exp(-\lambda_s D_s)$	$n_g(D_g) = N_{g0}\exp(-\lambda_g D_g)$	$\overline{D_c} = \left[\frac{6q_c\rho_a}{\pi N_c\rho_c}\right]^{\frac{1}{3}}$ $N_c = 1.0\times10^8$	$\overline{D_i} = \left[\frac{6q_i\rho_a}{\pi N_i\rho_i}\right]^{\frac{1}{3}}$
Fall velocity (m s^{-1})	$U_x(D_x) = \alpha_{ux} D_x^{\beta_{ux}} \left(\frac{\rho_0}{\rho_a}\right)^{\gamma_{ux}}$				
	$\alpha_{ur} = 842$ $\beta_{ur} = 0.8$ $\gamma_{ur} = 0.5$	$\alpha_{us} = 17$ $\beta_{us} = 0.5$ $\gamma_{us} = 0.5$	$\alpha_{ug} = 124$ $\beta_{ug} = 0.64$ $\gamma_{ug} = 0.5$	$\alpha_{uc} = 2.98\times10^7$ $\beta_{uc} = 2.0$ $\gamma_{uc} = 1.0$	$\alpha_{ui} = 700$ $\beta_{ui} = 1.0$ $\gamma_{ui} = 0.35$
Density (kg m^{-3})	$\rho_r = 1.0\times10^3$	$\rho_s = 8.4\times10^1$	$\rho_g = 3.0\times10^2$	$\rho_c = 1.0\times10^3$	$\rho_i = 1.5\times10^2$

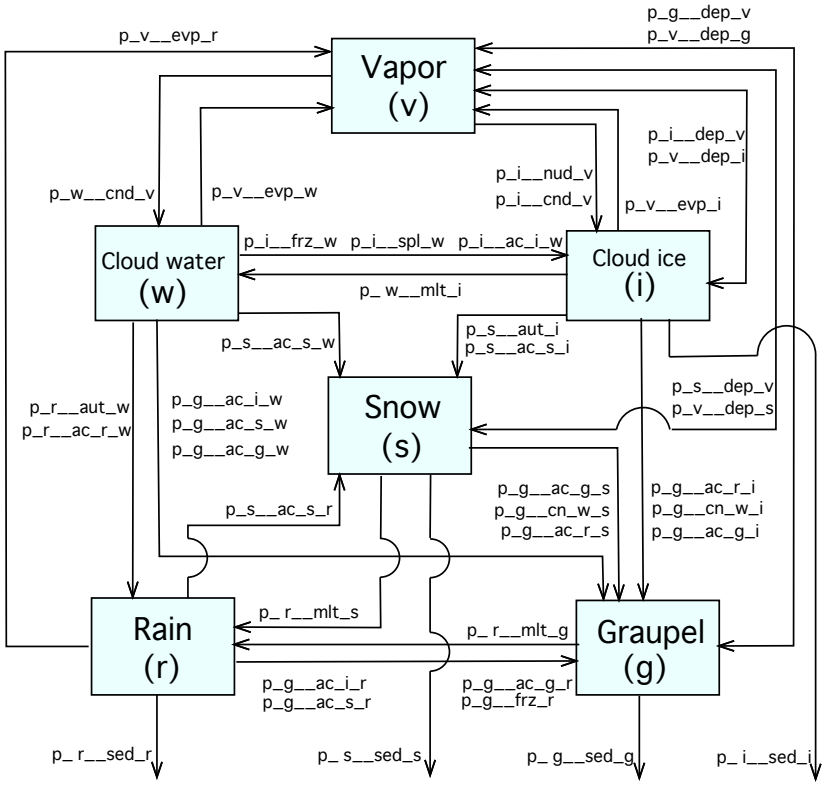

Figure 3.5.2: Cloud microphysical processes in the MSM. For a list of symbols, see Table 3.5.1.

3.5.5 Convective Parameterization

In order to incorporate vertical transport of heat and moisture by subgrid-scale convection, the Kain-Fritsch (KF) convective parameterization (Kain and Fritsch 1990; Kain 2004) has been employed for the MSM.

The KF scheme parameterizes convection using a cloud model based on the one-dimensional entraining/detraining plume model which contains detailed treatment concerning interactions between convective updraft and surrounding air, which are entrainment and detrainment processes. Therefore the subgrid-scale convection parameterized by the KF scheme is sensitive to thermodynamic conditions of the environment. The cloud model consists of a pair of upward and downward mass fluxes. These fluxes and compensating subsidence, which is induced through the mass conservation, transport heat and moisture vertically. Entrainment and detrainment, through which the mass is exchanged between the cumulus and the environment, control the development of the mass fluxes.

The scheme starts from estimation of mass fluxes representing the convection. In that estimation, entrainment and detrainment are calculated as interaction with the environment. The vertical transport of heat and moisture by the fluxes and the compensating subsidence brings modified vertical profiles of temperature and water vapor. Adjusting the mass fluxes to reduce the convective available potential energy (CAPE) results in vertically stabilized atmosphere. To find out grids at which the scheme works, a trigger function is used. As a consequence, temporal tendencies of temperature, water vapor and hydrometeors are obtained by the scheme. Each process is described below in detail.

The upward mass flux is estimated through moving air mass up from the lifting condensation level (LCL) with the conservation of equivalent potential temperature and total amount of water contents in a Lagrangian sense. The initial upward mass flux at the LCL, M_{u0}, is given as follows with the assumption that the vertical velocity is $1\mathrm{ms}^{-1}$ and the initial area occupied by convection is 1% of a grid,

$$M_{u0} = \rho_{u\mathrm{LCL}} \times 0.01\Delta x^2, \tag{3.5.73}$$

where $\rho_{u\mathrm{LCL}}$ is the density of the upward mass flux at the LCL and Δx is the grid size of 5km for the MSM.

While evaluating the updraft, condensate is formed and some of them are glaciated according to the temperature of the updraft at each level, and excess amount of these hydrometeors over a threshold is taken out from the updraft as precipitation via a Kessler type autoconversion scheme. Furthermore, as entrainment and detrainment, the interactions between updraft and the environment as the turbulent mixing are also estimated at each vertical level. It is supposed that the turbulent mixing occurs at very near the periphery of the updraft, then many subparcel-like mixtures of the updraft and the environment are formed at various ratios assuming the Gaussian distribution of the probability such that mixtures at the ratio of fifty-fifty is the most likely. Consequently, the mixtures with positive (negative) buoyancy against the environment entrain into (detrain from) updraft. It means that more moist/warmer condition of the environment favors much developed updraft and that drier/cooler one prevents the updraft from growing. The hydrometeors included in detrainment masses are taken into account as the tendencies for the grid-scale variables. The vertical velocity of the updraft changes by buoyancy and weight of the hydrometeors. The updraft terminates when the upward mass flux has emaciated through detrainment or vertical velocity of the updraft turns into zero.

Entrainment rate, δM_e, which determines amount of entrainment and detrainment, is inversely proportional to radius of the updraft, R,

$$\delta M_e = M_{u0}(0.03\delta P/R), \tag{3.5.74}$$

where δP(Pa) is thickness of vertical grid. The radius of the updraft is used only for the entrainment rate estimation.

The radius R is rendered as a function of larger-scale forcing through the grid-resolved vertical velocity and the height of the LCL (Moriyasu and Narita 2011). In the case that the height of the LCL is lower than 950hPa, R takes 500m. When the height of the LCL is higher than 800hPa, R is determined as follows:

$$R = factor \times \Delta x/\Delta x_0 \times \begin{cases} 1000 & (W_0 < 0\mathrm{ms}^{-1}) \\ 1000(1 + W_0/0.1) & (0\mathrm{ms}^{-1} \leq W_0 \leq 0.1\mathrm{ms}^{-1}) \\ 2000 & (W_0 > 0.1\mathrm{ms}^{-1}), \end{cases} \tag{3.5.75}$$

$$W_0 = \bar{W}_{\mathrm{LCL}} \times \Delta x/\Delta x_0 - W_{\mathrm{KLCL}}, \tag{3.5.76}$$

$$W_{\mathrm{KLCL}} = \begin{cases} 0.02 & (Z_{\mathrm{LCL}} \geq Z_0) \\ 0.02 \times Z_{\mathrm{LCL}}/Z_0 & (Z_{\mathrm{LCL}} < Z_0), \end{cases} \tag{3.5.77}$$

where Δx_0 takes 25km that is the grid size of the original model the KF scheme developed, W_0 indicates the intensity of the updraft depending on the grid-resolved vertical velocity at the LCL, $\bar{W}_{\mathrm{LCL}}$ is a running mean of the grid-resolved vertical velocity at the LCL for 8 timesteps, Z_{LCL} is the height of the LCL, Z_0 takes 2000m and *factor* takes 5 for the MSM. In the case that the height of the LCL is between 950hPa and 800hPa, R is linearly interpolated between both cases above. The gap of the grid size between the MSM and the original model needs the correction term of $\Delta x/\Delta x_0$.

A downward mass flux as a convective downdraft is fueled by evaporation of the hydrometeors that are generated within the updraft. The downdraft starts at the layer of 150hPa above the LCL. With the similar way to the updraft, the mass flux is estimated for the downdraft. Entrainment between the downdraft and the environment is allowed only above the LCL and detrainment only below the LCL.

Parameterized shallow convection is also allowed for any updraft that does not reach the minimum cloud depth for deep convection. The minimum value of cloud depth is a function of temperature at cloud base (LCL).

Adjusting amount of the mass fluxes iteratively in the sense of a 85% reduction of the initial value of CAPE, the stabilized atmosphere succeeds. Differences of the thermodynamic variables of the stabilized atmosphere from that of the initial unstable one is the contributions of the parameterized convection as the goal of the scheme. The differences divided by an advective time period for a column are as the tendencies on each step. In the case of the temperature, T, for example,

$$\left.\frac{dT}{dt}\right|_{\text{convection}} = \frac{T_{\text{stabilized}} - T_{\text{initial}}}{\Delta x/\bar{V}}, \tag{3.5.78}$$

where $\bar{V}$ is an average wind speed at the LCL and 500hPa.

Searching to find out grids which the parameterized convection should occur is repeated in every 5 minutes (*i.e.* 15 timesteps). For picking up the grids, the trigger function is defined as the temperature of a lifted air mass at the LCL with perturbations as a function of the grid-resolved vertical velocity and the relative humidity at the LCL added.

$$\text{Trigger Function} = T_{\text{LCL}} + 0.2 \times \Delta T_{\text{LCL}} + 0.25 \times \Delta T_{\text{RH}}. \tag{3.5.79}$$

The first term of the perturbations represents the dynamical forcing which needs to overcome the convective inhibition.

$$\Delta T_{\text{LCL}} = \max\left[(100W_0)^{\frac{1}{3}}, 0\right]. \tag{3.5.80}$$

And the second term comes from the variance in the relative humidity distribution (Undén *et al.* 2002).

$$\Delta T_{\text{RH}} = \begin{cases} 0 & (RH_{\text{LCL}} < 0.75) \\ 0.25(RH_{\text{LCL}} - 0.75)q/(\partial q^*_{\text{LCL}}/\partial T) & (0.75 \leq RH_{\text{LCL}} \leq 0.95) \\ (1/RH_{\text{LCL}} - 1)q/(\partial q^*_{\text{LCL}}/\partial T) & (0.95 < RH_{\text{LCL}}), \end{cases} \tag{3.5.81}$$

where RH_{LCL} is the grid-resolved relative humidity at the LCL, q is mixing ratio of the water vapor of the lifted source layers and q^*_{LCL} is mixing ratio of the saturated water vapor as grid-resolved value at the LCL. Tuning factors for both the perturbations appear in Eq. (3.5.79) for the MSM.

First, the potential updraft source layer (USL) of the lowest 50hPa depth is lifted adiabatically to its LCL. And then the trigger function to be compared with the environmental temperature represented by a grid-scale value. If $T_{\text{LCL}} + 0.2 \times \Delta T_{\text{LCL}} + 0.25 \times \Delta T_{\text{RH}} > T_{\text{ENV}}$ is met, the USL is regarded to have buoyancy and parameterized convection is initiated at the LCL. If not, the base of the potential USL is moved up 15hPa and the comparison between the trigger function and T_{ENV} is repeated while the base of the potential USL is below the lowest 300hPa of the atmosphere.

3.5.6 Radiation

The radiation process employed in the MSM is almost identical to that in the GSM, as codes of the GSM radiation process was ported into the MSM. The details are described in Subsection 3.2.3. Some differences between them are mentioned below.

A method to evaluate the effective radius of a cloud ice particle in the MSM is based on Ou and Liou (1995) with modification by McFarquhar *et al.* (2003). Following the method, the effective radius $r_{\text{e}}[\mu\text{m}]$ is given as

$$r_{\text{e}} = -1.56 + 0.388D_{\text{e}} + 0.00051{D_{\text{e}}}^2, \tag{3.5.82}$$

$$D_{\text{e}} = 326.3 + 12.42T + 0.197T^2 + 0.0012T^3, \tag{3.5.83}$$

where T [deg. C] is air temperature and D_{e} [μm] is the mean effective size of the particle.

Cloud fraction is diagnosed using the partial condensation method based on Sommeria and Deardorff (1977) which is also employed in evaluating buoyancy flux in the boundary layer scheme (Subsection 3.5.7).

The longwave and shortwave radiation are fully calculated every 15 minutes, while heating rates due to longwave and shortwave radiation are corrected every time step using the surface temperature and the solar zenith angle, respectively.

3.5.7 Boundary Layer

As a boundary layer scheme which represents vertical turbulent transport of momentum, heat and water, the Mellor-Yamada-Nakanishi-Niino Level 3 model (MYNN3) (Nakanishi and Niino 2009) is employed in the MSM.

MYNN3 is the second order turbulent closure model, which assumes that the third order moments of turbulent fluctuation can be depicted by the lower order moments. The full model (called "Level 4") requires too large computational costs because all the second order moments are prognostic variables. In order to reduce the computational costs to run, some terms appeared in the prognostic equations are neglected in terms of the order of anisotropy. In the model called "Level 3" with the boundary layer approximation in which horizontal derivatives are ignored, just only four turbulent prognostic variables, including the turbulent kinetic energy (TKE), are left as

$$\frac{Dq^2}{Dt} = -2\left(\overline{u'w'}\frac{\partial\overline{u}}{\partial z} + \overline{v'w'}\frac{\partial\overline{v}}{\partial z}\right) + 2\frac{g}{\overline{\theta_{\rm v}}}\overline{w'\theta'_{\rm v}} - 2\varepsilon + {\rm dif}.q^2, \tag{3.5.84}$$

$$\frac{D\overline{\theta'^2_{\rm l}}}{Dt} = -2\overline{w'\theta'_{\rm l}}\frac{\partial\overline{\theta_{\rm l}}}{\partial z} - 2\varepsilon_\theta + {\rm dif}.\overline{\theta'^2_{\rm l}}, \tag{3.5.85}$$

$$\frac{D\overline{q'^2_{\rm w}}}{Dt} = -2\overline{w'q'_{\rm w}}\frac{\partial\overline{q_{\rm w}}}{\partial z} - 2\varepsilon_q + {\rm dif}.\overline{q'^2_{\rm w}}, \tag{3.5.86}$$

$$\frac{D\overline{\theta'_{\rm l}q'_{\rm w}}}{Dt} = -\overline{w'\theta'_{\rm l}}\frac{\partial\overline{q_{\rm w}}}{\partial z} - \overline{w'q'_{\rm w}}\frac{\partial\overline{\theta_{\rm l}}}{\partial z} - 2\varepsilon_{\theta q} + {\rm dif}.\overline{\theta'_{\rm l}q'_{\rm w}}, \tag{3.5.87}$$

and the other second order moments are diagnosed as

$$\overline{w'u'} = -q\ell(S_{\rm M2.5} + S'_{\rm M})\frac{\partial\overline{u}}{\partial z}, \tag{3.5.88}$$

$$\overline{w'v'} = -q\ell(S_{\rm M2.5} + S'_{\rm M})\frac{\partial\overline{v}}{\partial z}, \tag{3.5.89}$$

$$\overline{w'\theta'_{\rm l}} = -q\ell(S_{\rm H2.5} + S'_{\rm H})\frac{\partial\overline{\theta_{\rm l}}}{\partial z} = -q\ell\left(S_{\rm H2.5}\frac{\partial\overline{\theta_{\rm l}}}{\partial z} + \Gamma_\theta\right), \tag{3.5.90}$$

$$\overline{w'q'_{\rm w}} = -q\ell(S_{\rm H2.5} + S'_{\rm H})\frac{\partial\overline{q_{\rm w}}}{\partial z} = -q\ell\left(S_{\rm H2.5}\frac{\partial\overline{q_{\rm w}}}{\partial z} + \Gamma_q\right). \tag{3.5.91}$$

Here, $q_{\rm l}$ is mixing ratio of condensed water (including ice phase), and

$$q^2 = 2{\rm TKE} = \left(\overline{u'^2} + \overline{v'^2} + \overline{w'^2}\right), \tag{3.5.92}$$

$$\theta_{\rm l} = \theta - \frac{L}{C_p}\frac{\theta}{T}q_{\rm l}, \tag{3.5.93}$$

$$q_{\rm w} = q_{\rm v} + q_{\rm l}, \tag{3.5.94}$$

with the assumptions that the vertical derivative of the third order moments can reduce to diffusion terms (dif.X denotes a diffusion term on X). The dissipation terms ε_X appeared in the equations are parameterized on the basis of the Kolmogorov's local isotropy assumption as

$$\varepsilon = \frac{q}{B_1\ell}q^2, \quad \varepsilon_\theta = \frac{q}{B_2\ell}\overline{\theta'^2_{\rm l}}, \quad \varepsilon_q = \frac{q}{B_2\ell}\overline{q'^2_{\rm w}}, \quad \varepsilon_{\theta q} = \frac{q}{B_2\ell}\overline{q'_{\rm w}\theta'_{\rm l}}, \tag{3.5.95}$$

with the closure constants B_1, B_2. The mixing length ℓ is given by

$$\frac{1}{\ell} = \frac{1}{L_{\rm S}} + \frac{1}{L_{\rm T}} + \frac{1}{L_{\rm B}}, \tag{3.5.96}$$

where

$$L_{\rm S} = \begin{cases} kz/3.7 & (\zeta \geqq 1) \\ kz(1+2.7\zeta)^{-1} & (0 \leqq \zeta < 1) \\ kz(1-\alpha_4\zeta)^{0.2} & (\zeta < 0) \end{cases}, \tag{3.5.97}$$

$$L_{\mathrm{T}} = \alpha_1 \frac{\int_0^\infty qz\, dz}{\int_0^\infty q\, dz}, \tag{3.5.98}$$

$$L_{\mathrm{B}} = \begin{cases} \alpha_2 q / N_{\mathrm{l}} & (\partial\theta/\partial z > 0, \zeta \geqq 0) \\ \left[\alpha_2 q + \alpha_3 (q_{\mathrm{c}}/L_T N_{\mathrm{l}})^{1/2}\right] / N_{\mathrm{l}} & (\partial\theta/\partial z > 0, \zeta < 0) \\ \infty & (\partial\theta/\partial z < 0) \end{cases}, \tag{3.5.99}$$

with the Brunt-Väisälä frequency N_{l}, von Kármán's constant k, and $\zeta = z/L$ with the Monin-Obukhov length L. Empirical constants α_1, α_2, α_3 and α_4 set to be

$$(\alpha_1, \alpha_2, \alpha_3, \alpha_4) = (0.23, 1.0, 5.0, 100.0). \tag{3.5.100}$$

$S_{\mathrm{M2.5}}$ and $S_{\mathrm{H2.5}}$ are determined by the flux Richardson number and empirical constants appearing in closure assumptions. S'_{M}, S'_{H}, Γ_θ and Γ_q are correction terms induced by the enhancement from level 2.5 (in which only the TKE is treated as a prognostic variable) to level 3. The correction terms depend on the turbulent prognostic variables (q^2, $\overline{\theta_{\mathrm{l}}'^2}$, $\overline{q_{\mathrm{w}}'^2}$ and $\overline{\theta_{\mathrm{l}}' q_{\mathrm{w}}'}$).

Buoyancy flux $(g/\overline{\theta_{\mathrm{v}}})\overline{w'\theta_{\mathrm{v}}'}$ is the important origin of the TKE production. By considering partial condensation effects assuming that fluctuations of θ_{l} and q_{w} from their mean values is depicted by the Gaussian probability density function (PDF) (Sommeria and Deardorff 1977), the width of which depends on $\overline{\theta_{\mathrm{l}}'^2}$, $\overline{q_{\mathrm{w}}'^2}$ and $\overline{\theta_{\mathrm{l}}' q_{\mathrm{w}}'}$, the buoyancy flux can be written as a function of cloud fraction and condensed water obtained as moments of the PDF.

Using local gradient of u, v, θ_{l} and q_{w}, $S_{\mathrm{M2.5}}$ and $S_{\mathrm{H2.5}}$ can be calculated. Once the prognostic equations Eq. (3.5.84), Eq. (3.5.85), Eq. (3.5.86) and Eq. (3.5.87) are integrated, fluxes Eq. (3.5.88), Eq. (3.5.89), Eq. (3.5.90) and Eq. (3.5.91) and tendencies of the turbulent prognostic variables can be calculated. The fluxes give temporal tendency of a variable $\phi(= u, v, \theta_{\mathrm{l}}, q_{\mathrm{w}})$ due to the turbulent transport as follows,

$$\frac{\partial \phi}{\partial t} = -\frac{\partial}{\partial z}\overline{w'\phi'}. \tag{3.5.101}$$

For the details of the formalism, refer to Nakanishi (2001); Nakanishi and Niino (2004, 2006, 2009).

3.5.8 Surface Fluxes

The main procedures around surface processes are evaluation of surface fluxes. It is assumed that the turbulent fluxes are constant with height and equal to the surface values within the surface layer. They can be expressed in term of differences between quantities at the lowest layer of atmosphere (identified by a subscript "a") and surface (identified by a subscript "s") as

$$\overline{u'w'} = -C_{\mathrm{m}} U_{\mathrm{a}} u_{\mathrm{a}}\,, \tag{3.5.102}$$

$$\overline{v'w'} = -C_{\mathrm{m}} U_{\mathrm{a}} v_{\mathrm{a}}\,, \tag{3.5.103}$$

$$\overline{\theta_{\mathrm{v}}'w'} = -C_{\mathrm{h}} U_{\mathrm{a}} (\theta_{\mathrm{va}} - \theta_{\mathrm{vs}})\,, \tag{3.5.104}$$

$$\overline{q_{\mathrm{v}}'w'} = -C_{\mathrm{q}} \beta U_{\mathrm{a}} (q_{\mathrm{va}} - q_{\mathrm{sat}})\,, \tag{3.5.105}$$

where $U_{\mathrm{a}} = \sqrt{u_{\mathrm{a}}^2 + v_{\mathrm{a}}^2}$, q_{sat} is the saturated specific humidity at the ground surface temperature T_1, and β is the evapolation efficiency. Over land, β is estimated with soil moisture

$$\beta = \begin{cases} w_{\mathrm{g}}/0.3 & (w_{\mathrm{g}} \leq 0.3) \\ 1 & (w_{\mathrm{g}} > 0.3) \end{cases}, \tag{3.5.106}$$

where w_{g} is the volumetric water content at the surface, and is predicted by Eq. (3.5.133) (see Subsection 3.5.9). Over the sea, snow, and seaice, β is set equal to 1.

The transfer coefficients C_m, C_h, and C_q can be expressed as

$$C_\mathrm{m} = \frac{\kappa^2}{\left[\ln\frac{z-d_0}{z_{0\mathrm{m}}} - \psi_\mathrm{m}\left(\frac{z-d_0}{L}\right) + \psi_\mathrm{m}\left(\frac{z_{0\mathrm{m}}}{L}\right)\right]^2}, \tag{3.5.107}$$

$$C_\mathrm{h} = \frac{\kappa^2}{\left[\ln\frac{z-d_0}{z_{0\mathrm{m}}} - \psi_\mathrm{m}\left(\frac{z-d_0}{L}\right) + \psi_\mathrm{m}\left(\frac{z_{0\mathrm{m}}}{L}\right)\right]\left[\ln\frac{z-d_0}{z_{0\mathrm{h}}} - \psi_\mathrm{h}\left(\frac{z-d_0}{L}\right) + \psi_\mathrm{h}\left(\frac{z_{0\mathrm{h}}}{L}\right)\right]}, \tag{3.5.108}$$

$$C_\mathrm{q} = \frac{\kappa^2}{\left[\ln\frac{z-d_0}{z_{0\mathrm{m}}} - \psi_\mathrm{m}\left(\frac{z-d_0}{L}\right) + \psi_\mathrm{m}\left(\frac{z_{0\mathrm{m}}}{L}\right)\right]\left[\ln\frac{z-d_0}{z_{0\mathrm{q}}} - \psi_\mathrm{q}\left(\frac{z-d_0}{L}\right) + \psi_\mathrm{q}\left(\frac{z_{0\mathrm{q}}}{L}\right)\right]}, \tag{3.5.109}$$

where ψ_m, ψ_h, and ψ_q are the integrated gradient functions. d_0 is the zero-plane displacement (the MSM assumes $d_0 = 0$). Following Beljaars and Holtslag (1991), they are given as functions of $\zeta = z/L$,

$$\psi_\mathrm{m}(\zeta) = \begin{cases} -b\left(\zeta - \frac{c}{d}\right)\exp(-d\zeta) - a\zeta - \frac{bc}{d} & (\zeta \geq 0) \\ \frac{\pi}{2} - 2\tan^{-1}x + \ln\frac{(1+x)^2(1+x^2)}{8} & (\zeta < 0) \end{cases}, \tag{3.5.110}$$

$$\psi_\mathrm{h}(\zeta) = \begin{cases} -b\left(\zeta - \frac{c}{d}\right)\exp(-d\zeta) - \left(1 + \frac{2}{3}a\zeta\right)^{\frac{3}{2}} - \frac{bc}{d} + 1 & (\zeta \geq 0) \\ 2\ln\frac{1+x^2}{2} & (\zeta < 0) \end{cases}, \tag{3.5.111}$$

where L is the Monin-Obukhov Length, $\kappa = 0.4$ (von Kármán's constant), and $a = 1$, $b = 2/3$, $c = 5$, $d = 0.35$, and $x = (1 - 16\zeta)^{1/4}$. The integrated gradient function for moisture ψ_q is assumed equal to ψ_h. ζ, which required to calculate $\psi_\mathrm{m}(\zeta)$ and $\psi_\mathrm{h}(\zeta)$, satisfies the following equation,

$$Ri_\mathrm{B} = \zeta\frac{\left[\ln\frac{z-d_0}{z_{0\mathrm{h}}} - \psi_\mathrm{h}\left(\frac{z-d_0}{L}\right) + \psi_\mathrm{h}\left(\frac{z_{0\mathrm{h}}}{L}\right)\right]}{\left[\ln\frac{z-d_0}{z_{0\mathrm{m}}} - \psi_\mathrm{m}\left(\frac{z-d_0}{L}\right) + \psi_\mathrm{m}\left(\frac{z_{0\mathrm{m}}}{L}\right)\right]^2}, \tag{3.5.112}$$

which can be solved by iteration such as the Newton's method. Ri_B is the bulk Richardson Number defined by

$$Ri_\mathrm{B} = \frac{gz_\mathrm{a}}{\frac{1}{2}(\theta_\mathrm{va} + \theta_\mathrm{vs})}\frac{(\theta_\mathrm{va} - \theta_\mathrm{vs})}{U_\mathrm{a}^2}. \tag{3.5.113}$$

$z_{0\mathrm{m}}$, $z_{0\mathrm{h}}$, and $z_{0\mathrm{q}}$ are the roughness length for momentum, heat and moisture respectively. The roughness length on land is set depending on the land use of each grid point. Over the sea, following Beljaars (1995) they are expressed by

$$z_{0\mathrm{m}} = a_\mathrm{m}\frac{\nu}{u_*} + a_\mathrm{Ch}\frac{u_*^2}{g}, \tag{3.5.114}$$

$$z_{0\mathrm{h}} = a_\mathrm{h}\frac{\nu}{u_*}, \tag{3.5.115}$$

$$z_{0\mathrm{q}} = a_\mathrm{q}\frac{\nu}{u_*}, \tag{3.5.116}$$

where $a_\mathrm{m} = 0.11$, $a_\mathrm{Ch} = 0.018$, $a_\mathrm{h} = 0.40$, $a_\mathrm{q} = 0.62$, and ν is the kinematic viscosity ($= 1.5 \times 10^{-5}$ m^2 s^{-1}). u_* is the friction velocity defined by

$$u_* = \left(\overline{u'w'}^2 + \overline{v'w'}^2\right)^{\frac{1}{4}}. \tag{3.5.117}$$

An effect of a stomatal resistance is introduced as following. The surface flux of moisture $\overline{q'_v w'}$ is represented with a resistance coefficient r_a,

$$\overline{q'_{\rm v} w'} = -\frac{1}{r_{\rm a}}(q_{\rm va} - q_{\rm sat}), \quad r_{\rm a} \equiv \frac{1}{C_{\rm q}\beta U_{\rm a}} \,. \tag{3.5.118}$$

$r_{\rm a}$ is corrected to $r_{\rm a} + r_{\rm s}$ when an effect of a stomatal resistance $r_{\rm s}$ is incorporated. $r_{\rm s}$ depends on shortwave radiation flux towards surface S

$$r_{\rm s} = r_{\rm s,\,day} + \frac{r_{\rm s,\,night}}{1 + \dfrac{S}{S_0}} \,, \tag{3.5.119}$$

where $S_0 = 1$ W m^{-2}, $r_{\rm s,\,day}$ is set to 30 s m^{-1} from April to October and 60 s m^{-1} in the other month, and $r_{\rm s,\,night} = 300$ s m^{-1}.

The screen level physical quantities such as wind at 10 m height, temperature and dew point at 1.5 m height are diagnosed by interpolation between the lowest model level and surface assuming the same gradient functions as in the scheme of surface process. Wind velocity at z_{10} (10 m height), u_{10}, and virtual potential temperature at $z_{1.5}$ (1.5 m height), $\theta_{\rm v1.5}$ are diagnosed as

$$u_{10} = \sqrt{\frac{C_{\rm m}(z_{\rm a})}{C_{\rm m}(z_{10})}}\, u_{\rm a} \,, \tag{3.5.120}$$

$$\theta_{\rm v1.5} = \theta_{\rm vs} + \frac{C_{\rm h}(z_{\rm a})}{C_{\rm h}(z_{1.5})} \sqrt{\frac{C_{\rm m}(z_{1.5})}{C_{\rm m}(z_{\rm a})}}(\theta_{\rm va} - \theta_{\rm vs}) \,. \tag{3.5.121}$$

3.5.9 Ground Temperature and Soil Moisture

Ground temperature, which is used in evaluating surface fluxes, is predicted by a multi layer model. The basic equation is the heat conduction equation, in which prognostic variables are temperature T,

$$\rho_c \frac{\partial T}{\partial t} = -\frac{\partial G}{\partial z}, \quad G = -\lambda \frac{\partial T}{\partial z} \,, \tag{3.5.122}$$

where G is the ground heat flux, $\rho_{\rm c}$ is the heat capacity, and λ is the coefficient of the thermal conductivity, respectively. By vertically discretizing soil into N layers (is set to 4 in the MSM, as showing Figure 3.5.3),

$$G_{\rm k} = -2\lambda \frac{T_{\rm k} - T_{\rm k-1}}{\Delta z_{\rm k} + \Delta z_{\rm k-1}} \ (k = 2, \ldots, N), \quad \frac{\partial T_{\rm k}}{\partial t} = -\frac{G_{\rm k+1} - G_{\rm k}}{\rho_{\rm c} \Delta z_{\rm k}} \ (k = 1, \ldots, N-1) \,, \tag{3.5.123}$$

where $\Delta z_{\rm k}$ denotes thickness of k-th layer (concretely $\Delta z_1 = 0.04$ m, $\Delta z_2 = 0.15$ m, $\Delta z_3 = 0.40$ m and $\Delta z_4 = 0.60$ m), and $G_{\rm k}(k \geq 2)$ is given as the gradient of temperature between k-th and $(k-1)$-th layer. G_1 is the heat flux towards surface, which is given by

$$G_1 = (1 - \alpha) S_{\downarrow} + L_{\downarrow} - \sigma T_1^4 - H - lE \,, \tag{3.5.124}$$

where $S_{\downarrow}$ and $L_{\downarrow}$ denote fluxes of shortwave and longwave radiation towards surface, σ is the Stefan-Boltzmann constant, and α is the surface albedo. H and lE represent fluxes of sensible heat and latent heat from the surface,

$$H = -c_{\rm p} \rho \, \overline{\theta'_{\rm v} w'} \,, \tag{3.5.125}$$

$$lE = -l\rho \, \overline{q'_{\rm v} w'} \,, \tag{3.5.126}$$

in which $c_{\rm p}$ is the specific heat of dry air at constant pressure, l is the latent heat of vaporization, and ρ is the density of air at the lowest layer of atmosphere. $G_{\rm k}(k \geq 2)$ can be eliminated as:

$$\frac{\partial T_1}{\partial t} = \frac{G_1}{\rho_{\rm c} \Delta z_1} + \frac{2\Lambda(T_2 - T_1)}{\Delta z_1 (\Delta z_2 + \Delta z_1)} \,, \tag{3.5.127}$$

$$\frac{\partial T_{\rm k}}{\partial t} = -\frac{2\Lambda(T_{\rm k} - T_{\rm k-1})}{\Delta z_{\rm k}(\Delta z_{\rm k} + \Delta z_{\rm k-1})} + \frac{2\Lambda(T_{\rm k+1} - T_{\rm k})}{\Delta z_{\rm k}(\Delta z_{\rm k+1} + \Delta z_{\rm k})} \ (k = 2, \ldots, N) \,, \tag{3.5.128}$$

where $\Lambda \equiv \lambda/\rho_{\rm c}$. λ and $\rho_{\rm c}$ are set as to land use and surface type.

For time integration, the trapezoidal implicit method is adopted. Temporally discretized equations are:

$$T_1^{n+1} = T_1^n + \frac{\Delta t}{2}\left[\frac{G_1^{n+1} + G_1^n}{\rho_{\rm c}\Delta z_1} + \frac{2\Lambda(T_2^{n+1} - T_1^{n+1} + T_2^n - T_1^n)}{\Delta z_1(\Delta z_1 + \Delta z_2)}\right] , \tag{3.5.129}$$

$$T_{\rm k}^{n+1} = T_{\rm k}^n + \Delta t\left[-\frac{\Lambda(T_{\rm k}^{n+1} - T_{\rm k-1}^{n+1} + T_{\rm k}^n - T_{\rm k-1}^n)}{\Delta z_{\rm k}(\Delta z_{\rm k} + \Delta z_{\rm k-1})} + \frac{\Lambda(T_{\rm k+1}^{n+1} - T_{\rm k}^{n+1} + T_{\rm k+1}^n - T_{\rm k}^n)}{\Delta z_{\rm k}(\Delta z_{\rm k+1} + \Delta z_{\rm k})}\right] \ (k = 2, \ldots, N-1) \,, \tag{3.5.130}$$

where

$$G_1^{n+1} = G_1^n + \Delta t\left[\frac{\partial G_1}{\partial t}\right]^{n+1/2} = G_1^n + \Delta t\left[\frac{\partial G_1}{\partial T_1}\frac{\partial T_1}{\partial t}\right]^{n+1/2} \cong G_1^n + \left[\frac{\partial G_1}{\partial T_1}\right]^n (T_1^{n+1} - T_1^n) \,. \tag{3.5.131}$$

If $T_{\rm N}$ is given, these elliptic equations can be solved. In the MSM, T_4 is fixed to climatological value during forecasts. The climatological data for the ground temperature were obtained in the following way. Firstly, monthly mean temperatures at standard pressure levels were calculated from the objective analysis during 1985 and 1986. Next, these data were interpolated vertically to the model ground surface. Then, only the annual mean and the first harmonic component of annual change of the surface temperature are extracted to obtain the climatological underground temperature at the k-th ground layer with the following equation.

$$T_{\rm k} = \hat{T} + A\exp\left(-\frac{z_{\rm k}}{d}\right)\cos\left\{\frac{2\pi}{365}(D - P) - \frac{z_{\rm k}}{d}\right\} \,, \tag{3.5.132}$$

where $\hat{T}$ is the mean ground surface temperature, A and P are the amplitude and the phase of the annual component of the surface temperature, respectively, $z_{\rm k}$ is the depth of the k-th ground layer, d(= 2.65 m) is the e-folding depth and D is the number of day from the beginning of the year.

Furthermore, the sea surface temperature is spatially interpolated from the SST analysis at 18UTC (Section 5.2). It is given as T_1, and is kept constant during the forecast.

Soil moisture is also predicted by the force restore method based on Deardorff (1978):

$$\frac{\partial w_{\rm g}}{\partial t} = -\frac{w_{\rm g} - w_2}{\tau_{\rm g}} + F_{\rm g} \,, \tag{3.5.133}$$

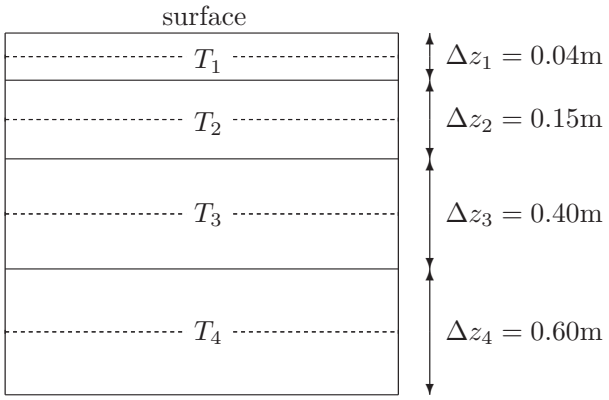

Figure 3.5.3: Structure of the numerical discretization over the layers for the temperatures.

$$\frac{\partial w_2}{\partial t} = F_2 \,, \tag{3.5.134}$$

where w_2 is the mean volumetric water content under the ground, and τ_g is a time constant (= 0.9×86400 s).

Forcing terms F_g and F_2 are given by

$$F_g = -C_g \frac{E - P_r}{\rho_w d_1} \,, \tag{3.5.135}$$

$$F_2 = -\frac{E - P_r}{\rho_w d_2} \,, \tag{3.5.136}$$

where E is the evapolation rate, P_r is the precipitation rate, ρ_w is the density of liquid water, $d_1 = 0.1$ m, and $d_2 = 0.5$ m. C_g is a constant given as following

$$C_g = \begin{cases} 0.5 & \left(\dfrac{w_g}{w_{max}} \geq 0.75\right) \\ 14 - 22.5\left(\dfrac{w_g}{w_{max}} - 0.15\right) & \left(0.15 \leq \dfrac{w_g}{w_{max}} < 0.75\right) \\ 14 & \left(\dfrac{w_g}{w_{max}} < 0.15\right) \end{cases} \,, \tag{3.5.137}$$

where w_{max} is the maximum of volumetric water content (= 0.4).

3.5.10 Parallelization

In order to parallelize computation in the model, the domain is horizontally (two-dimensionally) decomposed into some blocks (Figure 3.5.4) and each of the decomposed blocks is assigned to one process which communicates with other processes through the Message Passing Interface (MPI) (Aranami and Ishida 2004). The processes exchange their data on halo regions when the data on adjacent processes are required for low-order derivatives and interpolation. As the width of the halos is unity, extra halos are temporarily prepared in evaluating the forth order horizontal advection because it requires halos with the width of two or more.

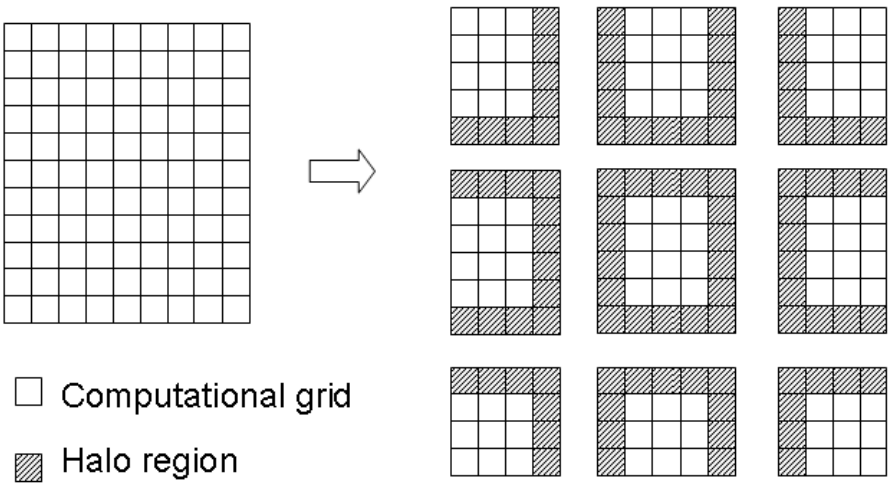

Figure 3.5.4: The whole computational domain (left) and the domain distributed to MPI processes with halo regions (right)

In addition to the processes tied to the decomposed blocks, a special process is exclusively spared to store data into physical disks. As the process can work in background of the main forecasting calculation, time necessary for the output can be hidden and reduced (Figure 3.5.5).

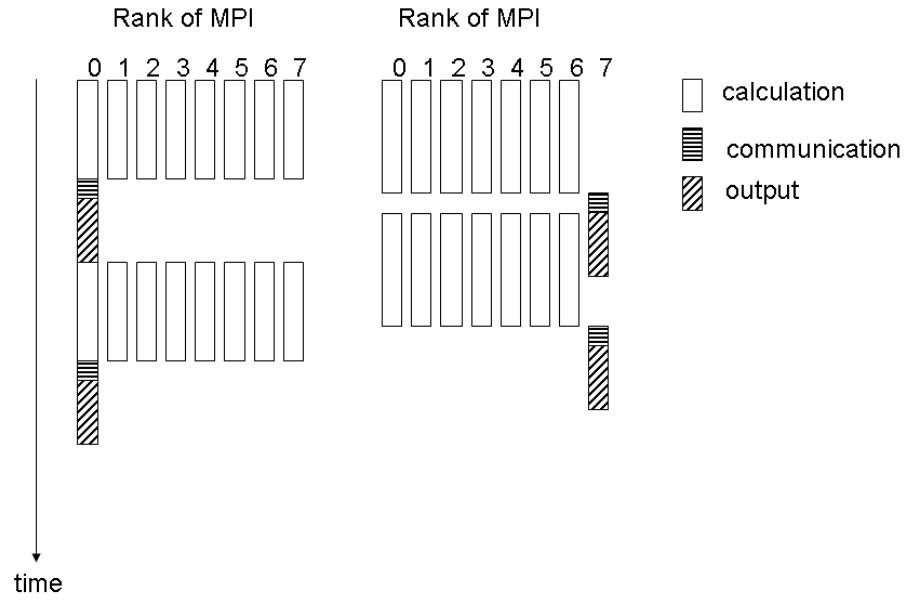

Figure 3.5.5: A diagram of calculation without (left) and with (right) an output process.

Because necessity and sufficiency of conducting MPI communications have been carefully examined, bit-comparable results can be always obtained not depending on the number of processes and how the domain is decomposed. It is very useful and easy to find bugs related to the parallelization.

Within each MPI process, the thread parallelization (SMP) is also applied relying on a function of a Fortran compiler to automatically build parallelized modules.

In the current operation of the MSM, the domain is divided into 17 for x direction and 30 for y direction for the MPI parallelization and additional one process is secured for exclusive data storage. Each MPI process consists of two SMP threads. With this configuration, it takes around 28 minutes to complete 33-hour forecasts of the MSM on Hitachi SR16000/M1 at JMA.

3.5.11 Forecast Performance

Performance of the MSM forecasts has been evaluated by comparing the forecasts with various observations to measure quality of its products and find clues as to further improvements of the model. Especially the accuracy of precipitation forecasts should be emphasized because one of the important purposes of the MSM is to provide information on severe weather phenomena leading to serious disasters.

Figure 3.5.6 and Figure 3.5.7 show time series of threat and bias scores of 3-hour accumulated precipitation forecasts produced by the MSM with the 10-mm threshold from January 2006 to December 2011, respectively. The verification has been performed using "Radar-Raingauge Analyzed Precipitation" (hereafter R/A, see Subsection 4.4.1) as reference observations. (Note that the horizontal resolution of the R/A has been 1-km since March 2006, while the R/A was generated at the 2.5-km resolution until then.) The verification grid size is 20-km, meaning that both the forecasted and observed precipitation over land or sea within 40-km from the coast are averaged over 20-km meshes. Then contingency tables are created by comparing them on each grids.

Figure 3.5.6 and Figure 3.5.7 indicate that the threat score tends to be increasing and the bias score is gradually approaching to unity over the past 6 years. The steady progress has been made by persistent developments of forecast model, data assimilation system, and assimilation method of observation.

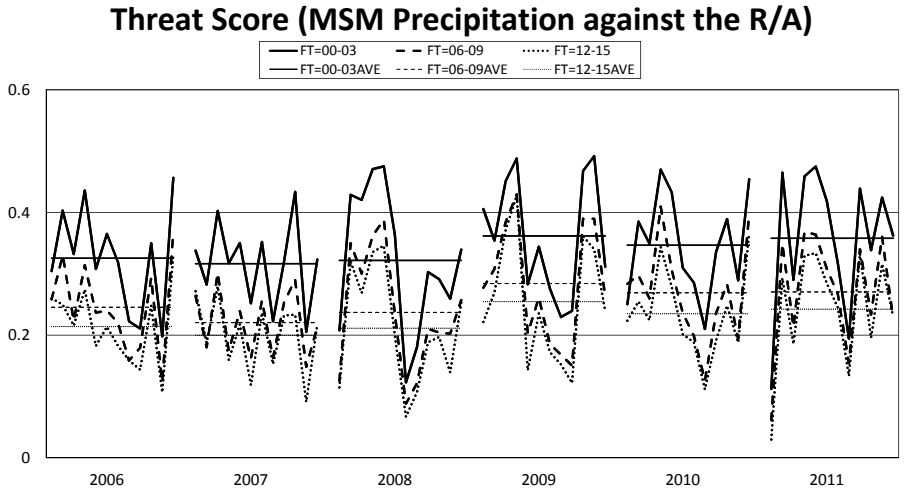

Figure 3.5.6: The monthly threat scores for 3-hour accumulated precipitation by the MSM against the R/A with the threshold of 10mm/3h and within 20km verification grid. The verification period is from January 2006 to December 2011. The thin line means annual average. FT means forecast time from initial time.

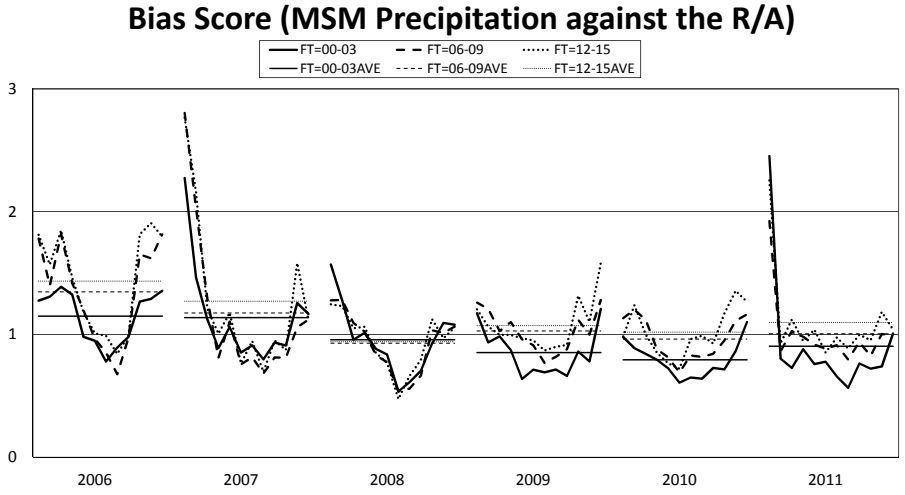

Figure 3.5.7: Same as Figure 3.5.6 but bias scores.

3.6 Local Forecast Model

3.6.1 Introduction

As mentioned in Section 3.5, the Meso-Scale Model (MSM), a numerical weather prediction to provide information on disaster prevention and aviation weather, has been operated since 2001. In its over-ten-year history, horizontal and vertical resolutions have been enhanced: the current MSM covers Japan and its sounding areas with the 5-km grid spacing and places 50 layers in vertical direction up to the height of almost 21.8 km above the surface.

Making use of the new powerful supercomputer system installed in June 2012, operation for a forecast model at an even higher resolution, called the Local Forecast Model (LFM), was launched in August 2012 along with the Local Analysis (LA) described in Section 2.7. The new model has the 2-km horizontal grid spacing and 60 vertical layers up to the height of approximately 20.2km above the surface, and is designed to produce more detailed forecasts with emphasis on predicting localized and short-lived severe events. The LFM focuses on providing very short range forecasts such as 9-hour ahead, and it is intended to quickly and frequently update the forecasts using initial conditions with the latest observations assimilated by the LA.

3.6.2 General Configurations

The LFM has been providing 9-hour forecasts every 3 hours (at 00, 03, 06, 09, 12, 15, 18, 21UTC). The forecast domain covers the eastern part of Japan (shown with the broken line in Figure 2.7.1) with the 2-km horizontal grid spacing.

The LFM employs the identical model to the MSM (the JMA nonhydrostatic model; JMA-NHM) with almost the same configuration mentioned in Section 3.5. Some differences of the configurations between the MSM and the LFM are described below.

- The number and the grid spacings of vertical layers are enhanced in the LFM comparing to those in the MSM. The LFM possesses 60 vertical layers and increases their thicknesses linearly from 40m at the bottom and 678m at the top, while the height of the lowest atmospheric layer is kept the same as that of the MSM. The model top is placed at the height of 20189.5m.

- The LA produces initial conditions with an analysis cycle with hourly 3-dimensional variational method. Boundary conditions are obtained from forecasts performed by the MSM.

- The model is operated with 8-second timestep.

- Strength of the linear and non-linear numerical diffusion should be usually proportional to the horizontal resolution. The time constant for the linear diffusion is set to be 240 seconds as well as that of the non-linear diffusion in the LFM, while both of them are 600 seconds in the MSM.

- The MSM adopts the time splitting of gravity waves (Subsection 3.5.3.5) as the time step (20 seconds) is larger than or comparable to the time scale to propagate the gravity waves (typically 20–30 seconds). Because the time step of the LFM is smaller enough than the time scale, the time splitting is no longer necessary.

- As it is highly expected that considerable part of vertical transport accompanied with convection can be resolved with the grid mean vertical velocity, no convective parameterizations are employed in the LFM. Because convective parameterizations can be the origin of uncertainty of the model, it is preferable to remove them if the resolution is high enough to resolve convective transport.

- As described in Subsection 3.5.6, cloud fraction used in the radiation process is diagnosed considering fluctuations of temperature and water content from their grid mean values over each of the grids. Because the fluctuations are expected to be smaller in higher resolution models, the width of the probability density function depicting behavior of the fluctuation was made smaller.

3.7 Atmospheric Transport Model

3.7.1 Introduction

Since July 1997, JMA has been a Regional Specialized Meteorological Centre (RSMC) with the specialization to provide atmospheric transport model (ATM) products for the environmental emergency response, with responsibility for the Regional Association II (RA-II) of the World Meteorological Organization (WMO). RSMC Tokyo is required to provide advice on the atmospheric transport of pollutants related to nuclear facility accidents and radiological emergencies. The RSMC's ATM products are sent to the National Meteorological Services (NMS) of the WMO Member States in RA-II, and the secretariats of WMO and of the International Atomic Energy Agency (IAEA). The basic procedure of the service is defined in WMO (2010a).

3.7.2 Model

3.7.2.1 Basic Framework

ATM used in JMA is based on Iwasaki *et al.* (1998) with some modifications like one found in Kawai (2002), and it follows a Lagrangian approach, where many tracer particles are released at the time and location of the pollutant emission are displaced due to horizontal and vertical advection and diffusion, and dropped through dry and wet deposition. Advection, diffusion and deposition are computed using 3-hourly model-level outputs from the operational global numerical weather prediction (NWP) model: GSM. The horizontal and vertical displacements during 1 time step δt are given as follows:

$$\delta x = u\delta t + G\sqrt{2k_h\delta t} \tag{3.7.1}$$

$$\delta y = v\delta t + G\sqrt{2k_h\delta t} \tag{3.7.2}$$

$$\delta z = w\delta t + \Sigma G\sqrt{2k_v\delta t'} \tag{3.7.3}$$

where k_h and k_v are horizontal and vertical diffusion coefficients respectively, and Gs are random displacements whose statistical distributions take the Gaussian distribution functions with mean 0 and standard deviation 1. The Monte Carlo method is used to determine displacement of each tracer particle so that it results in a Gaussian distribution. The time step for the integration of the vertical diffusion $\delta t'$ is much less than those for integrations of horizontal diffusion and advection. Tracer particles are also removed from the atmosphere due to dry and wet deposition and radioactive decay.

3.7.2.2 Vertical and Horizontal Diffusion Coefficients

The vertical diffusion coefficient depends on atmospheric vertical profiles. A shorter time step is used so that a vertical displacement due to diffusion becomes smaller than the thickness of the model layer.

The vertical diffusion coefficient k_v is decided referring meteorological parameters on the sigma-pressure hybrid levels by a procedure in the analogous with the molecular diffusion coefficient estimation by Louis *et al.* (1982). The vertical diffusion coefficient is given as follows:

$$k_v = l^2\left|\frac{\partial v}{\partial z}\right|F(R_i) \tag{3.7.4}$$

where the parameters l and R_i are the vertical mixing length of turbulence and the Flux Richardson number, respectively. The similarity function of $F(R_i)$ is taken from Louis *et al*. (1982). The mixing length is written as a function of geometric height z

$$l = \frac{kz}{1 + kz/l_0} \tag{3.7.5}$$

where k is von Kármán's constant and l_0 is the maximum mixing length.

Table 3.7.1: Other Specifications of the ATM

Number of Tracers	100,000
Grid Type for the Calculations of Concentration and Deposition	Lat Lon-grid
Size of the Calculation Grid	(lat) 1.0 × (lon) 1.0 degree

The horizontal diffusion coefficient k_h should be parameterized considering the model resolution and temporal and spatial variations of meteorological fields. An appropriate constant value is set in the model to save computational time.

3.7.2.3 Dry and Wet Deposition

The surface tracer flux F_s due to dry deposition is presented by means of the deposition velocity $V(z_r)$ and concentration $C(z_r)$ at a reference level z_r as

$$F_s \equiv V(z_r)C(z_r) \tag{3.7.6}$$

For simplicity, the deposition rate is set to F_s/z_r according to Kitada *et al.* (1986).

Concerning wet deposition, only wash-out processes are parameterized. The wet deposition rate is approximated as a function of precipitation intensity P(mm/h) predicted by the meteorological model (GSM) with the below-cloud scavenging ratio per hour given by

$$\Lambda \approx 0.1 \times P^{0.75} \tag{3.7.7}$$

according to Kitada (1994). The Monte Carlo method is applied to decide whether each tracer particle is removed from the atmosphere at the above-mentioned dry and wet deposition rates.

Other specifications of the ATM are presented in Table 3.7.1.

3.7.3 Products

The ATM products consist of the charts of 3D trajectories, of the time integrated pollutant concentrations, and of the total depositions. Sample charts are shown in Figure 3.7.1 - Figure 3.7.7. The way to interpret these products is found in Appendix II-7 of WMO (2010).

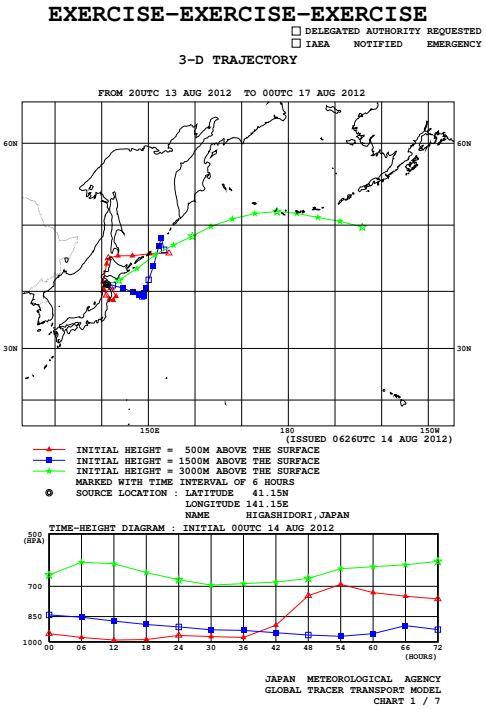

Figure 3.7.1: An example of the 3D trajectories

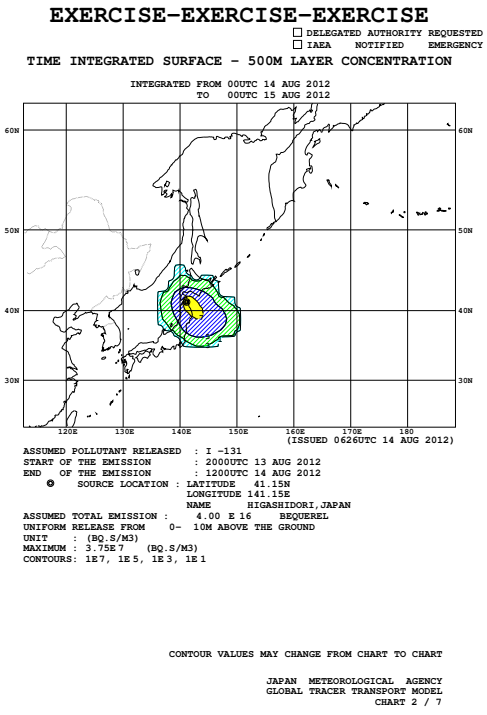

Figure 3.7.2: An example of the time integrated concentration up to 24 hours forecast

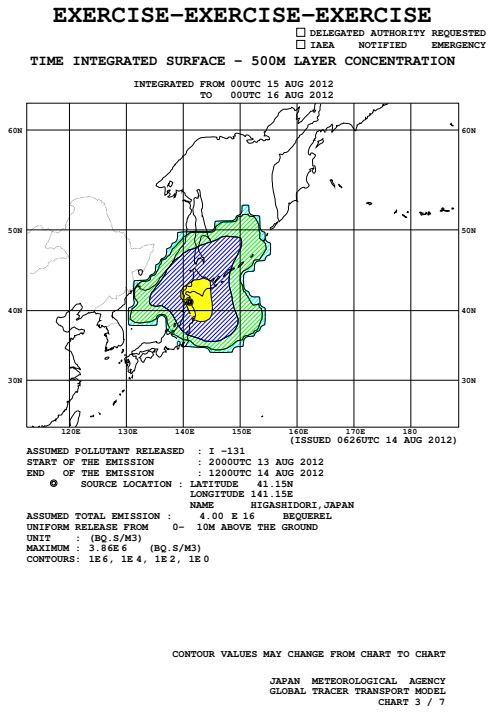

Figure 3.7.3: An example of the time integrated concentration up to 48 hours forecast

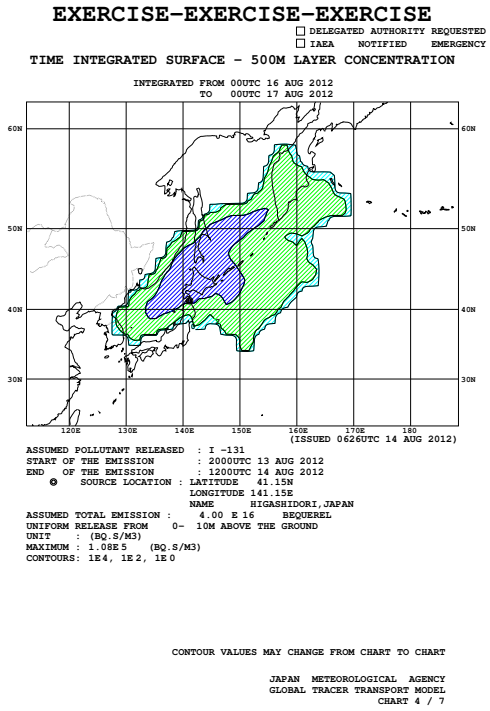

Figure 3.7.4: An example of the time integrated concentration up to 72 hours forecast

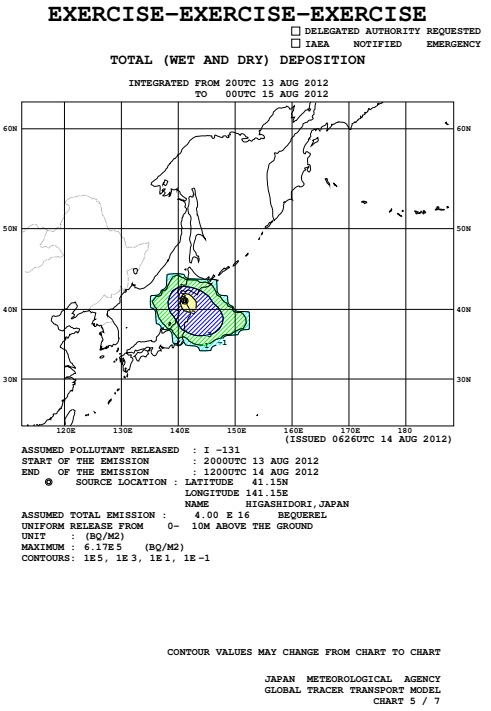

Figure 3.7.5: An example of the total deposition by 24 hours forecast time

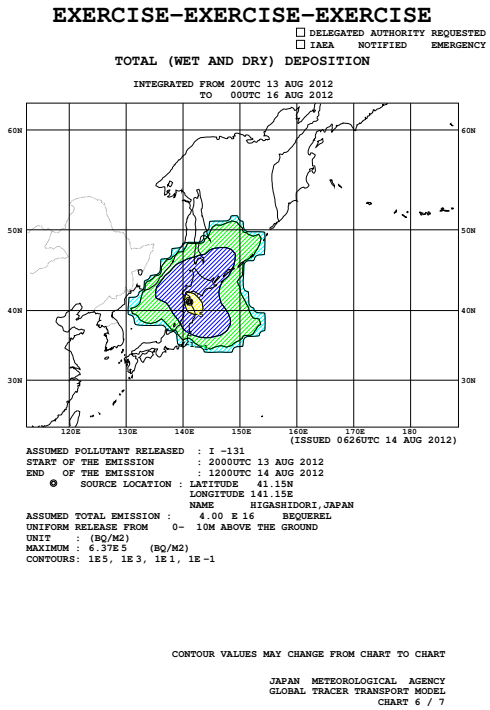

Figure 3.7.6: An example of the total deposition by 48 hours forecast time

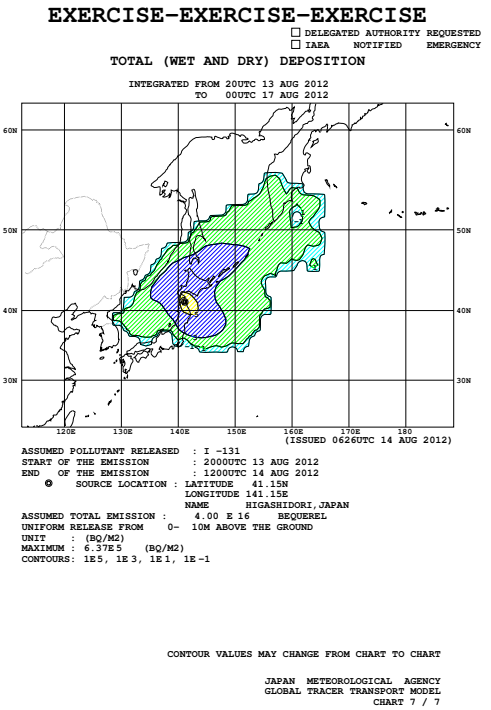

Figure 3.7.7: An example of the total deposition by 72 hours forecast time

3.8 Chemical Transport Model

3.8.1 Introduction

JMA has provided various types of atmospheric environmental information such as a Kosa (Aeolian dust) forecast, UV-index forecast and a photochemical oxidant forecast information through the JMA website (Figure 3.8.1 to Figure 3.8.3), simulated by Chemical Transport Models (CTMs). JMA has operated a Kosa prediction CTM since January 2004, stratospheric ozone CTM for the UV-index prediction system since May 2005 and tropospheric-stratospheric ozone CTM for the photochemical oxidant information since August 2010.

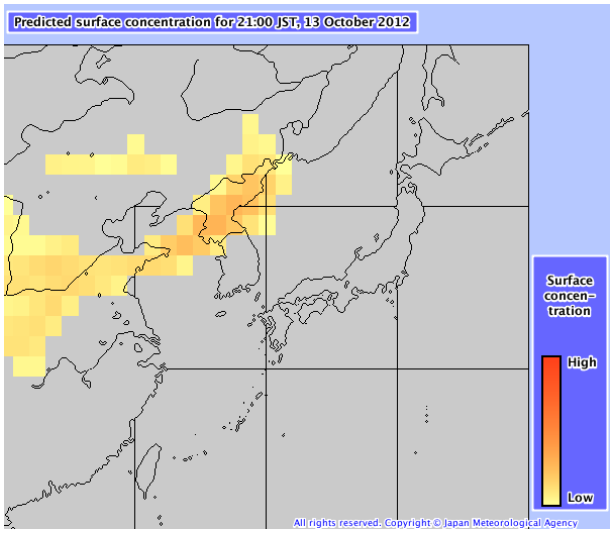

Figure 3.8.1: Kosa information forecast web page(`http://www.jma.go.jp/en/kosafcst/`).

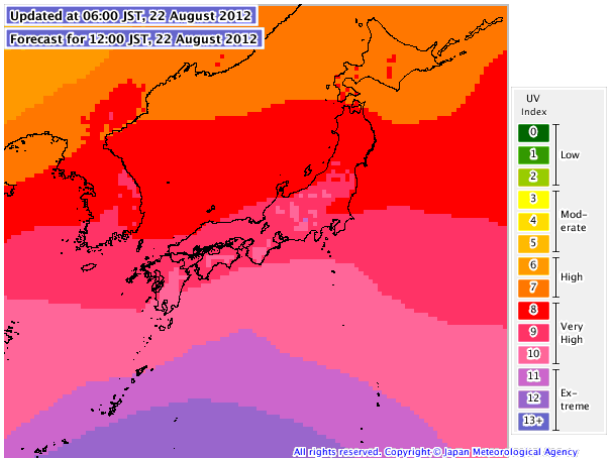

Figure 3.8.2: Clear sky UV index forecast web page(`http://www.jma.go.jp/en/uv/`).

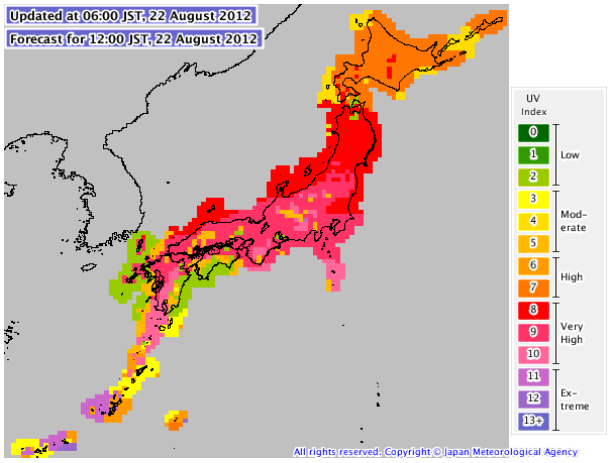

Figure 3.8.3: UV index forecast web page(`http://www.jma.go.jp/en/uv/`).

3.8.2 General Circulation Model

3.8.2.1 Basic Framework

In the CTMs, the chemical modules are directly coupled with a General Circulation Model (MRI/JMA98; Shibata *et al.* (1999)) and use several GCM parameters without any temporal or spatial interpolation. The schematic illustrations of the CTMs structures are shown in Figure 3.8.4 to Figure 3.8.6. The GCM used here is a global spectral model based on an operational weather forecasting model in 1996 (GSM9603) in the JMA, and some improvements are made in physical processes. For example, the solar and terrestrial radiation scheme (Chiba *et al.* 1996) is used to yield temperature distributions in the middle atmosphere with modest accuracy. The soil temperatures are divided into three layers, which are similar to those for soil water, leading to a precise treatment of melting and freezing of water through the consistency between heat and water budgets.

3.8.2.2 Relaxation to Analyzed/Forecasted Field

In general, a CTM needs more computational resources than a GCM because the CTM deals with the more variables and chemical processes than the GCM, and a lower spatial resolution of CTM is adopted for operation. Because of the difference of the resolution and physical and dynamical processes of GCM, the meteorological field will not be consistent with the operational analyzed and forecasted field. To solve this problem, the GCM has a built-in, four-dimensional data assimilation with a nudging scheme incorporating an analyzed and forecasted meteorological field as in Eq. (3.8.1),

$$\left(\frac{\partial x}{\partial t}\right)_{nudging} = -\frac{x - x_{analysis/forecast}}{T} \tag{3.8.1}$$

where x is the dynamical variable, $x_{analysis/forecast}$ is the analyzed/forecasted variable, and T is the time scale of relaxation of 6-24 hours. This scheme enables the CTM to simulate a meteorological field realistically during a forecast period.

3.8.3 Aerosol CTM Used for Kosa Prediction

3.8.3.1 Basic Framework

The Chemical Transport Model used for Kosa prediction was named as a Model of Aerosol Species IN Global Atmosphere (MASINGAR; Tanaka *et al.* (2003)). The MASINGAR consists of transport modules of advective transport (3D semi-Lagrangian scheme), sub-grid scale eddy diffusive and convective transport, and other

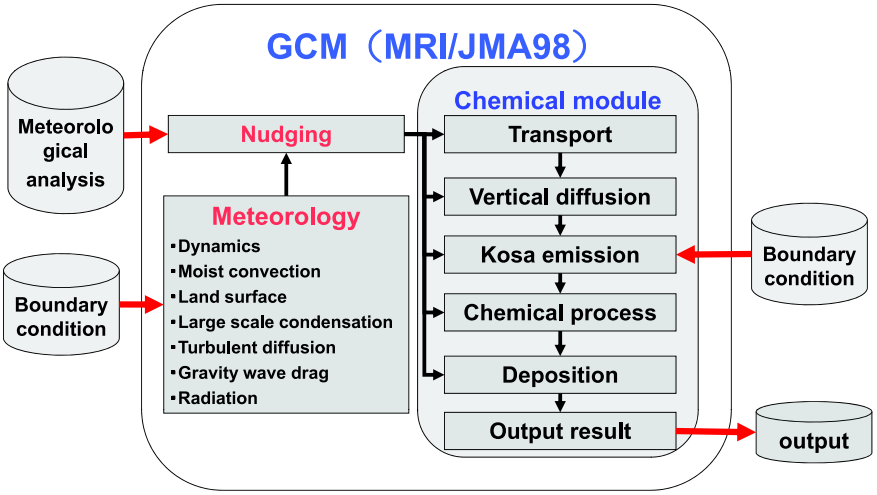

Figure 3.8.4: The schematic illustration of the structure of Kosa CTM.

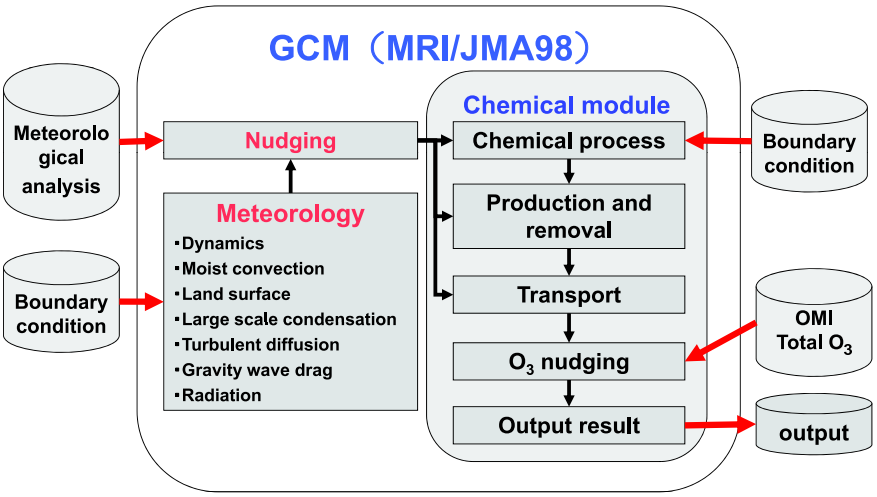

Figure 3.8.5: The schematic illustration of the structure of stratospheric ozone CTM.

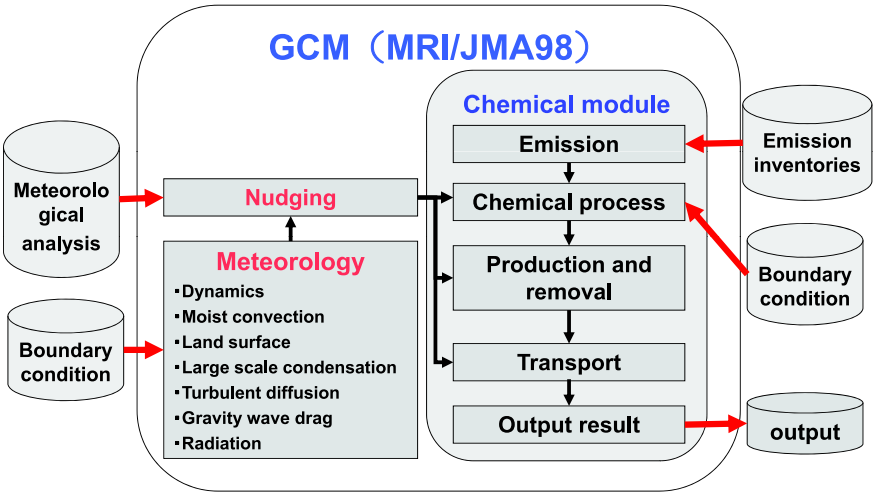

Figure 3.8.6: The schematic illustration of the structure of stratospheric-tropospheric ozone CTM.

modules of surface emission and dry/wet depositions as well as chemical reactions. Although it deals with many types of aerosols such as non-sea-salt sulfate, carbonaceous, mineral dust and sea-salt, only mineral dust aerosol is dealt with in the operational model for Kosa prediction, where the forecast period is 96 hours and the resolution of GCM is T106L30 up to 5 hPa. The vertical resolution of the chemical module is reduced to 20 layers (up to 42 hPa) from 30 of the GCM in order to reduce computational cost. The emission flux of mineral dust aerosol depends on meteorological, geographical and soil surface conditions, such as wind speed, land use, vegetation type, soil moisture and soil types. The dust emission flux F is expressed as a function of dust size and wind speed at 10 m (U_{10}):

$$F = CMA\frac{W_{gt} - W_g}{W_{gt}}\left(U_{10} - U_t\right)U_t^2 \quad \text{for} \quad U_{10} > U_t \text{ and } W_{gt} > W_g \tag{3.8.2}$$

where a threshold wind velocity U_t is set to 6.5 m/s, C is a dimensional factor, M is the mass ratio of dust at a size bin to the total mass, A is the erodible fraction at the surface, W_g is the soil moisture, and W_{gt} is the threshold soil moisture (currently set to 0.3 kg/m^3).

3.8.3.2 Relaxation to Analyzed/Forecasted Field

Due to the lack of real-time and three-dimensional observational data of Kosa aerosol, the chemical module in the MASINGAR is not assimilated with the Kosa aerosol observations. However, because the Kosa emissions are very sensitive to the land surface conditions such as soil water and snow, the chemical module in Kosa prediction model has a nudging system with snow depth analysis. This system improves snow forecast in GCM to be close to the actual snow cover on the surface. The types of datasets used for nudging system in Kosa prediction model is shown in Table 3.8.1.

Table 3.8.1: Types of dataset used for nudging system in Kosa prediction model

	From -24 hour to initial	From initial to 48 hour forecast
Meteorological field	Global analysis	Global forecast
Snow depth	Snow depth analysis	-

Table 3.8.2: Verification indices for categorical forecast

	Observed(ww = 06 – 09, 30 – 35, 98)	Not Observed (ww = 00 – 05)
Forecasted (Surface Kosa concentration is higher than 90μg/m^3)	FO	FX
Not Forecasted (Surface Kosa concentration is lower than 90μg/m^3)	XO	XX

3.8.3.3 Verification

The forecast by the operational Kosa prediction model is verified against the surface synoptic observation (present weather (ww)). We have calculated the model score using categorical verification similar to Appendix A (shown in Table 3.8.2). The threshold value for Kosa forecast is currently set to be 90 μg/m^3. The threat score of the Kosa prediction model at 24 hour forecast in an area of Japan are 0.42, 0.39 and 0.41 in 2009, 2010 and 2011 spring, respectively.

3.8.4 Stratospheric Ozone CTM Used for UV Index Prediction

3.8.4.1 Basic Framework

The stratospheric ozone CTM composed of chemical and transport processes was developed by Shibata *et al.* (2005). The chemical processes, which are based on the family method, contain major stratospheric species, i.e., 34 long-lived species including 7 families and 15 short-lived species with 79 gas phase reactions and 34 photodissociations. The names of these species are shown in Table 3.8.3. The model includes two types of heterogeneous reactions on the surfaces of polar stratospheric clouds (PSCs) and sulfate aerosols. The ozone CTM predicts a 48-hour forecast with a resolution of T42L68 up to 0.01 hPa.

The transport scheme of chemical species adopts a hybrid semi-Lagrangian transport scheme, which is compatibly solved with the continuity equation and has different forms for horizontal and vertical directions (Shibata *et al.* 2005). The horizontal form has an ordinary semi-Lagrangian scheme while the vertical form is equivalent to a mass-conserving flux-form in transformed pressure coordinates specified by the vertical velocity. In addition, the operational global spectral model uses three-dimensional monthly-mean ozone climatology data that were produced by the CTM with nudging towards satellite data (TOMS).

3.8.4.2 Relaxation to Observational Data

The chemical module in the stratospheric ozone CTM has an assimilation system similar to meteorological field (Eq. (3.8.1)), which can assimilate total ozone once a day obtained from the satellite measurement of Ozone Monitoring Instrument (OMI/Aura). The weight of the model guess to OMI data is determined by the ratio of the root mean square errors against the surface observational data. We adopt a third as the ratio of relative contribution of CTM to OMI for nudging. The ozone CTM incorporates a meteorological assimilation system from minus 72 hours to 48 hours with data assimilation to satellite measurements of total ozone, as shown in Table 3.8.4

Table 3.8.3: Names of species used in the stratospheric ozone CTM

Long-lived					
01: N_2O	02: CH_4	03: H_2O	04: NO_y	05: HNO_3	06: N_2O_5
07: Cl_y	08: O_x	09: CO	10: OClO	11: CO_2	12: Aerosols
13: HCl	14: $ClONO_2$	15: HOCl	16: Cl_2	17: H_2O_2	18: $ClNO_2$
19: HBr	20: $BrONO_2$	21: NO_x	22: HO_2NO_2	23: ClO_x	24: BrO_x
25: Cl_2O_2	26: HOBr	27: CCl_4(CFC-10)	28: $CFCl_3$(CFC-11)	29: CF_2Cl_2(CFC-12)	30: Br_y
31: CH_3Cl	32: CH_3Br	33: CF_2ClBr (Halon1211)	34: CF_3Br (Halon1301)		
O_x = O_3 + O(3P) + O(1D)					
ClO_x = Cl + ClO	Cl_y = ClO_x + OClO + $2Cl_2O_2$ + HCl + $ClONO_2$ + HOCl + $2Cl_2$ + $ClNO_2$ + BrCl				
NO_x = NO + NO_2 + NO_3	NO_y = NO_x + N + HNO_3 + $2N_2O_5$ + HO_2NO_2 + $ClONO_2$ + $ClNO_2$ + $BrONO_2$				
BrO_x = Br + BrO + BrCl	Br_y = BrO_x + HBr + HOBr + $BrONO_2$				
Short-lived					
01: O(1D)	02: OH	03: Cl	04: O(3P)	05: O_3	06: HO_2
07: NO_2	08: NO	09: Br	10: N	11: ClO	12: BrO
13: NO_3	14: BrCl	15: H			

Table 3.8.4: Types of datasets used for nudging system in stratospheric ozone CTM

	From -72 hour to initial	From initial to 48 hour forecast
Meteorological field	Global analysis	Global forecast
Total ozone	OMI daily data	-

3.8.4.3 Verification

The predictability of CTM on total ozone was investigated for up to 4 weeks from 1997 to 2000 (Sekiyama and Shibata 2005). Root-mean-square errors (RMSEs) of the control run for the hindcast experiments range from 10 to 30 DU in the whole earth and global average of RMSEs are approximately 10 DU (3% of total ozone) throughout the year. The anomaly correlation between the 5-day forecasts and satellite measurements is approximately 0.6 throughout the year in the extratropical regions in the both hemispheres, suggesting that the model utilizes total ozone forecasts up to 5 days. Furthermore, in the extratropical regions, the model can produce better total ozone forecasts up to 2 weeks.

3.8.4.4 Radiative Transfer Model for UV Index Prediction Using Look-Up Table Method

The surface UV dose is calculated under clear-sky conditions by the radiative transfer model (Aoki *et al.* 2002) in an area from 122°E to 149°E and from 24°N to 46°N with a grid resolution of 0.25° x 0.20°. A Look-Up Table (LUT) method is used to reduce the computational cost. The basic parameters of LUT for the clear-sky UV are the solar zenith angle and the total ozone predicted by the CTM. The clear-sky UV index is derived from clear-sky UV dose corrected by climatological aerosol, distance from the sun, altitude, and climatological surface albedo. The forecast UV index is corrected by a categorization of weather forecast.

The clear sky UV index calculated by the LUT is verified against the observed UV index. The result is shown in Figure 3.8.7. The mean error of the calculated clear sky UV index is 0.0 and the RMSE is 0.5. We find that modeled UV indices are well simulated to observed ones.

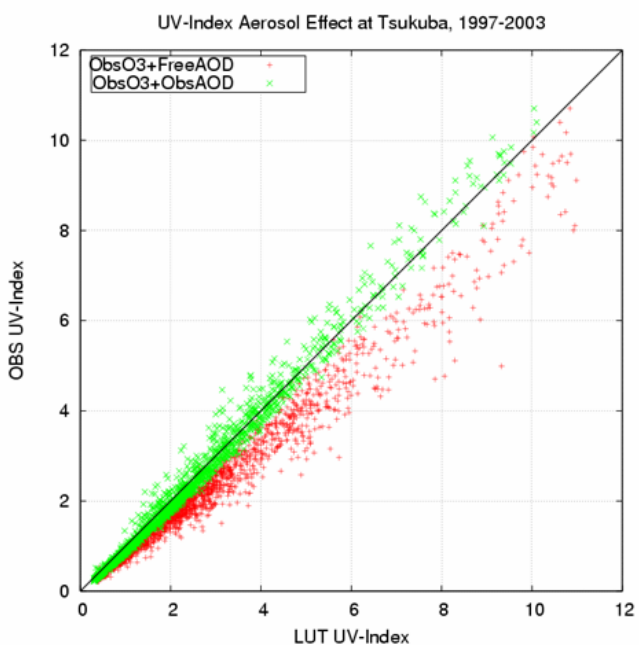

Figure 3.8.7: Relationship between the observed and calculated UV indices. The green cross marks show the UV index with the correction of measured aerosol optical depth and the red-plus marks show the UV index without aerosol correction.

3.8.5 Tropospheric-Stratospheric Ozone CTM Used for Photochemical Oxidant Information

3.8.5.1 Basic Framework

JMA has provided photochemical oxidant information by a CTM for the whole of Japan since August 2010. The information is produced by combining a global tropospheric-stratospheric ozone CTM (MRI-CCM2; Deushi and Shibata (2011)) incorporating chemical transport processes of photochemical oxidants in the troposphere/stratosphere and statistical guidance induced from model outputs associated with past events. The framework of this model is similar to that of the stratospheric ozone CTM (MRI-CCM: referred in Subsection 3.8.4). The MRI-CCM2 was produced to add detailed tropospheric chemistry to the MRI-CCM in order to treat ozone chemistry in both the troposphere and stratosphere seamlessly. The chemistry module includes 90 chemical species (64 for the long-lived species and 26 for the short-lived species) with 172 gas-phase reactions, 59 photolysis reactions and 16 heterogeneous reactions. The names of these species are shown in Table 3.8.5. The forecast period is 72 hours and the resolution is T106L30 up to 0.4 hPa. The model adopted the improved grid-scale transport with a semi-Lagrangian scheme, sub grid-scale convective transport and turbulent diffusion, dry and wet deposition, and emissions of trace gases from various sources.

As for the emission of the trace gases imposed at the surface, we use the statistical inventories shown in Table 3.8.6.

The dynamical module in the MRI-CCM2 also has an assimilation system in the meteorological field. Types of datasets used for nudging system in tropospheric and stratospheric ozone prediction model are shown in Table 3.8.7.

3.8.5.2 Verification

We compared the simulated ozone field to the observation. The simulated seasonal cycle of the ozone mixing ratio at 800 hPa reproduces the observed seasonal cycle at ozonesonde measurement stations (Deushi and

Table 3.8.5: Names of species used in the tropospheric-stratospheric ozone CTM

Long-lived			
01: N_2O	02: CH_4	03: H_2O	04: NO_y
05: HNO_3	06: N_2O_5	07: Cl_y	08: O_x
09: CO	10: OClO	11: CO_2	12: Passive tracer
13: HCl	14: $ClONO_2$	15: HOCl	16: Cl_2
17: H_2O_2	18: $ClNO_2$	19: HBr	20: $BrONO_2$
21: NO_x	22: HO_2NO_2	23: ClO_x	24: BrO_x
25: Cl_2O_2	26: HOBr	27: CCl_4(CFC-10)	28: $CFCl_3$(CFC-11)
29: CF_2Cl_2(CFC-12)	30: Br_y	31: CH_3Cl	32: CH_3Br
33: CF_2ClBr (Halon1211)	34: CF_3Br (Halon1301)	35: COF_2	36: HF
37: CH_2O	38: CH_3OOH	39: C_2H_6	40: CH_3CHO
41: C_2H_5OOH	42: PAN ($CH_3C(O)OONO_2$)	43: $CH_3C(O)OOH$	44: C_3H_8
45: ACET ($CH_3C(O)CH_3$)	46: C_3H_7OOH	47: HACET ($CH_3C(O)CH_2OH$)	48: MGLY ($CH_3C(O)CHO$)
49: C_2H_4	50: GLY ALD ($HOCH_2CHO$)	51: GPAN ($HOCH_2C(O)OONO_2$)	52: GC(O)OOH ($HOCH_2C(O)OOH$)
53: C_3H_6	54: ONIT ($CH_3C(O)CH_2ONO_2$)	55: POOH (HOC_3H_6OOH)	56: C_4H_{10}
57: C_5H_8 (isoprene)	58: MACR	59: ISON	60: ISOPOOH
61: NALD	62: MACROOH	63: MPAN	64: $C_{10}H_{16}$ (terpenes)
Short-lived			
01: O(1D)	02: OH	03: Cl	04: O(3P)
05: O_3	06: HO_2	07: NO_2	08: NO
09: Br	10: N	11: ClO	12: BrO
13: NO_3	14: BrCl	15: H	16: CH_3O_2
17: $C_2H_5O_2$	18: $CH_3C(O)O_2$	19: $C_3H_7O_2$	20: $ACETO_2$ ($CH_3C(O)CH_2O_2$)
21: EO_2 ($HOC_2H_4O_2$)	22: EO (HOC_2H_4O)	23: $GC(O)O_2$ ($HOCH_2C(O)O_2$)	24: PO_2 ($HOC_3H_6O_2$)
25: $ISOPO_2$	26: $MACRO_2$		
Chemical families			
O_x = O_3 + O(3P) + O(1D)			
ClO_x = Cl + ClO			
Cl_y = ClO_x + OClO + $2Cl_2O_2$ + HCl + $ClONO_2$ + HOCl + $2Cl_2$ + $ClNO_2$ + BrCl			
NO_x = NO + NO_2 + NO_3			
NO_y = NO_x + N + HNO_3 + $2N_2O_5$ + HO_2NO_2 + $ClONO_2$ + $ClNO_2$ + $BrONO_2$ + PAN + GPAN + ONIT + ISON + NALD + MPAN			
BrO_x = Br + BrO + BrCl			
Br_y = BrO_x + HBr + HOBr + $BrONO_2$			

Table 3.8.6: The emission inventories of trace gases used in the MRI-CCM2

name	emission sources	coverage
EDGAR v2.0 (Olivier *et al.* 1996)	anthropogenic	global
GEIA (Guenther *et al.* 1995)	natural	global
REAS1.1 (Ohara *et al.* 2007)	anthropogenic	East Asia

Table 3.8.7: Types of datasets used for nudging system in tropospheric-stratospheric ozone CTM

	From -24 hour to initial	From initial to 48 hour forecast
Meteorological field	Global analysis	Global forecast

Shibata 2011). At the Naha station which is located in the East China Sea, the model captures well the observed summertime minimum due to the evolution of continental air mass to a maritime one, which implies that the chemical destruction of O_x in the summer maritime air mass is adequately simulated (Figure 3.8.8).

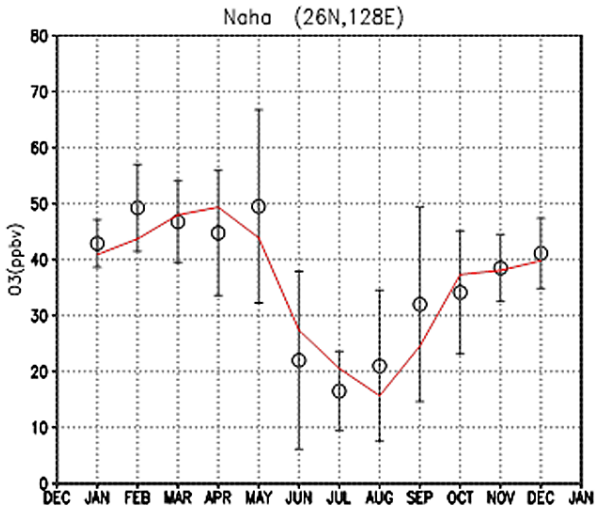

Figure 3.8.8: Annual cycle of observed ozone mixing ratios (in ppb by volume) (open circles) with standard deviations (error bars) at Naha station for the 800 hPa level by ozonesonde measurements, and the simulated mixing ratios (red line) of the FREE-run averaged over 10 years at the corresponding location (Deushi and Shibata 2011).

3.9 Verification

In JMA, the forecast results of the Numerical Weather Prediction (NWP) models are operationally verified against observations and/or analyses. The results of the verification are used for the reference of research and development of the NWP models. The verification results of GSM are exchanged between JMA and the other NWP centers through the Global Data-processing and Forecasting System (GDPFS) of Commission for Basic Systems (CBS) in World Meteorological Organization (WMO), based on the Manual on the GDPFS (WMO 2010a). The standard procedure of the verifications for the deterministic NWP model is coordinated in the Coordination Group on Forecast Verification (CG-FV), CBS (WMO 2012). In this section, the operational verifications for GSM, MSM and One-week EPS are summarized.

The specifications of the verifications for GSM and MSM against analysis are shown in Table 3.9.1. Although the operation of the Regional Spectral Model (RSM) for the east Asian area was discontinued in November 2007, the RSM core region is used for the continuity of the verification. The scores used for the verifications indices are presented in Appendix A. The adjacent zones to the boundaries are excluded from the verification for MSM, because the limited area models such as MSM have lateral boundaries and the adjacent zones to the boundaries are strongly affected by an outer coarse mesh model such as GSM. The remaining areas are called core regions. The forecast performance of GSM including typhoon forecast are described in Subsection 3.2.13. The results of the categorical verification for precipitation forecasts of MSM are presented in Subsection 3.5.11. As mentioned in Section 3.6, LFM was put into operation in August 2012, and the verification results are to be prepared.

Radiosonde data are used for the verification against observations. The specifications of the verification against radiosonde data for GSM and MSM are shown in Table 3.9.2. All of the radiosonde data that have passed quality control are used for the verification for GSM and MSM. The stations of which radiosonde data is to be used in the verification for GSM are selected according to the recommendation of CBS.

Table 3.9.1: Operational Verification against Analysis

	GSM	MSM
Verification Grid Size	2.5°	40km
Element	Z, U, V, T and wind speed at 850, 500 and 250hPa Psea; RH at 850 and 500hPa; total precipitable water	
Score	mean error, root mean square error, anomaly correlation, standard deviation, S1 score	
Time Interval	6 hours	6 hours
Verification Area	NH(90°N – 20°N), SH(20°S – 90°S), TR(20°N – 20°S), RSM core region	MSM core region

Table 3.9.2: Operational Verification against Radiosonde Data

	GSM	MSM
Verification Grid Size	2.5°	40km
Element	Z, U, V, T and wind speed at 850, 500 and 250hPa; RH at 850hPa and 500hPa	
Score	mean error, root mean square error, standard deviation	
Time Interval	12 hours	6 hours
Verification Area	NH,SH,TR, North America, Europe, Asia, Australia, RSM core region	MSM core region

The specifications of the verification against the surface observations for GSM and MSM are shown in Table 3.9.3, Table 3.9.4, and Table 3.9.5. JMA operates a surface observation network with high spatial resolution called Automated Meteorological Data Acquisition System (AMeDAS), which consists of about 1300 stations with raingauges, about 310 stations with snowgauges, and about 840 stations with thermometer, aerovanes and heliographs in Japan. The average intervals of the AMeDAS stations are about 17 km for raingauges and about 21km for the others. The AMeDAS data are used for the verification of forecast performance on both precipitation and temperature at the surface. The observation data are converted into a set of grid mesh data with a uniform spatial resolution of 80 km to be compared with the forecasts and to reduce sampling error of observation. As a consequence, the continuity for the verification is kept, even if the resolutions of models are changed.

The network of C-band Doppler radars (with a wavelength of 5.6 cm) covers most of Japan's territory, and observes rainfall intensity and distribution. Radar data are digitized to produce special radar-echo composite maps every five minutes for the purpose of monitoring precipitation throughout the country. The data are also calibrated with raingauge data of AMeDAS, and are used for a precipitation analysis over the coverage in Japan. Table 3.9.6 shows the specifications of the verification for GSM and MSM against Radar-Raingauge Analyzed Precipitation. Since the precipitation analysis provides very dense (about 1km) information making up for the raingauge data, it is capable to evaluate forecast skills on meso-scale disturbances. It is also used for the verification of typhoon forecast, along with the best track of TC track and central pressure analyzed by the RSMC Tokyo - Typhoon Center in JMA.

A low-resolution version of GSM is used for the operational EPSs (see Section 3.3), which are also verified operationally. The specifications of the verification for One-week EPS are shown in Table 3.9.7. The probabilistic forecasts for the verification is defined as the ratio of the number of ensemble members occurred in an event to the ensemble size at every grid. The verification results for One-week EPS are described in Section 3.3.

Table 3.9.3: Operational Verification against AMeDAS Raingauge Observation (quantitative)

	GSM	MSM
Verification Grid Size	80km	
Score	mean of observation, mean of forecast, root mean square error, correlation, standard deviation of observation, forecast and error	
Time Interval	12 hours	3, 6 and 12 hours
Verification Area	whole and 6 districts of Japan	

Table 3.9.4: Operational Verification against AMeDAS Raingauge Observation (categorical)

	GSM	MSM
Verification Grid Size	80km	
Score	threat score, bias score	
Time Interval	12, 24 hours	3, 6 and 12 hours
Threshold	1, 5, 20, 50mm	
Verification Area	whole and 6 districts of Japan	

Table 3.9.5: Operational Verification against AMeDAS Temperature Observation

	GSM	MSM
Verification Grid Size	80km	
Score	mean error, root mean square error	
Time Interval	3 hours maximum, minimum	3 hours maximum, minimum
Verification Area	whole and 6 districts of Japan	

Table 3.9.6: Operational Verification against Radar-Raingauge Analyzed Precipitation (categorical)

	GSM	MSM
Verification Grid Size	20, 40 and 80km	5, 10, 20, 40 and 80km
Score	threat score, bias score	
Time Interval	3 and 6 hours	1, 3 and 6 hours
Threshold	1, 5, 10, 20mm	1, 5, 10, 20, 50mm
Verification Area	whole of Japan	

Table 3.9.7: Operational Verification for One-week EPS

	Deterministic Verification	Probabilistic Verification	
Analysis	Global analysis on $2.5^\circ \times 2.5^\circ$ grid	Global analysis on $2.5^\circ \times 2.5^\circ$ grid	
Forecast	Ensemble mean and all members	Probability	
Climatology	Climatological fields and standard deviations are calculated from JRA-25. The climatological probability is given by the monthly frequency derived from analysis fields.		
Element	Z at 1000 and 500hPa; T at 850 and 500hPa; U and V at 850 and 250hPa; Psea	Anomalies of Z at 500hPa, T at 850hPa and Psea with thresholds of ±1, ±1.5, and ±2 climatological standard deviation; Anomalies of Z at 500hPa with thresholds of ±25m and ±50m; Psea with thresholds of 1000hPa; Wind speed at 850hPa with thresholds of 10, 15, and 25m/s	Z at 500hPa; T at 850hPa; U and V at 850 and 250hPa; Wind speed at 850hPa; Psea
Score	Mean error, root mean square error, and anomaly correlation	Brier (skill) score, ROC-area (skill) score, and relative economic value	Continuous rank probability score
Time Interval	12 hours	24 hours	
Verification Area	NH extra-tropics, East Asia, Japan, Tropics, Western Pacific, SH extra-tropics, NH, SH, North America, Europe, and Asia		